The Graduate University for Advanced Studies
Shonan Village, Hayama, Kanagawa 240-0193 Japan

<u>Author</u>

PHAN Hong Khiem

Full one-loop electroweak radiative corrections at Future Colliders

<u>Supervisor</u>

Prof. Yoshimasa KURIHARA

<u>Referees</u>

Prof. Shoji HASHIMOTO	(Head Examiner)
Prof. Junpei FUJIMOTO	(Examiner)
Prof. Kyoshi KATO	(Examiner)
Prof. Mihoko NOJIRI	(Examiner)
Prof. Shigeru ODAKA	(Examiner)
Prof. Keisuke FUJII	(Examiner)

KEK-18th December 2014

Table of Contents

List of Figures

List of Tables

Abstract

In July 2012, ATLAS and CMS experiments at the Large Hadron Collider (LHC) announced the evidence for a new boson whose properties were consistent with the SM Higgs boson [1, 2, 3, 4, 5, 6]. The mass of the new boson was reported by two experiments as

- ATLAS: 126.0 ± 0.4(stat.)± 0.4(sys.) GeV;
- CMS: 125.3 ± 0.4(stat.)± 0.4(sys.) GeV.

Once the discovery of the Higgs boson is confirmed, it will open a new phase for studying particle physics. The expected program of future colliders, e.g. the high luminosity version of LHC, the International Linear Collider (ILC), not only makes precise measurements on the properties of the Higgs particle, top quarks and vector bosons interactions, but also search for physics Beyond the Standard Theory. The measurements will be performed at high precision. In order to match future precision data, the theoretical calculations to the experimental measurement such as cross section and decay width, with including higher order radiative corrections are mandatory. The calculations are great motivation and effort by many groups. Such calculations are one of the main targets of this thesis. In particular, the aim of thesis is twofold:

1. The first aspect of the thesis is to study how to calculate the experimental quantities in the framework of Quantum Field Theory. This part is mainly

focused to upgrade the GRACE-Loop program which is a generic automatic computer program for calculating High Energy Physics processes at one-loop electroweak corrections.

2. The second aspect of the thesis is to apply the above framework to compute the full $\mathcal{O}(\alpha)$ electroweak radiative corrections to some of the most important processes at future colliders. These processes are

   - $pp \to W^-W^+$ and $pp \to W^-W^+ + 1$ jet at the LHC;
   - $e^-e^+ \to e^-e^+\gamma$ at the ILC;
   - $e^-e^+ \to t\bar{t}$ and $e^-e^+ \to t\bar{t}\gamma$ at the ILC.

We observe that electroweak radiative corrections to W-pair production and W-pair production in association with a jet at the LHC are of sizeable impact (order 10%) in the high-energy region where the new-physics signatures are expected. The corrections must be included to interpret the new physics signals at the future LHC experiments.

For the processes at the ILC, the electroweak radiative corrections also form significant contributions (order 10%). Such corrections are very important contributions and they must be taken into consideration in the future.

Acknowledgements

First of all, I would like to express my deep gratitude to my friendly supervisor, Prof. Yoshimasa KURIHARA, for his inspirational and patient advice, enthusiasm suggestions and constant encouragement during my PhD time. I have learned a great methods from my supervisor perspective on research, the scientific approaches he analyses the Physical problems in a simple and pedagogical way. Moreover, I would like to thank my supervisor so much for his constant support me to attend many interesting conferences and internship program at NIKHEF.

I am deeply indebted to MINAMI-TATEYA GROUP: Prof. Junpei FUJIMOTO, Prof. Toshiaki KANEKO, Prof. Fukuko YUASA, Prof. Kyoshi KATO, Prof. Yoshimitsu SHIMIZU, Prof. Tadashi ISHIKAWA for their help and enthusiasm suggestions and constant encouragement. I would like to thank Prof. Shigeru ODAKA, Prof. Ken SASAKI and Prof. Tadashi KON, Prof. Masaaki KURODA and Prof. Masato JIMBO, Prof. Y. YASUI for their fruitful discussions. I would like to send my deeply thank to Prof. K. TOBIMATSU, Prof. N. NAKAZAWA and Prof. M. IGARASHI for useful discussions.

I would like to express my deep appreciate to Prof. J.A.M VERMASEREN for giving me a great chance to visit NIKHEF and for his advice during my time in NIKHEF. Thank to Prof. VERMASEREN so much for his effort to read the paper manuscripts and his encouragement.

I am indebted to Dr. DO Hoang Son, my advisor in master program at the

University of Science HoChiMinh City for his advice and enthusiasm suggestions. He has encouraged me so much to attach the difficult problem in Physics and to mature my research method.

Dr. Takahiro UEDA is a good friend, he is very good at computer program, specially he is a master in using and developing FORM. I am deeply indebted to Dr. Takahiro UEDA for his guidance and fruitful discussions about FORM as well as Physics.

I am indebted to Prof. Patrick AURENCHE, Prof. Pietro SLAVICH for supporting me to have great internship program at LPTHE. I had a great chance and fruitful discussions to Prof. Pietro SLAVICH about the Physics Beyond the Standard Model.

My deeply thank directly to Profs. TRAN Thanh Van and NGUYEN Anh Ky for their support and give me many chance to attend Vietnam School of Physics (VSOP).

I am grateful to Rencontres du Vietnam sponsored by Odon VALLET. My PhD's fellowship is supported by Japanese Government Scholarship (MEXT).

I am grateful to Profs. HOANG Dzung, NGUYEN Nhat Khanh, PHAN Quoc Khanh, Dr. NGUYEN Huu Nha at The University of Science HoChiMinh City for their teaching and their encouragement.

My deep appreciate to Prof. KANEMURA and Dr. YOKOYA for giving a chance to visit the University of Toyama and for their fruitful discussions.

I would like to express my deep appreciate to Prof. Mihoko NOJIRI, Prof. Shoji HASHIMOTO, Prof. Keisuke FUJII for give me many comments and suggestions and for their effort to read the manuscripts.

For interesting discussions I would like to thank Prof. Emi KOU, Ms. Nhi M. U. QUACH, Dr. KAWAMURA, Mr. Rottier OTTO, Dr. WATANABE and Dr. LE Duc Ninh, Dr. LE Tho Hue for many fruitful discussions.

I want to send my deeply thank to my colleagues at Thu Dau Mot University, Binh Duong, Vietnam: Dr. NGUYEN Van Hiep, Mr. TRAN Quang Thai, Dr. VO Van On for their support.

Life would not have been as colorful without the many good friends I have. I would like to express my deep thank to Mr. LE Van Hung, Mr. NGUYEN Tan Loc, Mr. NGUYEN Truong Co and Mr. PHAN Toai Tuyn. They are always with me to share happiness and disappointment.

Last but not least, I want to thank my warm family for their encouragement. To my wife, NGUYEN Vuong Ngoc Thy and specially for her present of love, our lovely son, PHAN Hoang Khiem for their invaluable love.

Introduction

It is human nature try to answer the fundamental question. What are the building blocks of matter? An earlier answer to the question was proposed by Thales about 2600 years ago. His concept was that the matter could be reduced to water. One century later, Anaximenes of Miletus thought that the world was made of four elements, such as earth, water, fire and air. Both Thales and Anaximenes's concepts of the fundamental structure of matter are very simple and economical in the number of building blocks.

In 1869 Mendeleev published the periodic table of elements. The table listed of the elements according to the basis of their atomic weights and recurring columns possessing the same chemical properties. In the Mendeleev's concept the matter was constructed by these elements. At the same time, many new chemical elements were discovered and arranged them into the table. From the theorist's point of view one may doubt that "Are there too many fundamental elements" by looking at the hundred of elements in the table. Are there substructures for these particles?

In 1898 Joseph Thomson discovered that the cathode rays are electron beams. The discovery was a big challenge for the elements in the Mendeleev's periodic table as units of the Universe. This discovery also opened a new era, i.e the subatomic era. In 1911 Rutherford analyzed the so-called "plum pudding model" of the atom by J. J. Thomson. He found that this model was incorrect. The model of atom was reformed by Rutherford. In Rutherford's concept the atom contains highly concentrated charge and mass in a very small volume at its center which later was named the "nuclei" of the atom. By 1919, the proton was discovered by Rutherford via $^{14}N + \alpha \rightarrow\ ^{17}O + p$. Later, in 1932 James Chadwick found the neutron. The discoveries modified the nice picture of fundamental elements drawn by Mendeleev.

In 1910, Charles Wilson invented the cloud chamber containing a supersaturated vapor of water or alcohol. The cloud chamber allowed us to capture the track of charged particles. Many hadrons thereof like baryons and mesons were discovered one by one in a very short period. In 1964 the quark model was formed by Murray Gell-Mann, Kazuhiko Nishijima and George Zweig. In this model, the hadrons are constructed by the fundamental elements which are called quarks. In 1968, a deep inelastic scattering experiment at the Stanford Linear Accelerator Center (SLAC) showed that the proton contains quarks. The picture of the fundamental elements was refreshed and the gold era of particle physics started.

All these particles discovered through the last century make up the most complete theory, the Standard Theory (SM), which was proposed by Steven Weinberg, Sheldon Glashow and Abdus Salam [7] in 1967. After discovering tau lepton (at SLAC) and bottom, top quarks (at Fermilab), the fundamental building blocks of the SM consist of three charged leptons, three corresponding neutrinos and six quarks in the fermion sectors. These fermions interact via gauge boson exchange: Specially the photon for electromagnetic interaction, the weak gauge bosons Z and $W^{\pm}$ for weak interaction, and eight gluons for the strong interaction. In the theory the masses of the bosons are generated through nowadays known as the Higgs-Brout-Englert-Guralnik-Hagen-Kibble mechanism [8, 9]. While the masses of fermions are explained by their strength of interaction with the scalar Higgs boson. Present-day the main goals of particle physics studies are to test the SM and probe the new physics.

The LEP collider [10] was built by European Organization for Nuclear Research (CERN). It is an electron-positron collider with a tunnel of 26.7 kilometer circumference at 50–175 meter underground, crossing the Switzerland–France border. The

LEP operated to provide electron-positron collisions from Z peak energies between 89 and 93 GeV up to the highest energies above the W-pair threshold between 161 and 209 GeV. One of the important goals of LEP experimental program was the measurement of the properties of W and Z bosons, such as their masses, widths and their couplings to fermions and gauge bosons.

After the measurements of the W and Z boson's properties, the LEP experiment was terminated in 2000. The Large Hadron Collider (LHC) was then built by CERN, the world's largest and most powerful particle accelerator [11] up to now. The LHC is a proton-proton colliding accelerator with center-of-mass energies up to 14 TeV. Its purpose is to allow physicists to verify the different theories of elementary particles, such as the SM theory, Super-Symmetric theory (SUSY), Extra-Dimension theory, etc.

In July 2012, ATLAS and CMS experiments announced the discovery of a new boson whose properties were consistent with the SM Higgs boson [1, 2, 3, 4, 5, 6]. The mass of the new boson was reported by two experiments as $M_H = 126.0 \pm 0.4(\text{stat.}) \pm 0.4(\text{sys.})$ GeV at ATLAS and $M_H = 125.3 \pm 0.4(\text{stat.}) \pm 0.4(\text{sys.})$ GeV at CMS. After discovering the Higgs boson, the purpose of LHC physics [12, 13] at 13 TeV and 14 TeV and future colliders, like the ILC [14], are as follows:

- to precisely study the newly discovered Higgs boson properties such as its mass, spin, Yukawa couplings, Higgs self coupling, etc. The measurements play a major role to understand the Higgs mechanism and open a portal to physics Beyond the Standard Theory (BSM).

- to study the electroweak processes: vector boson productions and diboson productions in association with jets will be collected. Such studies will play an important role to reduce the background for Higgs as well as new physics searches. The processes also improve the future precision on vector boson properties.

- to precisely measure top quark properties and top quark electroweak couplings.

It is a potential to probe the new physics effects.

- to search for new physics signals such as SUSY as expected, Extra-Dimension, etc.

Calculating the experimental quantities such as the cross section, decay width and their relevant distributions is one of the main goals of high energy physics. In order to explain the high precision data at future colliders, the precision studies from theoretical calculations to these quantities are desirable. The calculations of one-loop QCD and electroweak radiative corrections to multi-particle processes are very complicated and difficult study because of the following two main problems.

The first problem comes from handling a huge amount of Feynman diagrams when we calculate the multi-particles processes. Let us consider the process $e^-e+ \to e^-e^+\gamma$ at the level of one-loop electroweak corrections as an example. The process contains 3456 one-loop diagrams including counterterms and 32 tree diagrams in covariant gauge. It is not trivial task to generate all the Feynman diagrams and write down the corresponding matrix element of this process by hand. Faced with the difficulty, the computer programs for automated calculation are necessary.

The second difficulty is related to evaluate tensor one-loop integrals which is one of the most important ingredients of high order calculation. In general, the matrix element of the studied processes can be written in terms of tensor one-loop integrals. The tensor integrals will be reduced into the basic scalar integrals which are scalar one-loop one-, two-, three- and four-point functions.

The traditional method for tensor one-loop reduction was proposed by Passarino and Veltman (PV) [15]. In this scheme, the tensor integrals were decomposed into the Lorentz-covariant structure with coefficient of the form factor integrals which later written in terms of the scalar integrals. By contracting the Minkowski metric ($g_{\mu\nu}$) and external momenta into the tensor integrals, one can obtain the form factors. In this step, we have to solve a system of linear equations where the Gram determinants appear in the denominator. If the Gram determinants will vanish or become very small, the reduction method will break or will be spoiled the numerical stability (so-called Gram determinant problems).

In Ref [16], the numerically stable reduction for tensor one-loop integrals up to six-points was introduced. In this method the modified Caylay determinants are used to avoid zero of Gram determinants. In the cases where Gram determinants become very small, the suitable expansions are handled in order to gain the numerically stable results. The method was applied successfully to calculate $e^-e^+ \to 4$ fermions processes in the Refs [17, 18, 19].

A reduction method in Feynman-paramters space, the improvement of the so-called Brown-Feynman reduction, has been used in GRACE-Loop [21].

The on-shell methods were developed in Refs [22, 23]. These methods are analytical one which differs from PV. In progress, the on-shell methods have been mainly applied to calculate one-loop multi-leg QCD processes. The methods can also be extended for the massive cases which can hence be used for electroweak processes. Moreover, in the on-shell method the Gram determinant problems have not been solved completely but it can be under control.

A semi-analytical reduction method for tensor one-loop integrals to overcome Gram determinant problems, was presented in Refs [24, 25, 26]. The same progress with the on-shell method, the semi-analytical method has been mainly applied to calculate one-loop multi-leg QCD processes.

The aim of thesis is twofold:

The first aspect of the thesis is to upgrade GRACE-Loop which is a generic automatic computer program for calculating High Energy Physics processes at one-loop electroweak corrections. In particular the thesis concerns to study method for tensor reduction one-loop five point functions in

Ref [16]. We then implement it into GRACE-Loop with providing a useful tool to check the calculation on tensor one-loop five point functions. The test is performed by comparing this method to the current one in GRACE-Loop [21].

In the second aspect of the thesis, the full $\mathcal{O}(\alpha)$ electroweak radiative corrections to the most important processes at future colliders are reported. At the LHC, the calculation of $pp \to W^-W^+$ and $pp \to W^-W^+ + 1$ jet are performed. The physical results of this calculation are discussed, one finds that at high energy region where the new physics signature is expected, the electroweak corrections are of significant impact (order 10% contributions). Such corrections play an important role to interpret the new physics signals.

Full $\mathcal{O}(\alpha)$ electroweak radiative corrections to $e^-e^+ \to e^-e^+\gamma$ at the ILC are also done in this thesis. It is very interesting result to observe the electroweak corrections form a sizeable contribution to the total cross section. Its contribution must be taken into account for luminosity measurement at the ILC. The calculation also provides a useful framework for future target, the process $e^-e^+ \to e^-e^+\gamma$ with soft photon case at one-loop corrections. One subsequently arrives the two-loop corrections to Bhabha scattering in the future.

Moreover, the precise calculations to the top quark productions at the ILC are of great interest. Because the calculation will provide a key role to understand electroweak spontaneous symmetry breaking (EWSB) as well as to open a window for new physics signals. To match the high precision data at future colliders on the top quark properties, the electroweak radiative corrections to top quark productions thereof must be considered. The calculations are also performed in this thesis. **In particular, we computed the processes $e^-e^+ \to t\bar{t}$ and $e^-e^+ \to t\bar{t}\gamma$ at the ILC.** The impact of electroweak corrections to the total cross section, the top quark forward-backward asymmetry A_{FB} are investigated in the thesis. One finds that electroweak corrections are significant contribution to the total cross section and its relevant distributions. Its contribution must be taken into consideration for the precise studies of top properties at the ILC.

The outline of this thesis is as follows.

- A short review of the SM is given in the first chapter by paying attention to the SM structure and to the physics Beyond the SM.

- In chapter 2, we review the GRACE-loop in greater detail. Specially one concentrates to study the tensor reduction one-loop five point functions. The one-loop renormalization theory and on-shell renormalization scheme are also discussed in this chapter.

- The calculation of the full one-loop electroweak radiative corrections to the W-pair and the W-pair productions in association with a jet at the LHC is then presented in chapter 3. In the physical results of the calculation, one examines the impact of electroweak corrections to the total cross section as well as its relevant distributions in the full energy reach of future LHC.

- The full $\mathcal{O}(\alpha)$ electroweak radiative corrections to the process $e^+e^- \to e^+e^-\gamma$ at the International Linear Collider are presented in chapter 4. The chapter will be started with the luminosity measurement at the ILC firstly. One then investigates the electroweak corrections to the total cross-section as well as relevant distributions: the differential cross section as a function of the invariant masses, energies and angles of final particles.

- One-loop electroweak radiative corrections to the processes $e^+e^- \to t\bar{t}$ and $e^+e^- \to t\bar{t}\gamma$ at the ILC is reported in chapter 5. The electroweak corrections to the total cross section, and top quark forward-backward asymmetry A_{FB} are studied.

- Thesis includes several appendices. In appendix A, the counterterms of $gq\bar{q}$ are calculated. They are used for the computation of process $pp \to W^-W^+ + 1$ jet at the LHC. In appendix B, the input parameters for the calculation of all processes are showed. Moreover, the numerical check on all the calculations are presented in appendix C. Finally, the phase space integration of $2 \to n$ processes are discussed in appendix D.

Chapter 1

The Standard Theory and beyond

In this chapter we give a short introduction to the standard theory and its structure. We then discuss the unsolved questions in the SM and introduce briefly to physics Beyond the SM. We refer Refs [20, 21, 68] for furthermore detail.

1.1 The Standard Theory

Two great achievements in the 20th-century of physics are Quantum Mechanics and Relativity theories. Quantum Field Theory (QFT) is a framework which combines Quantum Mechanics and Relativity theories. It is an essential subject for describing the processes that occur at very small scales or at very high energies. The standard theory is a particular physical model of QFT, based on the symmetry group $SU_C(3) \bigotimes SU_L(2) \bigotimes U_Y(1)$. It describes the strong, electromagnetic and weak interactions of the set of matter field in the first three columns of table 1.1.

The matter field contains three charged leptons, three their corresponding neutrinos and six quarks. They are arranged into three generations, with so-called fermion generations. The fermions interact via the exchange of gauge bosons, which are presented in the fourth column of table 1.1: Specially γ for electromagnetic interaction, the Z and W bosons for weak interaction and eight gluons for strong interaction.

In the theory, weak boson masses are generated through nowadays well-known the Higgs-Brout-Englert-Guralnik-Hagen-Kibble mechanism [8, 9]. In this mechanism, a $SU(2)$ doublet of scalar complex field is introduced with its neutral developing a non-zero of vacuum expectation value. Subsequently, the $SU_L(2) \bigotimes U_Y(1)$ symmetry is spontaneously broken to the electromagnetic $U_Q(1)$ symmetry. At the end, the masses of W and Z bosons are generated by absorbing three of four degrees of freedom in scalar complex doublet. The remaining degree of freedom is corresponding to the Higgs boson, which is shown in the fifth column of table 1.1. In addition, the fermion masses are also generated through their Yukawa interaction to the Higgs boson.

<table>
<tr><th>I</th><th>II</th><th>III</th><th>Gauge Bosons</th><th>Higgs Boson</th></tr>
<tr><td>u</td><td>c</td><td>t</td><td>g</td><td rowspan="4">H</td></tr>
<tr><td>d</td><td>s</td><td>b</td><td>γ</td></tr>
<tr><td>e</td><td>μ</td><td>τ</td><td>Z</td></tr>
<tr><td>ν_{e}</td><td>ν_μ</td><td>ν_τ</td><td>W</td></tr>
</table>

Table 1.1: The Standard Theory of elementary particles, with the three generations of fermions, gauge bosons in the fourth column, and the Higgs boson in the fifth.

The following section will present the structure of the SM Lagrangian from classical to quantization.

1.1.1 The classical Lagrangian

The classical Lagrangian of the SM is built by requiring it to be local gauge invariant and renormalizable. The SM Lagrangian can be divided into the gauge, fermion, Higgs and Yukawa sectors.

$$\mathcal{L}^c_{SM} = \mathcal{L}_G + \mathcal{L}_F + \mathcal{L}_H + \mathcal{L}_Y. \tag{1.1}$$

These parts will be written explicitly.

The gauge sector $\mathcal{L}_G$

The gauge sector of the gauge symmetry $SU_C(3) \bigotimes SU_L(2) \bigotimes U_Y(1)$ is given by

$$\mathcal{L}_G = -\frac{1}{4}G^a_{\mu\nu}G^{a,\mu\nu} - \frac{1}{4}W^a_{\mu\nu}W^{a,\mu\nu} - \frac{1}{4}B_{\mu\nu}B^{\mu\nu}, \tag{1.2}$$

where $G^a_{\mu\nu}$, $W^a_{\mu\nu}$ and $B_{\mu\nu}$ denote for field-strength tensors of gluon, weak and hypercharge field respectively. These fields strength tensors are defined as follows

$$\begin{cases} G^a_{\mu\nu} = \partial_\mu G^a_\nu - \partial_\nu G^a_\mu - g_s f^{abc} G^b_\mu G^c_\nu, \quad a,b,c = 1,2,..,8; \\ W^a_{\mu\nu} = \partial_\mu W^a_\nu - \partial_\nu W^a_\mu - g\epsilon^{abc} W^b_\mu W^c_\nu, \quad a,b,c = 1,2,3; \\ B_{\mu\nu} = \partial_\mu B_\nu - \partial_\nu B_\mu. \end{cases} \tag{1.3}$$

The respective gauge couplings of these groups are denoted by g_s, g and g' and the structure constants of the non-abelian group $SU_C(3)$ and $SU_L(2)$ are f^{abc} and ϵ^{abc} as in usual notation.

The Lagrangian of gauge sector contains the kinematic terms of gauge field and their interactions.

The fermions sector $\mathcal{L}_F$

The fermions sector Lagrangian reads

$$\mathcal{L}_F = i\bar{Q}^i_L \not{D} Q^i_L + i\bar{u}^i_R \not{D} u^i_R + i\bar{d}^i_R \not{D} d^i_R + i\bar{L}^i_L \not{D} L^i_L + +i\bar{e}^i_R \not{D} e^i_R, \tag{1.4}$$

where $Q_L = (u_L, d_L)^T$ are the left-handed $SU(2)_L$ doublets of up-type quarks $u = u, c, t$ and down-type quarks $d = d, s, b$; $L_L = (\nu_{l_L}, l_L)^T$ are the left-handed $SU(2)_L$

doublets of charged leptons, $l = e, \mu, \tau$ and their corresponding neutrinos $\nu_{l_L} = \nu_e, \nu_\mu, \nu_\tau$; the u_R, d_R and e_R are corresponding to right-handed $SU(2)$ singlets.

The Lagrangian contains the kinematic terms of fermion fields and encodes the interactions of fermions with the gauge bosons through the covariant derivative which is

$$D_\mu = \partial_\mu - ig_s T_c^a G_\mu^a - igI_W^a W_\mu^a - ig'\frac{Y_W}{2}B_\mu, \tag{1.5}$$

here $T_c^a = \frac{\lambda^a}{2}$ (λ^a with $a = 1, \cdots, 8$ are Gell-Mann matrices), $I_W^a = \frac{\sigma^a}{2}$ (σ^a with $a = 1, 2, 3$ are Pauli matrices) and Y_W are corresponding to the generators of the gauge groups of $SU_C(3) \bigotimes SU_L(2) \bigotimes U_Y(1)$ respectively. The hypercharge satisfies the Gell-Mann-Nishijima relation

$$Q = I_W^3 + \frac{Y_W}{2}. \tag{1.6}$$

As a consequence, the physical gauge bosons are related to the gauge boson fields as follows

$$\begin{cases} W_\mu^\pm = (W_\mu^1 \mp iW_\mu^2)/\sqrt{2}, \\ Z_\mu = c_W W_\mu^3 - s_W B_\mu, \\ A_\mu = s_W W_\mu^3 + c_W B_\mu, \end{cases} \tag{1.7}$$

where the weak mixing angle and electric charge are fixed by

$$s_W = \frac{g'}{\sqrt{g^2 + g'^2}}, \quad c_W = \frac{g}{\sqrt{g^2 + g'^2}}, \quad e = \frac{gg'}{\sqrt{g^2 + g'^2}}.$$

The covariant derivative can now be written in terms of the physical gauge bosons as

$$\begin{aligned} D_\mu &= \partial_\mu - ig_s T_c^a G_\mu^a - i\frac{g}{\sqrt{2}}(I_W^+ W_\mu^+ + I_W^- W_\mu^-) \\ &\quad -i\frac{g}{c_W} Z_\mu (I_W^3 - s_W^2 Q) - ieQA_\mu, \end{aligned} \tag{1.8}$$

where $I_W^\pm = \frac{\sigma^1 \pm i\sigma^2}{2}$. Inserting the form of D_μ in Eq. (1.8) into Eq. (1.4), one obtains the interaction terms of fermions to gauge bosons.

The Higgs sector $\mathcal{L}_H$

The next part is the Higgs Lagrangian which is governed by

$$\mathcal{L}_H = (D^\mu\Phi)^+(D_\mu\Phi) - \mu^2\Phi^+\Phi - \lambda(\Phi^+\Phi)^2. \tag{1.9}$$

In this Lagrangian, the Higgs doublet is $\Phi = (\Phi^+, \Phi^0)^T$ with $Y_\Phi = 1$.

In the case of $\mu^2 < 0$, the neutral component develops a non-zero vacuum expectation value

$$< \Phi >_0 = < 0|\Phi|0 > = (0, v/\sqrt{2})^T \quad \text{with} \quad v = \sqrt{\frac{-\mu^2}{\lambda}}. \tag{1.10}$$

By expanding the Higgs field around the vacuum expectation value as

$$\Phi(x) = \frac{1}{\sqrt{2}}\begin{pmatrix} 0 \\ v + H(x) \end{pmatrix}, \tag{1.11}$$

we then express the first term in Eq.(1.9) and identify the coefficients of bilinear terms in the gauge fields $W_\mu^\pm$, Z_μ, A_μ and H as the masses of corresponding gauge bosons. In detail, by omitting the gluon fields in the covariant derivative, the first term in the Lagrangian of the Higgs sector reads

$$\begin{aligned}
\mathcal{L}_H &= (D^\mu\Phi)^+(D_\mu\Phi) + ... \\
&= \frac{1}{2}\left| \begin{pmatrix} \partial_\mu - ieQA_\mu - i\frac{g(I_W^3 - s_W^2 Q)}{c_W} Z_\mu & -ieW_\mu^+/\sqrt{2}\, s_W \\ -ieW_\mu^-/\sqrt{2}\, s_W & \partial_\mu - ieQA_\mu - i\frac{g(I_W^3 - s_W^2 Q)}{c_W} Z_\mu \end{pmatrix} \begin{pmatrix} 0 \\ v + H \end{pmatrix} \right|^2 \\
&+ \quad ... \\
&= \quad ... \quad + \frac{1}{4}(gv)^2 W_\mu^+ W^{-\mu} + \frac{1}{4}(g^2 + g'^2)v^2 Z_\mu Z^\mu + \quad ...
\end{aligned} \tag{1.12}$$

The identified masses are according to

$$M_W = \frac{gv}{2}, \quad M_Z = \frac{v}{2}\sqrt{g^2 + g'^2}, \quad M_A = 0, \quad M_H = \sqrt{-2\mu^2}. \tag{1.13}$$

The Yukawa sector $\mathcal{L}_Y$

The fermion masses can be generated by using the same scalar field and its isodoublet $\tilde{\Phi} = i\sigma_2\Phi^*$ possessing $Y_{\tilde{\Phi}} = -1$. The gauge invariant Lagrangian for the Yukawa interaction is introduced by

$$\mathcal{L}_Y = -Y_u^{ij}\bar{Q}_L^i\tilde{\Phi}u_R^j - Y_d^{ij}\bar{Q}_L^i\Phi d_R^j - Y_e^{ij}\bar{L}_L^i\Phi e_R^j + h.c. \tag{1.14}$$

The fermion mass matrices Y_f^{ij} are diagonal, one then generates the Cabibbo-Kobayashi-Maskawa (CKM) matrix which includes CP-violating phase parameters,

$$V = \begin{pmatrix} V_{ud} & V_{us} & V_{ub} \\ V_{cd} & V_{cs} & V_{cb} \\ V_{td} & V_{ts} & V_{tb} \end{pmatrix} = \begin{pmatrix} 0.97383 & 0.2272 & 0.00396 \\ 0.2271 & 0.97296 & 0.04221 \\ 0.00814 & 0.04161 & 0.9991 \end{pmatrix}. \tag{1.15}$$

The fermion masses are identified by requirement of non-zero vacuum expectation value of the Higgs field or

$$m_f = \frac{Y_f^{ii}v}{\sqrt{2}} = \frac{y_f v}{\sqrt{2}}, \tag{1.16}$$

with y_f being Yukawa coupling.

1.1.2 Quantization: gauge-fixing and ghost Lagrangian

Because of gauge freedom in the classical Lagrangian of the SM, a Lorentz-invariant quantization requires a gauge-fixing terms. The generalized 't Hooft-Feynman linear gauge-fixing to non-linear gauge is introduced in Ref [21, 38]:

$$\begin{aligned} \mathcal{L}_{GF} &= -\frac{1}{\xi_W}|(\partial_\mu - ie\tilde{\alpha}A_\mu - igc_W\tilde{\beta}Z_\mu)W^{\mu+} + \xi_W\frac{g}{2}(v + \tilde{\delta}H + i\tilde{\kappa}\chi_3)\chi^+|^2 \\ &\quad -\frac{1}{2\xi_Z}(\partial_\mu Z^\mu + \xi_Z\frac{g}{2c_W}(v + \tilde{\varepsilon}H)\chi_3)^2 - \frac{1}{2\xi_A}(\partial_\mu A^\mu)^2 \\ &= -\frac{1}{\xi_W}F^+F^- - \frac{1}{2\xi_Z}(F^Z)^2 - \frac{1}{2\xi_A}(F^A)^2, \end{aligned} \tag{1.17}$$

where

$$\begin{cases} F^{+} = (\partial_\mu - ie\tilde{\alpha}A_\mu - igc_W\tilde{\beta}Z_\mu)W^{\mu+} + \xi_W \frac{g}{2}(v + \tilde{\delta}H + i\tilde{\kappa}\chi_3)\chi^{+}, \\ F^{Z} = \partial_\mu Z^\mu + \xi_Z \frac{g}{2c_W}(v + \tilde{\varepsilon}H)\chi_3, \\ F^{A} = \partial_\mu A^\mu. \end{cases} \tag{1.18}$$

The full effective Lagrangian is required to be invariant under BRST transformation (It means that the theory must be gauge invariant and unitary). As a consequence, the ghost Lagrangian is introduced as

$$\mathcal{L}_{Gh} = \sum_{\alpha,\beta=V,\chi} \bar{u}^\alpha(x) \frac{\delta F^\alpha}{\delta\theta^\beta(x)} u^\beta(x), \tag{1.19}$$

with the θ^α are infinitesimal gauge transformation parameters and $V \equiv W^\pm, A, Z$, $\chi \equiv \chi^\pm, \chi_3$. The gauge fixing operators $\dfrac{\delta F^\alpha}{\delta\theta^\beta}$ are determined by the variation of the field $A, Z, W^\pm$ as well as $\chi^\pm, \chi_3$. From the determined gauge fixing operators, the ghost Lagrangian will be obtained. The resulting formulas in non-linear gauge fixing term can be found in Ref [21].

Including these additional Lagrangian, the full quantum Lagrangian of the SM theory reads

$$\mathcal{L}_{SM} = \mathcal{L}_G + \mathcal{L}_F + \mathcal{L}_H + \mathcal{L}_Y + \mathcal{L}_{GF} + \mathcal{L}_{Gh}. \tag{1.20}$$

1.2 The unsolved questions of the Standard Theory and Beyond the Standard Theory

The discovery of the Higgs boson at the LHC [1, 2] with a mass around 126 GeV was confirmed. Further measurements of its properties showed its consistency with the SM Higgs boson [3, 4, 5, 6]. It makes the SM theory is the greatest triumph of modern physics.

In spite of the great successes of the SM theory, it is unlikely to be the fundamental theory for describing the Universe. There are several questions can not be explained by the SM theory. First, the SM has an gauge hierarchy problem [27]. The quantum corrections to the scalar Higgs boson mass have an quadratic divergence. One leads to an unnatural fine-tunning between bare mass term and quantum corrections to ensure the Higgs mass with order 100 GeV. The second question is related to the unification of fundamental forces in the nature, the SM theory doesn't provide a framework for fitting the gravity force into gauge interactions at high energy scale (the GUT or Plank scale). Beside that the SM theory can not explain the origin of matter-antimatter asymmetry in the Universe. This problem is related to the strong CP violation, it can not be explained correctly by the SM theory. Finally, the SM theory lacks of an explanation for the observed dark matter and dark energy in the Universe.

These problems are great motivation for physic Beyond the SM theories. It is worth mentioning Super-Symmetric theory which is a generalization of the space time symmetry of Quantum Field Theory. That generalization leads to a transformation of fermions into bosons and vice versa. The SUSY provides a framework of the unification of gauge and gravity interactions at the Plank scale where the gravity force is of sizeable magnitude in comparison with gauge forces. It also provides a natural explanation for the gauge hierarchy problem. In the SUSY, the lightest super-partner particle is a promising candidate for the dark matter. Last one, the SUSY is also a potential explanation for the strong CP violation problem through loop corrections.

Beside that the Grand Unified Theory (GUT), Extra-Dimension theory and String Theory, etc are also proposed for complementing the SM theory. However these topics will not be discussed in more detail in the thesis. It is important to note that the main goals of the particle physics studies are not only to test the SM theory but also probe the physics Beyond the SM. Whenever one studies the SM or different kind of BSM scenarios at the future colliders, the precise calculation of Standard Model background play important role on the whole picture. These theoretical calculations are the main target of the thesis. The next chapter will be devoted to a framework for high order correction calculation in greater detail.

Chapter 2

GRACE-Loop

The chapter will discuss the technique for calculating cross section or decay width at one-loop corrections in greater detail. The calculations are based on a framework of perturbation theory. One will pay attention specially to one-loop renormalisation as well as reduction method for tensor one-loop integrals. The GRACE-Loop program will be also presented in concrete.

2.1 Motivation of the automatic calculation

Explaining the experimental data at high energy particle colliders (the LHC and ILC) is a challenging and complicated task. This procedure can be summarized as following steps. Experimentalists firstly collect the data of the interested events. The data includes the signal and backgrounds of the studied events. The data analysis is then carried out in order to reduce (or eliminate if it is possible) the backgrounds and gain the signal of the studied events as clear as possible. In order to interpret the physical meaning of the obtained events, the precise calculations to the experimental quantities are performed. Both the signal and backgrounds of the studied events must be evaluated precisely. It is a main task of theoretical calculations which are based on the SM or the BSM scenarios in following the perturbation theory. In the next step, the cross section (or decay width) of the corresponding events from theoretical calculations will be simulated by including parton shower and hadronization at the LHC (or photon bremsstrahlung effected at the ILC) as well as applying the geometrical acceptance of the detector. One eventually obtains Monte Carlo events which will be fitted into the collected data one at colliders by using statistical approaches. From this, the physical information will be extracted which will discriminate different kind of particle theories. In the whole procedure, the precise theoretical calculations are crucial.

There are several methods to calculate the cross section (decay width). One of them is to solve the Dyson-Schwinger equation in the iterative way [28, 29, 30]. However, this method has not been extended beyond the tree-level. The other one is diagrammatic approach. It is the traditional method to calculate the cross section (decay width) and has been extended to one-loop (and beyond) level.

In the diagrammatic approach, the cross section (decay width) can be calculated by the following steps

- Draw all the possible Feynman diagrams of the given process at fixed order of perturbation theory.
- Write down the amplitudes of diagram by diagram based on the set of Feynman rules. If higher order corrections are considered, one needs to calculate loop diagrams.
- Squaring the total amplitude, one then integrates it over phase space variables, and get eventually the cross section for the given process.

Thanks to the achievement of science and technology nowadays, the colliders provide more and more precise measurements on the physical quantities. Such precision measurements require the knowledge of higher order quantum corrections to the studied processes from theoretical calculations. In addition, high energy experiments at future colliders will open up the thresholds for multi-particle productions. Thus, the most precise calculation involves evaluation of the multi-particle processes including one-loop or two-loop corrections. For example, the electroweak processes such as di-boson, vector boson in association with multi-jets will be collected at future colliders. These vector bosons will decay into leptons or quarks (or jets) and their corresponding neutrinos (the latter becomes missing energy). For such productions, the precise calculation must handle higher order corrections to multi-particle processes such as $2 \to 3, 4, ..., 6$ processes.

The complexities will be increased tremendously when one calculates the multi-particles processes possessing the following problems. The first complicated issue is related to handing a huge number of Feynman diagrams. For example, several $2 \to 2, 3$ and 4 processes at the ILC are considered at the level of one-loop corrections. The number of Feynman diagrams in the covariant gauge are listed in Table 2.1. One finds that the number of Feynman diagrams raise tremendously with increasing number of final particles.

Processes	$N_{\text{Tree diagrams}}$	$N_{\text{Loop diagrams}}$
$e^-e^+ \to t\bar{t}$	4	150
$e^-e^+ \to bW^+\bar{t}$	17	1794
$e^-e^+ \to b\bar{b}W^+W^-$	166	34802

Table 2.1: The number of Feynman diagrams in the covariant gauge. $N_{\text{Loop diagrams}}$ includes one-loop virtual diagrams and counterterm diagrams.

The strategy for hand calculation of these processes is to select the dominant diagrams. The diagrams contained the coupling of Higgs to electron and position, for example, can be omitted, because their contributions are smaller than the Monte Carlo integration accuracy. However, the hand calculations are very difficult to perform and prone to error. Furthermore, a complete hand calculation for such processes is impossible. Even in the tree level, the integration the squared total amplitude of the given process is impossible to evaluate by hand calculation.

Beside handing huge number of Feynman diagrams, the technique for evaluating tensor one-loop and two-loop integrals is very complicated. There are no ideal techniques up to now for complete tensor two-loop integrals with arbitrary internal masses in analytical manner. The tensor one-loop integrals up to six point functions were performed by several approaches. In general, the tensor integrals will be reduced into the basic scalar integrals which are scalar one-loop one-, two-, three- and four-point functions. The difficulties in the evaluation of tensor one-loop integrals are to deal with a Gram determinant problems, Landau singularity [31]. The Landau singularity is related to the appearance of unstable particles.

The traditional method for tensor one-loop reduction was proposed by Passarino and Veltman [15]. In this scheme, the tensor integrals were decomposed into the Lorentz-covariant structure with coefficient of the form factor integrals which later written in terms of the scalar integrals. By contracting the Minkowski metric ($g_{\mu\nu}$) and external momenta into the tensor integrals, one can obtain the form factors. In this step, we have to solve a system of linear equations where the Gram determinants appear in the denominator. If the Gram determinants will vanish or become very small, the reduction method will break or spoil numerical stability.

In Ref [16], numerically stable reduction for tensor one-loop integrals up to six points was introduced. In this method the modified Caylay determinants are used to avoid zero Gram determinants. For the cases where Gram determinants become very small, suitable expansions are employed in order to gain the numerically stable results. The method was applied successfully to calculate $e^-e^+ \rightarrow 4$ fermions processes in Refs [17, 18, 19].

In addition, the on-shell methods have been developed in Refs [22, 23]. The methods are analytical one which differs from PV. In progress, the on-shell methods have been mainly applied to calculate one-loop multi-leg QCD processes. It can be extended for the massive cases which can hence be used for electroweak processes. In the on-shell method the Gram determinant problems have not been solved completely but it can be under control.

A semi-analytical method for reduction of tensor one-loop integrals which can overcome Gram determinant problems, was presented in Refs [24, 25, 26]. In the same progress with the on-shell method, the semi-analytical method has been mainly applied to calculate one-loop multi-leg QCD processes.

A reduction method in Feynman-parameters space, the improved Brown-Feynman reduction method, has been used in GRACE-Loop [21]. This method will be discussed in further detail in the next section.

Faced with these difficulties, an ideal solution for automatic calculations of multi-particle processes including radiative corrections from the Lagrangian, is proposed. For the purpose, the thesis will introduce and focus on development of the GRACE-Loop program.

2.2 Introduction to GRACE-Loop

GRACE is a generic automatic computer program for calculating High Energy Physics processes up to one-loop corrections within the SM and Minimum Super-Symmetry Model (MSSM) [32]. The program has been developed by MINAMI-TATEYA group at High Energy Accelerator Research Organization (KEK) [33] and at some universities[1]. The first version of GRACE is dedicated to GRACE-tree which provides helicity amplitude and corresponding cross section at tree level. This version includes the SM and MSSM as well as many other BSMs.

GRACE-Loop has been then developed in 2002 [21]. It mainly focuses on the one-loop electroweak corrections to the SM processes at e^+e^- colliders. In parallel with the GRACE-Loop development, the program named GRACE-SUSY/1-LOOP has also been built for evaluating one-loop corrections in the MSSM [34, 35, 36]. This thesis only focuses on describing the GRACE-Loop program. The feature of the program and its structure will be presented in the next paragraphs.

[1]Kogakuin, Seikei, Chiba, Meiji Gakuin universities and Tokyo Management College.

In the GRACE-Loop, the renormalization is carried out with the on-shell renormalization conditions of the Kyoto scheme, as described in Ref [37]. The ultraviolet (UV) divergences are regulated by dimensional regularization, while the infrared (IR) divergences are regularized by giving the virtual photon an infinitesimal mass λ. It will be described in more detail in the next sections.

The program has been equipped with so-called non-linear gauge fixing terms [38] in the Lagrangian which are described in Eq.(1.17). In the practical calculation, we are working in the R_ξ-type gauges with the condition $\xi_W = \xi_Z = \xi_A = 1$ (also called the 't Hooft-Feynman gauge). There is no longitudinal contribution in the gauge propagator. This choice has not only the advantage of making the expressions much simpler. It also avoids unnecessary large cancellations, high tensor ranks in the one-loop integrals and extra powers of momenta in the denominators which cannot be handled by the FF and LoopTools packages [39, 40]. With the implementation of non-linear gauge fixing terms the program provides a powerful tool to check the results in a consistent way. After all, the results must be independent of the non-linear gauge parameters. It will be discussed in greater detail in chapter 3, section of test on the calculation of $pp \to W^+W^- + 1$ jet at the LHC.

In its latest version GRACE-Loop can use the axial gauge in the projection operator for external photons. This implementation is achieved in this thesis. It cures a problem with large numerical cancellations. This is very useful once calculating processes at small angle and energy cuts for the final particles. This implementation also provides a useful tool to check the consistency of the results which, due to the Ward identities, must be independent of the choice of the gauge.

The structure of GRACE-Loop is described in the following flow chart 2.1. Its structure is also explained explicitly in the following paragraphs:

- THEORY: the SM model with non-linear gauge fixing terms in the Lagrangian

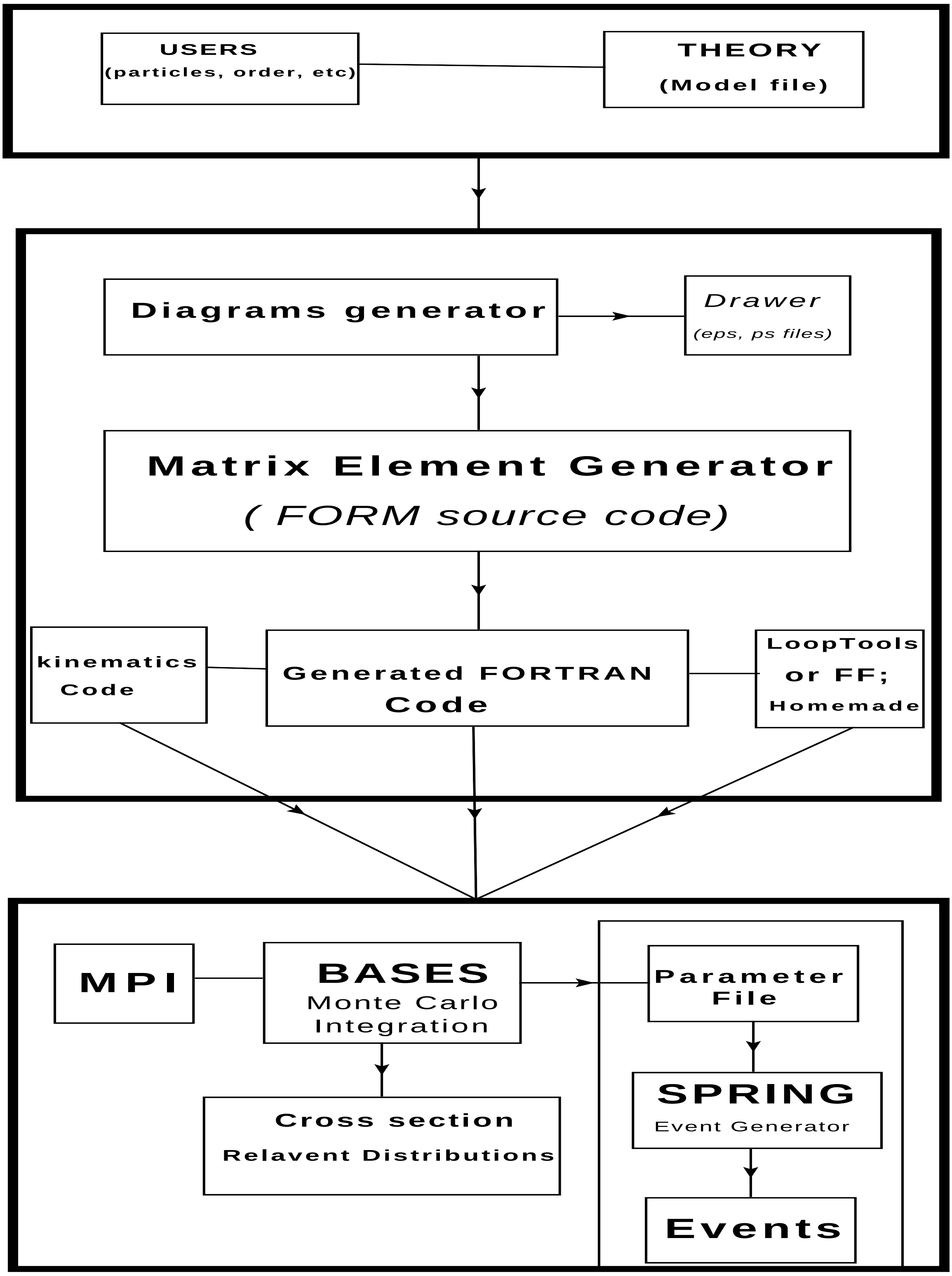

Figure 2.1: The GRACE-Loop flow chart.

has been implemented. In this model file, the particle contents and their interactions as well as the counterterms are provided.

- USERS: For a given process, a user will input the incoming particles, final particles and fix the order of perturbation theory.

- FEYNMAN DIAGRAMS GENERATOR: Once the process to study is fixed, the Feynman diagrams will be generated automatically by GRACE-Loop. The program also supports to generate full set of Feynman diagrams in covariant gauge and unitary gauge. In addition, the users can export the Encapsulated PostScript file for Feynman diagrams in GRACE-Loop.

- MATRIX ELEMENT GENERATOR: From the Feynman diagrams, the program will write down symbolic source code of the squared amplitude on a diagram by diagram basis by means of FORM [41, 42, 43, 44, 45]. FORM then will be used to convert the symbolic source code into FORTRAN one. In this step, the tensor one-loop integrals will be reduced to the scalar one-loop one-, two-, three- and four-point functions. These scalar integrals will later be evaluated numerically by FF or LoopTools packages.

- PHASE SPACE INTEGRATIONS: After generating the FORTRAN source code of the squared amplitude for the given process, one then combines it with kinematic program and scalar one-loop integrals library. The phase space integration is performed via the Monte Carlo integration program BASES [46], one eventually gets the cross section. The simulation and event generation are performed with the help of SPRING [46]. GRACE-Loop also includes kinematics data for processes up to six final particles.

The program has been used to calculate a variety of $2 \to 2$-body electroweak processes in Ref [21]. The GRACE-Loop program has also been used to calculate $2 \to 3$-body processes such as $e^+e^- \to ZHH$ [47], $e^+e^- \to t\bar{t}H$ [48], $e^+e^- \to \nu\bar{\nu}H$ [49]. The above calculations have been done independently by other groups, for example the processes $e^+e^- \to ZHH$ [50], $e^+e^- \to t\bar{t}H$ [51, 52, 53] and $e^+e^- \to \nu\bar{\nu}H$ [54, 55]. Also the $2 \to 4$-body process $e^+e^- \to \nu_\mu\bar{\nu}_\mu HH$ [56] was calculated successfully with the use of the GRACE-loop system. Recently, full one-loop electroweak radiative corrections to $e^-e^+ \to t\bar{t}\gamma,\ e^-e^+\gamma$ at the ILC [57, 58] have been performed with the help of GRACE-Loop program.

2.3 One-loop renormalisation

Suppose that one aims to calculate a physical quantity F (F can be cross section, decay width or their relevant distributions for example) at one-loop corrections. The quantity F is a function of bare parameters g_0 which can be the coupling, masses, etc. As a result, F will become infinity because the one-loop integrals contain the ultraviolet divergences. A procedure of renormalisation in which the bare parameters g_0 in the Lagrangian will be redefined in terms of the physical ones and give them measured values from the knowledge of experimental data.

The one-loop renormalisation of the SM theory can be performed in the following steps. Firstly, the base parameters and tadpole are redefined in terms of physical one and the counterterms as

$$\begin{cases} M_{0,W}^2 = M_W^2 + \delta M_W^2, \\ M_{0,Z}^2 = M_Z^2 + \delta M_Z^2, \\ m_{0,f} = m_f + \delta m_f, \\ M_{0,H}^2 = M_H^2 + \delta M_H^2, \\ e_0 = Ye = (1+\delta Y)e, \\ T^0 = T + \delta T. \end{cases} \tag{2.1}$$

The wave function renormalisation constants are defined as

$$W_{0,\mu}^{\pm} = (1 + \delta Z_W^{1/2}) W_\mu^{\pm}, \tag{2.2}$$

and

$$\begin{pmatrix} Z_{0\mu} \\ A_{0,\mu} \end{pmatrix} = \begin{pmatrix} 1+\delta Z_{ZZ}^{1/2} & \delta Z_{ZA}^{1/2} \\ \delta Z_{AZ}^{1/2} & 1+\delta Z_{AA}^{1/2} \end{pmatrix} \begin{pmatrix} Z_{\mu} \\ A_{\mu} \end{pmatrix}. \tag{2.3}$$

For the fermion wave functions

$$\begin{cases} f_{0,LR} = (1+\delta Z_{f_{LR}}^{1/2}) f_{LR}, \\ \bar{f}_{0,LR} = (1+\delta Z_{\bar{f}_{LR}}^{1/2}) \bar{f}_{LR}, \end{cases} \tag{2.4}$$

where L, R denote left- and right-handed fermions.

For the scalar sector one has

$$S_0 = (1+\delta Z_S^{1/2}) S, \tag{2.5}$$

with $S = H, \chi^{\pm}, \chi_3$.

We determine, for example the counterterms δM_W^2, $\delta Z_W^{1/2}$, in such a way the transverse part of the renormalised W-boson self energy $\Pi_T^W(q^2)$ at the M_W^2 behavior like QED or

$$\begin{cases} \Pi_T^W(q^2 \to M_W^2) = 0 \\ \dfrac{d}{d\, q^2}\, \Pi_T^W(q^2 \to M_W^2) = 0 \end{cases} \tag{2.6}$$

As a consequence, the W boson mass M_W is identical at the pole position of its propagator. For this reason, we call it on-shell renormalisation conditions [37]. In the next paragraphs, the on-shell renormalisation conditions will be discussed in concrete.

One particle irreducible two-point functions can cast into form

$$\tilde{\Pi} = \Pi + \hat{\Pi}, \tag{2.7}$$

where $\tilde{\Pi}$ denotes the sum of one-loop two-point diagram (Π) contributions and counterterms ($\hat{\Pi}$). The one-loop two-point functions can be decomposed into the Lorentz structure as in the following table:

type	formula
vector-vector	$\Pi_{\mu\nu}(q^2) = \left(g_{\mu\nu} - \frac{q_\mu q_\nu}{q^2}\right)\Pi_T(q^2) + \frac{q_\mu q_\nu}{q^2}\Pi_L(q^2)$
scalar-scalar	$\Pi(q^2)$
vector-scalar	$iq_\mu \Pi(q^2)$ (q is the momentum of the incoming scalar)
fermion-fermion	$\Sigma(q^2) = K_1 I + K_5\gamma_5 + K_\gamma \not{q} + K_{5\gamma}\not{q}\gamma_5$

The counterterms will be written explicitly as follow

1. Vector-Vector

WW	$\hat{\Pi}_T^W = \delta M_W^2 + 2(M_W^2 - q^2)\delta Z_W^{1/2}$
	$\hat{\Pi}_L^W = \delta M_W^2 + 2M_W^2 \delta Z_W^{1/2}$
ZZ	$\hat{\Pi}_T^{ZZ} = \delta M_Z^{1/2} + 2(M_Z^2 - q^2)\delta Z_{ZZ}^{1/2}$
	$\hat{\Pi}_L^{ZZ} = \delta M_Z^{1/2} + 2M_Z^2 \delta Z_{ZZ}^{1/2}$
ZA	$\hat{\Pi}_T^{ZA} = (M_Z^2 - q^2)\delta Z_{ZA}^{1/2} - q^2 \delta Z_{AZ}^{1/2}$
	$\hat{\Pi}_L^{ZA} = M_Z^2 \delta Z_{ZA}^{1/2}$
AA	$\hat{\Pi}_T^{AA} = -2q^2 \delta Z_{AA}^{1/2}$
	$\hat{\Pi}_L^{AA} = 0$

2. Scalar-Scalar

HH	$\hat{\Pi}^H = 2(q^2 - M_H^2)\delta Z_H^{1/2} - \delta M_H^2 + \frac{3\delta T}{v}$
$\chi_3\chi_3$	$\hat{\Pi}^{\chi_3} = 2q^2 \delta Z_{\chi_3}^{1/2} + \frac{\delta T}{v}$
$\chi\chi$	$\hat{\Pi}^{\chi} = 2q^2 \delta Z_\chi^{1/2} + \frac{\delta T}{v}$

3. Vector-Scalar

$W\chi$	$\hat{\Pi}^{W\chi} = M_W(\delta M_W/M_W + \delta Z_W^{1/2} + \delta Z_\chi^{1/2})$
$Z\chi_3$	$\hat{\Pi}^{Z\chi_3} = M_Z(\delta M_Z/M_Z + \delta Z_{ZZ}^{1/2} + \delta Z_{\chi_3}^{1/2})$
$A\chi_3$	$\hat{\Pi}^{A\chi_3} = M_Z \delta Z_{ZA}^{1/2}$

4. Fermion-Fermion: the fermionic sector can be written as

$$\begin{aligned}
\hat{K}_1 &= -m_f\left(\delta Z_{fL}^{1/2}+\delta Z_{fR}^{1/2}\right)-\delta m_f, \\
\hat{K}_5 &= 0, \\
\hat{K}_\gamma &= \left(\delta Z_{fL}^{1/2}+\delta Z_{fR}^{1/2}\right), \\
\hat{K}_{5\gamma} &= -\left(\delta Z_{fL}^{1/2}-\delta Z_{fR}^{1/2}\right) .
\end{aligned} \tag{2.8}$$

We are now going to apply on-shell renormalisation conditions to get the counterterms.

1. Tadpole

   Because the tadpole does not contribute to the calculation of physical quantities, its counterterms can be determined in such a simple way $\tilde{T} = T^{1-\text{loop}} + \delta T$=0. One then obtains

$$\delta T = -T^{1-\text{loop}}. \tag{2.9}$$

2. Charged vector

   As mention in previous paragraphs that the transverse part of $\Pi_T^{W^\pm}(q^2)$ behaves like QED in the limit $q^2 \to M_W^2$. It means that

$$\Re e\tilde{\Pi}_T^W(M_W^2)=0, \quad \frac{d}{dq^2}\Re e\tilde{\Pi}_T^W(q^2)\bigg|_{q^2=M_W^2}=0 \tag{2.10}$$

   This gives the following relations:

$$\delta M_W^2 = -\Re e\Pi_T^W(M_W^2), \quad \delta Z_W^{1/2} = \frac{1}{2}\frac{d}{dq^2}\Re e\Pi_T^W(q^2)\bigg|_{q^2=M_W^2} . \tag{2.11}$$

3. Neutral vector

   We impose the conditions on the photon-photon and Z-Z self-energies are the same as with the W-W case. In addition it is required that there should be no mixing between Z and the photon at the poles $q^2 = 0, M_Z^2$. That means

$$\Re e\tilde{\Pi}_T^{ZZ}(M_Z^2)=0, \quad \frac{d}{dq^2}\Re e\tilde{\Pi}_T^{ZZ}(q^2)\bigg|_{q^2=M_W^2}=0\ , \tag{2.12}$$

$$\tilde{\Pi}_T^{AA}(0) = 0, \quad \frac{d}{dq^2}\tilde{\Pi}_T^{AA}(q^2)\Big|_{q^2=0} = 0\ , \tag{2.13}$$

$$\tilde{\Pi}_T^{ZA}(0) = 0, \quad \Re e\tilde{\Pi}_T^{ZA}(M_Z^2) = 0\ . \tag{2.14}$$

There are six conditions, $\tilde{\Pi}_T^{AA}(0) = 0$ produces nothing, except that it ensures that the loop calculation does indeed give $\Pi_T^{AA}(0) = 0$. One obtains,

$$\delta M_Z^2 = -\Re e\Pi_T^{ZZ}(M_Z^2), \quad \delta Z_{ZZ}^{1/2} = \frac{1}{2}\Re e\frac{d}{dq^2}\Pi_T^{ZZ}(q^2)\Big|_{q^2=M_Z^2}\ , \tag{2.15}$$

$$\delta Z_{AA}^{1/2} = \frac{1}{2}\frac{d}{dq^2}\Pi_T^{AA}(0)\ , \tag{2.16}$$

$$\delta Z_{ZA}^{1/2} = -\Pi_T^{ZA}(0)/M_Z^2, \quad \delta Z_{AZ} = \Re e\Pi_T^{ZA}(M_Z^2)/M_Z^2. \tag{2.17}$$

4. Higgs

   The on-shell conditions are applied in such a way that we ensure the pole-position of the propagator is M_H^2, or

$$\Re e\tilde{\Pi}^H(M_H^2) = 0, \quad \frac{d}{dq^2}\Re e\tilde{\Pi}^H(q^2)\Big|_{q^2=M_H^2} = 0\ . \tag{2.18}$$

   These conditions will arrive at the following relations:

$$\delta M_H^2 = \Re e\Pi^H(M_H^2) + \frac{3\delta T}{v}, \quad \delta Z_H^{1/2} = -\frac{1}{2}\frac{d}{dq^2}\Re e\Pi^H(q^2)\Big|_{q^2=M_H^2}\ . \tag{2.19}$$

5. Fermion

   The on-shell renormalisation conditions are applied that the pole-positions are identical as the physical particles. Moreover the vanishing of γ_5 and $\gamma^\mu\gamma_5$ terms at the pole is required. These conditions read

$$\begin{cases} m_f\Re e\tilde{K}_\gamma(m_f^2) + \Re e\tilde{K}_1(m_f^2) = 0, \\ \frac{d}{d\not{q}}\Re e\left(\not{q}\tilde{K}_\gamma(q^2) + \tilde{K}_1(q^2)\right)\Big|_{\not{q}=m_f} = 0, \\ \Re e\tilde{K}_5(m_f^2) = 0, \Re e\tilde{K}_{5\gamma}(m_f^2) = 0. \end{cases} \tag{2.20}$$

Because of CP invariance, it leads to $K_5 = 0$. Thus it means that one can take both $\delta Z_{fL}^{1/2}$ and $\delta Z_{fR}^{1/2}$ to be real by using the invariance under a phase rotation. One obtains the following relations:

$$\begin{cases} \delta m_f = \Re e\left(m_f K_\gamma(m_f^2) + K_1(m_f^2)\right) \ , \\ \delta Z_{f_L} = \frac{1}{2}\Re e(K_{5\gamma}(m_f^2) - K_\gamma(m_f^2)) - m_f \frac{d}{dq^2}\left(m_f \Re e K_\gamma(q^2) + \Re e K_1(q^2)\right)\Big|_{q^2=m_f^2} \ , \\ \delta Z_{f_R} = -\frac{1}{2}\Re e(K_{5\gamma}(m_f^2) + K_\gamma(m_f^2)) - m_f \frac{d}{dq^2}\left(m_f \Re e K_\gamma(q^2) + \Re e K_1(q^2)\right)\Big|_{q^2=m_f^2} \end{cases} \tag{2.21}$$

6. Charge

We apply the conditions that the coupling of vertex $e^-e^+\gamma$ is $-e$ at the Thomson limit $q^2 \to 0$ and the $e^\pm$ with momenta $p_\pm$ are on-shell or

$$(e^+e^-A \text{ one loop term} + e^+e^-A \text{ counter term})\Big|_{q=0,p_\pm^2=m_e^2} = 0 \ . \tag{2.22}$$

The counterterm is written as a combination of $\delta Z_{AA}^{1/2}$ and $\delta Z_{ZA}^{1/2}$ or as

$$\delta Y = -\delta Z_{AA}^{1/2} + \frac{s_W}{c_W}\delta Z_{ZA}^{1/2} \ . \tag{2.23}$$

This relation is universal and written explicitly

$$\delta Y = \frac{\alpha}{4\pi}\left\{-\frac{7}{2}(C_{UV} - \log M_W^2) - \frac{1}{3} + \frac{2}{3}\sum_f Q_f^2(C_{UV} - \log m_f^2)\right\} , \tag{2.24}$$

with $C_{UV} = \dfrac{1}{\varepsilon} + \gamma_E - \log(4\pi)$ is the ultraviolet divergence parameter.

7. The unphysical sector

This part, in principle, does not contribute to the physical quantities. However, in practical calculation of one-loop correction in covariant gauge, the fields $\chi^\pm$ and χ_3 appear. The renormalisation for this part must be taken into account. It can be performed in a simple way as

$$\delta Z_\chi^{1/2} = -\frac{1}{2}\frac{d}{dq^2}\left(\Pi^\chi(q^2)\right)\Big|_{C_{UV}-\text{part}} \qquad \text{with} \quad \chi^\pm, \chi_3, \tag{2.25}$$

where $\Pi^\chi(q^2)\Big|_{C_{UV}-\text{part}}$ is only the divergent part of the Goldstone boson two-point functions.

2.3.1 Renormalisation scheme

In order to make a theoretical prediction, a set of independent parameters of the theory must be determined from experimental data. Renormalisation scheme reflects a specific choice of the experimental data points. If the measured quantity can be calculated exactly by mean of considering all orders of perturbation theory, it must be independent of renormalisation schemes. However, in the truncated perturbation theory, the measured quantity depends on the different choices of schemes, with so-called scheme dependence. In this thesis, we restrict our discussion on the on-shell renormalisation in Kyoto scheme which is described in further detail in Ref [37].

In this scheme, the set of input parameters are chosen to be $\mathcal{O} = \{\alpha(0) = 1/137.0359895,\ M_Z,\ M_W$ and fermion masses as well as Higgs mass$\}$. The Z boson mass has been precisely measured, at the current $M_Z = 91.1876 \pm 0.0021$ GeV as reported in PDG [59]. This uncertainty is small enough to probe the new physics signals at the future colliders. Contrary to the Z boson case, the W boson mass $M_W = 80.385 \pm 0.015$ GeV is reported in PDG [59]. At the current stage of precision at the LHC experiment, $\delta M_W = 15$ MeV is enough to explain the experimental data. With high precision program at future colliders, the uncertainty of δM_W around 4 MeV is desirable. In order to reduce theoretical uncertainties, M_W will be calculated as a function of M_Z, M_H and G_μ as follow [60]

$$M_W^2 = M_Z^2 \left\{ \frac{1}{2} + \sqrt{\frac{1}{4} - \frac{\pi\alpha}{\sqrt{2} G_\mu M_Z^2}[1 + \Delta r(M_W, M_Z, M_H, m_t, ...)]} \right\}, \tag{2.26}$$

where Δr summarizes a radiative corrections to the muon decay width [61]. The prediction for M_W is obtained by means of an iterative procedure from Eq.(2.26) since Δr itself depends on the W boson mass. At one-loop corrections, Δr is related to the large light-fermion contributions from the running fine structure constant from Thompson limit to M_Z scale ($\Delta\alpha$), and the leading contribution to the ρ parameter, $\Delta\rho$, which is quadratically dependent on the top quark mass. The result reads

$$\Delta r = \Delta\alpha - \frac{c_W^2}{s_W^2}\Delta\rho + \Delta r_{\mathrm{rem}}(M_H), \tag{2.27}$$

where $\Delta\alpha = 0.0593 \pm 0.0007$ [60], and

$$\begin{aligned} \Delta\rho &= \frac{3\alpha}{16\pi s_W^2 c_W^2} \cdot \frac{m_t^2}{M_Z^2}, \\ \Delta r_{\rm rem}(M_H) &= \frac{\alpha}{16\pi s_W^2 c_W^2} \cdot \frac{11}{3}\Big(\log\frac{M_H^2}{M_W^2} - \frac{5}{6}\Big). \end{aligned} \tag{2.28}$$

Table (2.2) shows numerical values of M_W and Δr at one-loop corrections as a function of M_H at $M_Z = 91.1876$ GeV and $m_t = 173.5$ GeV.

M_H [GeV]	Δr	M_W [GeV]
100	0.02396	80.388
120	0.02471	80.374
126	0.02491	80.370
200	0.02680	80.333

Table 2.2: The prediction for M_W as a function of M_H at $M_Z = 91.1876$ GeV and $m_t = 173.5$ GeV.

Once the input parameters are chosen, the total cross section, $\sigma_{\mathcal{O}(\alpha)}$, at one-loop radiative corrections is generated, the electroweak corrections can be expressed in this scheme as

$$\delta^{\alpha}_{\rm EW} = \frac{\sigma_{\mathcal{O}(\alpha)}}{\sigma_0} - 1, \tag{2.29}$$

where σ_0 is cross section of tree level. Because α is inputed in the Thompson limit, the $\delta^{\alpha}_{\rm EW}$ is called electroweak corrections in α-scheme. As a consequence, $\delta^{\alpha}_{\rm EW}$ will be affected by large contribution from two-point functions with light-fermion exchange. Its contribution forms as $\log(s/m_f^2)$ with energy scale s and the light-fermion masses m_f.

In the most practical purpose, one can express the electroweak corrections in G_μ-scheme ($\delta^{G_\mu}_{\rm EW}$), the improved Born approximation method. In this scheme the fine structure constant will be run from $q^2 = 0$ to $q^2 = M_Z^2$ scale. A part of higher order corrections from two-point functions involving the light fermion exchange, will be absorbed into the tree cross section.

The relation between $\delta_{\rm EW}^{\alpha}$ and $\delta_{\rm EW}^{G_\mu}$ can be derived as follows. The total cross section of the reaction $2 \to n$ (it is also supposed that n is order of α) can be written by

$$\sigma_{\mathcal{O}(\alpha)} = \alpha^n(0) \int d\Omega_n \mathcal{M}_0^2 (1 + \delta_{EW}^{\alpha}), \tag{2.30}$$

where $\mathcal{M}_0^2$ is the tree level amplitude squared after factorizing out the coupling, $d\Omega_n$ is the phase space of n final particles. Applying the running coupling constant equation $\alpha(0) = \alpha(M_Z^2)(1 - \Delta r)$, one obtains

$$\begin{aligned} \sigma_{\mathcal{O}(\alpha)} &= \alpha^n(M_Z) \int d\Omega_n \mathcal{M}_0^2 (1-\Delta r)^n (1 + \delta_{EW}^{\alpha}), \\ &\simeq \alpha^n(M_Z) \int d\Omega_n \mathcal{M}_0^2 \Big(1 - n\Delta r + \delta_{EW}^{\alpha} + \mathcal{O}((\Delta r)^2)\Big). \end{aligned} \tag{2.31}$$

From that, one finds out the relation $\delta_{\rm EW}^{G_\mu} = \delta_{\rm EW}^{\alpha} - n\Delta r$.

2.4 Tensor one-loop reduction

A general form of tensor one-loop integrals involving N external particles (N-points) in dimensional regularization ($n = 4 - 2\varepsilon$), as described in figure 2.2, reads

$$T^{(N)}_{\underbrace{\mu\nu\cdots\rho}_{M}} = \int \frac{d^n l}{(2\pi)^n} \frac{l_\mu l_\nu \cdots l_\rho}{D_0 D_1 \cdots D_{N-1}}, \quad M \leq N, \tag{2.32}$$

where

$$D_i = (l + s_i)^2 - M_i^2, \quad s_i = \sum_{j=1}^{i} p_j, \quad s_0 = 0,$$

M_i are masses of the particles circulating in the loop, l is the loop momentum, p_i are external momenta and s_i are a combination of external momenta. The scalar one-loop N-point integrals correspond to $M = 0$ or the numerator of the integrand of Eq. (2.32) being identical to 1.

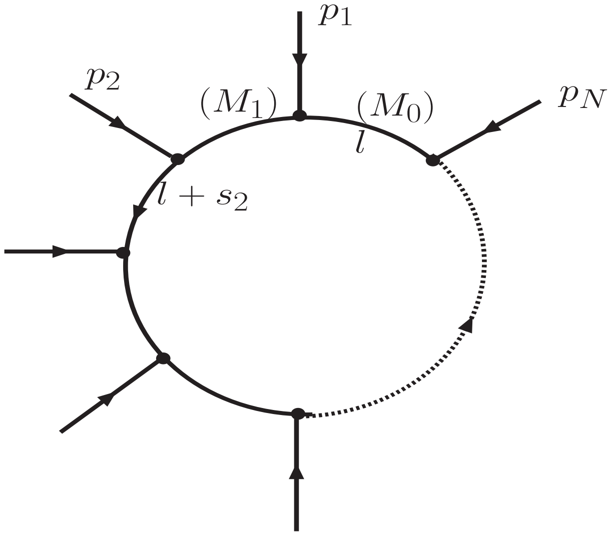

Figure 2.2: General structure of the one-loop N-point integral. The figure is taken from the paper [21].

In general, the tensor integrals will be reduced to the scalar one-loop one-, two-, three-, four-point functions. In GRACE-Loop, the reduction for tensor one-loop $N \leq 4$ integrals is performed by solving a system of equations which are obtained by taking derivatives of Feynman parameters. Noted that the reduction approach is different from PV, Brown-Feynman reduction as well as on-shell methods. Moreover, the tensor one-loop five- and six-point functions will be represented in terms of the tensor one-loop four-point integrals in following the improved Brown-Feynman approach. The following section will discuss the reduction method in more detail.

2.4.1 Scalar one-loop $N \leq 4$ point integrals

For scalar one-loop one-point function, the analytical solution has been well-known

$$A_0 = \int \frac{d^n l}{i(2\pi)^n} \frac{1}{l^2 - M_A^2} = \frac{1}{16\pi^2} M_A^2 (C_{UV} - \log(M_A^2) + 1), \tag{2.33}$$

where $C_{UV} = 1/\varepsilon + \gamma_E - \log(4\pi)$.

Scalar one-loop two-point function reads

$$B_0 = \int \frac{d^n l}{i(2\pi)^n} \frac{1}{[l^2 - M_A^2][(l+q)^2 - M_B^2)]}. \tag{2.34}$$

Performing Feynman's parameterization, one obtains

$$B_0 = \int \frac{d^n l}{i(2\pi)^n} \int_0^1 dx \frac{1}{[l^2 - \mathcal{D}_2(x)]^2}, \tag{2.35}$$

where $\mathcal{D}_2(x) = (1-x)M_A^2 + xM_B^2 - x(1-x)s$ with $s = q^2$.

The loop momentum integral will be integrated out firstly as

$$\int \frac{d^n l}{i(2\pi)^n} \frac{1}{[l^2 - \mathcal{D}_2(x)]^2} = \frac{1}{16\pi^2}(C_{UV} - \log \mathcal{D}_2(x)). \tag{2.36}$$

The B_0 is cast into the form

$$B_0 = \int_0^1 dx \, \frac{1}{16\pi^2}(C_{UV} - \log \mathcal{D}_2(x)) = \frac{1}{16\pi^2}(C_{UV} - F_0(M_A^2, M_B^2, q^2)),$$

where the analytical formula for $F_0(M_A^2, M_B^2, q^2)$ is presented in appendix E.

For the scalar one-loop three- and four-point functions (C_0 and D_0 respectively), GRACE-Loop uses the packages named LoopTools and FF for numerical evaluation. It is worth mentioning that the program also uses homemade one-loop package for cross-checking with LoopTools and FF when it is needed. It is fully numerical calculation of scalar one-loop integrals up to six points as well as two-loop up to four-point integrals which is based on Direct Computational Method [62, 63, 64, 65, 66].

2.4.2 Tensor one-loop 2-point reduction

This is the simplest case, we can obtain the analytical formula directly as following steps

$$B_{\mu;\mu\nu} = \int \frac{d^n l}{i(2\pi)^n} \frac{N(l)}{[l^2 - M_A^2][(l+q)^2 - M_B^2)]}, \tag{2.37}$$

where $N(l) = l_\mu,\ l_\mu l_\nu$. Performing Feynman's parameterization, one then makes a loop momenta shift $l \to l + qx$. The tensor one-loop two-point can be casted into the form

$$B_{\mu;\mu\nu} = \int \frac{d^n l}{i(2\pi)^n} \int_0^1 dx \frac{N(l)}{[l^2 - \mathcal{D}_2(x)]^2}, \tag{2.38}$$

where N now depends on the momenta l, q and the Feynman parameter. The loop momentum integral will be performed firstly by applying

$$\begin{aligned}
\int \frac{d^n l}{i(2\pi)^n} \frac{1}{[l^2 - \mathcal{D}_2(x)]^2} &= \frac{1}{16\pi^2}(C_{UV} - \log \mathcal{D}_2(x)), &(2.39)\\
\int \frac{d^n l}{i(2\pi)^n} \frac{l^2}{[l^2 - \mathcal{D}_2(x)]^2} &= \frac{1}{16\pi^2} 2\mathcal{D}_2(C_{UV} + \frac{1}{2} - \log \mathcal{D}_2(x)), &(2.40)\\
\int \frac{d^n l}{i(2\pi)^n} \frac{l^\mu l^\nu}{[l^2 - \mathcal{D}_2(x)]^2} &= \frac{1}{16\pi^2} \frac{\mathcal{D}_2}{2}(C_{UV} + 1 - \log \mathcal{D}_2(x))\ g^{\mu\nu}. &(2.41)
\end{aligned}$$

Then the integrals of the Feynman parameter are taken,

$$\int_0^1 dx \mathcal{D}_2 = \frac{1}{2}(M_A^2 + M_B^2) - \frac{s}{6}; \quad F_n(M_A^2, M_B^2, q^2) = \int_0^1 dx\ x^n\ \log \mathcal{D}_2(x), \tag{2.42}$$

where $F_n(M_A^2, M_B^2, q^2)$ is shown in appendix E.

2.4.3 Tensor one-loop 3-, and 4-points reduction

Using Feynman's parameterization one combines all propagators in the tensor one-loop N-point integrals of rank M in such a way

$$\begin{aligned}
\frac{1}{D_0 D_1 \cdots D_{N-1}} &= \Gamma(N) \int [dx] \frac{1}{\Big(D_1 x_1\ +\ D_2 x_2 + \cdots D_0(1 - \sum_{i=1}^{N-1} x_i)\Big)^N},\\
\text{with} \quad \int [dx] &= \int_0^1 dx_1 \int_0^{1-x_1} dx_2 \cdots \int_0^{1-\sum\limits_{i=1}^{N-2} x_i} dx_{N-1}. &(2.43)
\end{aligned}$$

The tensor one-loop N-point integrals can be written in a compact formula

$$
\begin{aligned}
T^{(N)}_{\underbrace{\mu\nu\cdots\rho}_{M}} &= \Gamma(N)\int [dx]\, \mathcal{T}^{(N)}_{\underbrace{\mu\nu\cdots\rho}_{M}}, \quad \text{with} \\
\mathcal{T}^{(N)}_{\underbrace{\mu\nu\cdots\rho}_{M}} &= \int \frac{d^n l}{(2\pi)^n} \frac{l_\mu l_\nu \cdots l_\rho}{\left(l^2 - 2l.P(x_i) - M^2(x_i)\right)^N}, \quad M \leq N. \qquad (2.44)
\end{aligned}
$$

Integration over the loop momentum l is done firstly. One then obtains

$$
\begin{aligned}
\mathcal{T}^{(N)} &= \widetilde{\mathcal{T}}^{(N)}\Gamma(N-n/2) \quad \text{with} \quad \widetilde{\mathcal{T}}^{(N)} = \frac{(-1)^N i\pi^{n/2}}{(2\pi)^n\Gamma(N)}\Delta^{-(N-n/2)}, \\
\mathcal{T}^{(N)}_{\mu} &= \mathcal{T}^{(N)} P_\mu, \\
\mathcal{T}^{(N)}_{\mu\nu} &= \widetilde{\mathcal{T}}^{(N)}\left(\Gamma(N-n/2)P_\mu P_\nu - \frac{1}{2}g_{\mu\nu}\Delta\Gamma(N-1-n/2)\right), \qquad (2.45) \\
\mathcal{T}^{(N)}_{\mu\nu\rho} &= \widetilde{\mathcal{T}}^{(N)}\left(\Gamma(N-n/2)P_\mu P_\nu P_\rho - \frac{\Delta}{2}(g_{\mu\nu}P_\rho + g_{\mu\rho}P_\nu + g_{\nu\rho}P_\mu)\Gamma(N-1-n/2)\right), \\
\mathcal{T}^{(N)}_{\mu\nu\rho\sigma} &= \widetilde{\mathcal{T}}^{(N)}\Bigg(\Gamma(N-n/2)P_\mu P_\nu P_\rho P_\sigma + \frac{\Delta^2}{4}(g_{\mu\nu}g_{\rho\sigma} + g_{\mu\rho}g_{\nu\sigma} + g_{\mu\sigma}g_{\nu\rho})\Gamma(N-2-n/2) \\
&\quad - \frac{\Delta}{2}(g_{\mu\nu}P_\rho P_\sigma + g_{\mu\rho}P_\nu P_\sigma + g_{\mu\sigma}P_\nu P_\rho + \text{permutaion terms})\Gamma(N-1-n/2)\Bigg),
\end{aligned}
$$

where

$$
\begin{aligned}
\Delta &= \sum_{i,j=1}^{N-1} Q_{ij}x_i x_j + \sum_{i=1}^{N-1} L_i x_i + \Delta_0, \quad Q_{ij} = s_i.s_j, \quad L_i = -s_i^2 + (M_i^2 - M_0^2), \\
\Delta_0 &= M_0^2, \quad P = -\sum_{i=1}^{N-1} s_i x_i. \qquad (2.46)
\end{aligned}
$$

It turns all tensor integrals into Feynman parameters space. All these parametric integrals will be classified into

$$
I^{(N)}_{\underbrace{i\cdots k}_{M}} = \int [dx]\frac{x_i\cdots x_k}{\Delta^{(N-2)}} \quad \text{and} \quad J^{(N)}_{i;\alpha} = \int [dx] x_i^\alpha \log\Delta \quad \text{with} \quad \alpha = 0, 1. \qquad (2.47)
$$

The issue is now finding the solutions for these parametric integrals. It is important to note that the appearance of the integrals $J^{(N)}_{i;\alpha}$ from expanding Eq. (2.45) around $n = 4 - 2\varepsilon$. The integrals come from the ε independent terms in $\varepsilon(1/\varepsilon + \mathcal{O}(\varepsilon^{0,1}))$.

In the realistic calculation one needs $J^{(4)} = J^{(4)}_{i;0}$ and $J^{(3)}_{i;(0,1)}$. All these integrals are derived recursively. As a result, the parametric integrals will be expressed eventually in terms of the scalar integrals.

For example, let us consider the case of $I^{(N)}_{\underbrace{i\cdots k}_{M}}$ for the box integrals, the trick is that one uses

$$\int [dx]\, \partial_i \left(\frac{x_k^\alpha x_l^\beta x_m^\gamma}{\Delta} \right), \quad \text{with} \quad \partial_i = \frac{\partial}{\partial x_i}, \quad 1 \le \alpha+\beta+\gamma = M \le N-1.$$

One then arrives at the relation

$$\begin{aligned}\partial_i \left(\frac{x_k^\alpha x_l^\beta x_m^\gamma}{\Delta} \right) &= -\frac{x_k^\alpha x_l^\beta x_m^\gamma}{\Delta^2}(L_i + 2\sum_j Q_{ij}x_j) + \frac{1}{\Delta^2}\left(\Delta_0 + \sum_j L_j x_j + \sum_{jn} Q_{jn}x_j x_n \right) \times \\ & \left(\alpha x_k^{\alpha-1} x_l^\beta x_m^\gamma \delta_{ki} + \beta x_l^{\beta-1} x_k^\alpha x_m^\gamma \delta_{li} + \gamma x_m^{\gamma-1} x_k^\alpha x_l^\beta \delta_{mi} \right) \end{aligned} \tag{2.48}$$

The terms in the left-hand side can be expressed in terns of the triangle integrals with rank $M \le 3$. In the right-hand side the terms of the coefficient of L_i are the box integrals of rank M. While the terms with coefficient of Δ_0 are the box integrals of rank $M-1$. All these terms will be combined into the $C_{i;jkl}$. Finally, the terms proportional to Q_{ij} are identified as the boxes with rank $M+1$ which one then would like to derive.

For furthermore detail, considering the box with rank $M = 4$, one applies the relation for the case of $\alpha = \beta = \gamma = 1$ ($M = 3$). As a consequence, the integrals $I^{(4)}_{ijkl}$ can be expressed as

$$\begin{aligned} C_{i;klm} &= -2\sum_j Q_{ij} I^{(4)}_{jklm} + \sum_{jn} Q_{jn} \left(\delta_{ki} I^{(4)}_{jnlm} + \delta_{li} I^{(4)}_{jnkm} + \delta_{mi} I^{(4)}_{jnkl} \right), \\ I^{(4)}_{ijkl} &= \int [dx] \frac{x_i x_j x_k x_l}{\Delta^2}. \end{aligned} \tag{2.49}$$

By solving a system of equations for the parametric box integrals with rank $M+1$, one can express it in terms of the parametric box integrals with rank $M-1$ and M and the parametric triangle with rank M. Therefore all the integrals $I^{(N)}_{\underbrace{i\cdots k}_{M}}$ are derived recursively and can be written in terms of the scalar integrals eventually.

The parametric integrals $J^{(4)}$ can be also reduced into the triangle and the box integrals with lower rank by using the same previous trick,

$$x_i^\alpha \log \Delta_N \;=\; \frac{1}{N+\alpha-1}\sum_{j=1}^{N-1}\left\{\partial_j\left(x_i^\alpha x_j \log \Delta_N\right) - x_i^\alpha x_j \partial_j\left(\log \Delta_N\right)\right\} \quad (2.50)$$

Applying this relation for the box with $\alpha = 0$ and triangle integrals with $\alpha = 0, 1$, one has

$$\begin{aligned}
x_i \log \Delta &= \frac{1}{3}\sum_{j=1}^{2}\left\{\partial_j\left(x_i x_j \log \Delta\right) - x_i + \frac{x_i(L_j x_j + \Delta_0)}{\Delta}\right\}, N=3,\ \alpha=1 \\
\log \Delta &= \frac{1}{2}\sum_{j=1}^{2}\left\{\partial_j\left(x_j \log \Delta\right) - 1 + \frac{L_j x_j + \Delta_0}{\Delta}\right\}, N=3,\ \alpha=0 \qquad (2.51)\\
\log \Delta &= \frac{1}{3}\sum_{j=1}^{3}\left\{\partial_j\left(x_j \log \Delta\right) - \frac{2}{3} + \frac{\Delta(L_j x_j + 2/3\Delta_0)}{\Delta^2}\right\}, N=4,\ \alpha=0
\end{aligned}$$

The first terms in the right-hand side of these relations are desired to derive. These relations in Eq. (2.51) show clearly that all $J^{(4)}$ can be represented in terms of the lower integrals $J^{(3)}_{i;1}$ and $I^{(4)}_{M=0,1,2,3}$. In addition, all $J^{(3)}_{i;(0,1)}$ are written in terms of two-point functions and the integrals $I^{(3)}_{M=0,1,2}$.

2.4.4 Tensor one-loop 5-point reduction

The tensor one-loop five point functions will be reduced into tensor one-loop four-point functions. The method used in GRACE-Loop will be presented in this section. The general idea that all the external momenta are not linearly independent in the case $N > 4$. For $N = 5$ as an example, the vectors $\{s_i\}$ with $i = 1, \cdots 4$, set an independent basis of 4-vectors. As a result, one can represent any 4-momentum, particular the loop momentum l as

$$l^\mu = \sum_{i,j=1}^{4}(Q^{-1})_{ij}(l\cdot s_i)s_j^\mu, \qquad (2.52)$$

where the 4×4 matrix Q_{ij} is defined as in Eq. (2.46) with $i, j = 1, \cdots 4$. We express l^2 as

$$l^2 = \sum_{i,j=1}^{4} (Q^{-1})_{ij} (l \cdot s_i)(l \cdot s_j). \tag{2.53}$$

From the relation in Eq. (2.53), one can derive the representation between the propagators in the 5-point function as follows

$$D_0 + M_0^2 = \frac{1}{2} \sum_{i,j=1}^{4} (Q^{-1})_{ij} (D_i - D_0 + L_i)(l \cdot s_j), \tag{2.54}$$

to arrive at the identity

$$4M_0^2 - \sum_{i,j=1}^{4} (Q^{-1})_{ij} (L_i)(D_j - D_0 + L_j) = -4D_0 + 2 \sum_{i,j=1}^{4} (Q^{-1})_{ij} (D_i - D_0)(l \cdot s_j). \tag{2.55}$$

It demonstrates clearly that a 5-point function with a numerator of the form $N(l) = l^{\mu_1} \cdots l^{\mu_k}$ is written in terms of the box integrals,

$$\left(4M_0^2 - \sum_{i,j=1}^{4} (Q^{-1})_{ij} L_i L_j \right) \int \frac{d^4 l}{(2\pi)^4 i} \frac{N(l)}{\mathcal{D}_5} = \tag{2.56}$$
$$\int \frac{d^4 l}{(2\pi)^4 i} N(l) \left(-\frac{4D_0}{\mathcal{D}_5} + \sum_{i,j=1}^{4} (Q^{-1})_{ij} L_i \frac{D_j - D_0}{\mathcal{D}_5} + 2 \sum_{i,j=1}^{4} (Q^{-1})_{ij} \frac{(D_i - D_0)(l \cdot s_j)}{\mathcal{D}_5} \right),$$

with $\mathcal{D}_5 = D_0 \prod_{i=1}^{4} D_i$.

This reduction technique can present five point functions to the box integrals completely. However, it is important to note that the appearance of the term $l \cdot s_j$ in Eq. (2.56) raises the rank of the integral by a unit. As a consequence, a superficial UV divergence in the box integrals in the case of $M \geq 3$. In addition, for $M = 4$ as a example, the reduction requires the evaluation of $M = 5$ box diagrams. These box integrals with rank $M = 5$ are not covered in the tensor box integrals reduction, see the previous section.

Furthermore the matrix elements in GRACE-Loop will be written in a symbolic way, the resultant **FORTRAN** code usually becomes very lengthy in this reduction technique. Another technique for the reduction of higher rank tensors has been developed by applying the identity Eq. (2.52) to the numerator $N(l)$ directly in such a way

$$\begin{aligned} N(l) &= l^{\mu_1} l^{\mu_2} \cdots l^{\mu_k} = \sum_{i,j=1}^{4} (Q^{-1})_{ij} (l \cdot s_i) s_j^{\mu_1} l^{\mu_2} \cdots l^{\mu_k}, \\ &= \frac{1}{2} \sum_{i,j=1}^{4} (Q^{-1})_{ij} (D_i - D_0 + L_i) s_j^{\mu_1} l^{\mu_2} \cdots l^{\mu_k}. \end{aligned} \tag{2.57}$$

Then

$$\begin{aligned} \int \frac{d^4 l}{(2\pi)^4 i} \frac{N(l)}{\mathcal{D}_5} &= \frac{1}{2} \sum_{i,j=1}^{4} (Q^{-1})_{ij} s_j^{\mu_1} \int \frac{d^4 l}{(2\pi)^4 i} \frac{(D_i - D_0) l^{\mu_2} \cdots l^{\mu_k}}{\mathcal{D}_5} \\ &+ \frac{1}{2} \sum_{i,j=1}^{4} (Q^{-1})_{ij} L_i s_j^{\mu_1} \int \frac{d^4 l}{(2\pi)^4 i} \frac{l^{\mu_2} \cdots l^{\mu_k}}{\mathcal{D}_5}. \end{aligned} \tag{2.58}$$

The second term in the right-hand-side still remains a sum of 5-point functions with rank reducing a unit. The reduction is repeated until arriving at scalar one-loop 5-point function and the box integrals. This method is called the *vector-derived* reduction. An advantage of this method is that the final expression in **FORTRAN** code is about ten times shorter than that obtained by the previous technique. This point is discussed in concrete in Ref [21].

2.5 Tensor one-loop 5-point reduction in LoopTools

In this section, we discuss briefly the tensor reduction one-loop five point functions in Ref [16]. In this method, the tensor one-loop integrals up to rank five will be decomposed into the Lorentz-covariant structure as

$$
\begin{aligned}
T^{N,\mu} &= \sum_{i_1=1}^{N-1} p^{\mu}_{i_1} T^N_{i_1}, \qquad T^{N,\mu\nu} = \sum_{i_1,i_2=1}^{N-1} p^{\mu}_{i_1} p^{\nu}_{i_2} T^N_{I_1 I_2} + g^{\mu\nu} T^N_{00}, \\
T^{N,\mu\nu\rho} &= \sum_{i_1,i_2,i_3=1}^{N-1} p^{\mu}_{i_1} p^{\nu}_{i_2} p^{\rho}_{i_3} T^N_{i_1 i_2 i_3} + \sum_{i_1=1}^{N-1} \{gp\}^{\mu\nu\rho}_{i_1} T^N_{00 i_1}, \\
T^{N,\mu\nu\rho\sigma} &= \sum_{i_1,i_2,i_3,i_4=1}^{N-1} p^{\mu}_{i_1} p^{\nu}_{i_2} p^{\rho}_{i_3} p^{\sigma}_{i_4} T^N_{i_1 i_2 i_3 i_4} + \sum_{i_1,i_2=1}^{N-1} \{gpp\}^{\mu\nu\rho\sigma}_{i_1 i_2} T^N_{00 i_1 i_2} \\
&\quad + \{gg\}^{\mu\nu\rho\sigma} T^N_{0000}, \\
T^{N,\mu\nu\rho\sigma\tau} &= \sum_{i_1,i_2,i_3,i_4,i_5=1}^{N-1} p^{\mu}_{i_1} p^{\nu}_{i_2} p^{\rho}_{i_3} p^{\sigma}_{i_4} p^{\tau}_{i_5} T^N_{i_1 i_2 i_3 i_4 i_5} + \sum_{i_1,i_2,i_3=1}^{N-1} \{gppp\}^{\mu\nu\rho\sigma\tau}_{i_1 i_2 i_3} T^N_{00 i_1 i_2 i_3} \\
&\quad + \sum_{i_1=1}^{N-1} \{ggp\}^{\mu\nu\rho\sigma\tau}_{i_1} T^N_{0000 i_1}.
\end{aligned} \tag{2.59}
$$

where the following notations are used

$$
\begin{aligned}
\{p\ldots p\}^{\mu_1\ldots\mu_P}_{i_1\ldots i_P} &= p^{\mu_1}_{i_1} \ldots p^{\mu_P}_{i_P}, \\
\{gg\}^{\mu\nu\rho\sigma} &= g^{\mu\nu} g^{\rho\sigma} + g^{\nu\rho} g^{\mu\sigma} + g^{\rho\mu} g^{\nu\sigma}, \\
\{gp\}^{\mu\nu\rho}_{i_1} &= g^{\mu\nu} p^{\rho}_{i_1} + g^{\nu\rho} p^{\mu}_{i_1} + g^{\rho\mu} p^{\nu}_{i_1}, \\
\{gpp\}^{\mu\nu\rho\sigma}_{i_1 i_2} &= g^{\mu\nu} p^{\rho}_{i_1} p^{\sigma}_{i_2} + g^{\mu\rho} p^{\sigma}_{i_1} p^{\nu}_{i_2} + g^{\mu\sigma} p^{\nu}_{i_1} p^{\rho}_{i_2} + g^{\nu\rho} p^{\sigma}_{i_1} p^{\mu}_{i_2} + g^{\rho\sigma} p^{\nu}_{i_1} p^{\mu}_{i_2} + g^{\sigma\nu} p^{\rho}_{i_1} p^{\mu}_{i_2},
\end{aligned} \tag{2.60}
$$

The $T^N_{i_1 i_2 \ldots}$ are called tensor coefficient integrals. These tensors will be reduced into the scalar one-loop integrals by numerically stable reduction [16]. The method is the improved PV method in order to get the numerical stability when the inverse Gram determinant problems happen. **We implement this method into GRACE-Loop. It provides an useful subroutine to cross check the result on five-point functions by comparing this method to the current one in GRACE-Loop.**

The reduction method for the one-loop five-point functions in GRACE-Loop is also cross-checked with the one in Ref [16] by calculating the amplitude of the diagrams in figure (2.3). Table 2.3 shows the numerical check at an arbitrary phase space point. The results in two methods are in good agreement over a range of 24 digits.

Reduction	$2\Re(\mathcal{M}_{Loop}\mathcal{M}^{+}_{Tree})$
GRACE-Loop	$-2.038745980639938993001525372641855 \cdot 10^{-6}$
Ref [16]	$-2.038745980639938993001528930735675 \cdot 10^{-6}$

Table 2.3: Test of the reduction of the one-loop five-point functions in GRACE-Loop in comparison with the method in Ref [16].

2.6 Test on the calculation with GRACE-Loop

The result of calculation will be checked by consistency tests. There are test of ultraviolet, infrared finiteness, and independence of the gauge parameters. The tests are verified numerically at the amplitude level at several arbitrary phase space points (accepted for k_c stability check). In appendix C the numerical checks are presented at one phase space point.

Once the numerical checks are performed successfully, the physical results for the studied processes can proceed. For the given purpose, one sets $C_{UV} = 0$, $\zeta = (0, 0, 0, 0, 0)$ and $\lambda = 10^{-17}$ GeV as well as $k_c = 10^{-3}$ GeV as the default values.

2.6.1 Ultraviolet finiteness

The first test concerns ultraviolet finiteness of the result. As a result of renormalisation procedure, the counterterm diagrams are taken into account in one-loop correction calculations. The result then must be independent of dimensional regularization parameter (C_{UV}). The test is performed numerically by changing C_{UV}, the results of the squared amplitude are usually stable over 30 digits in quadruple precision calculation.

2.6.2 Infrared finiteness

Beside the UV divergence, one-loop integrals have also infrared divergence which involves loop diagrams with photon exchange between two on-shell particles. In order

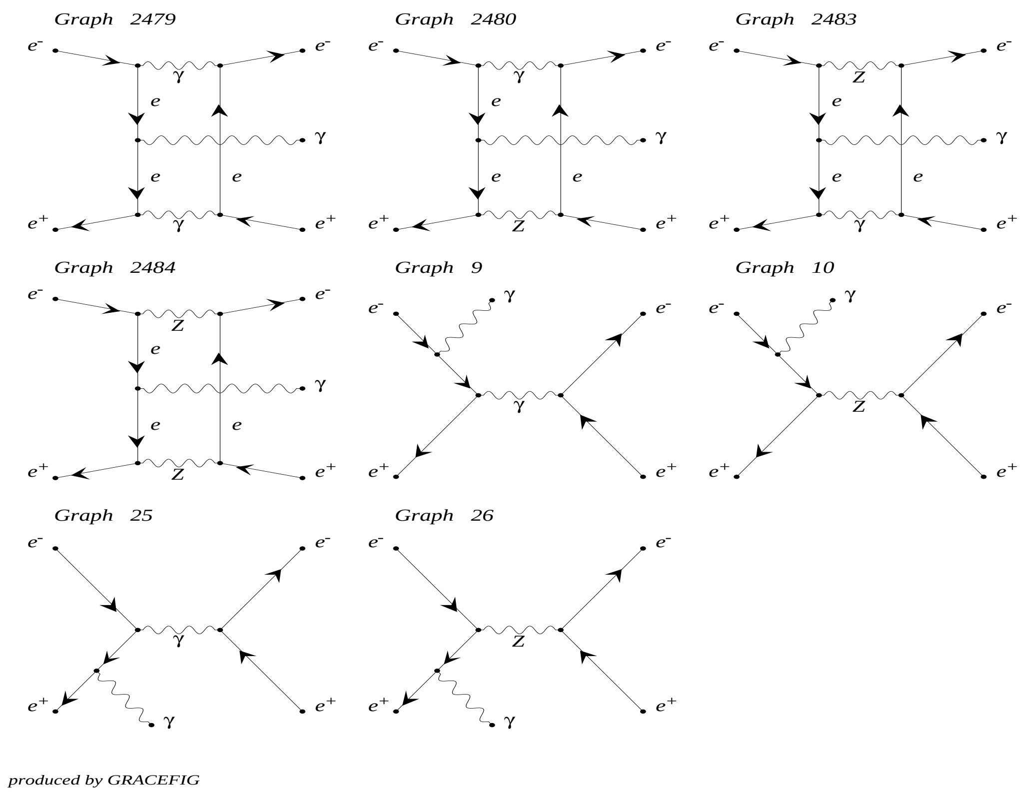

Figure 2.3: Feynman diagrams in the process $e^+e^- \rightarrow e^+e^-\gamma$ generated by the GRACE-Loop program.

to regularize the IR divergence, one introduces an infinitesimal photon mass λ. As a consequence, the results depend on the fictitious photon mass. The λ dependence should be canceled against when one includes the soft photon bremsstrahlung.

The soft photon bremsstrahlung can be factorized as

$$d\sigma_{\text{soft}}(\lambda, E_\gamma \le k_c) = d\sigma_0 \times \delta_{\text{soft}}(\lambda, E_\gamma \le k_c), \tag{2.61}$$

where k_c the soft cutoff energy parameter. The soft factor $\delta_{\text{soft}}(\lambda, E_\gamma \le k_c)$ is explained as the probability of emitting a photon with mass λ and the energy $E_\gamma \le k_c$ from charged particles. The soft factor is completely determined from the classical current of a charged particles without involving the spin connection.

$$\delta_{\text{soft}} = -e^2 \int_{|k|<k_c} \frac{d^3k}{2E_\gamma(2\pi)^3} \sum_{ij} \varepsilon_i \varepsilon_i Q_i Q_j \frac{p_i.p_j}{(k.p_i)(k.p_j)} = \sum_{ij} R_{ij} \ , \quad E_\gamma = \sqrt{k^2+\lambda^2},$$

where $\varepsilon_i = \pm 1$ are used for incoming $(+1)$ or outgoing (-1) particles. A general expressions for R_{ij} have been found in Ref [67]. A few special cases have been calculated in detail in Ref [68]. For example, the diagonal term R_{ii} from a charged particle with $|Q| = 1$ with momentum $p = (E, \overrightarrow{p}), \quad p^2 = m^2$ and $P = |\overrightarrow{p}|$, can be evaluated as

$$R_{ii} = -e^2 \int_{|k|<k_c} \frac{d^3k}{2E_\gamma(2\pi)^3} \frac{m^2}{(k.p)^2} = -\frac{\alpha}{\pi} \left\{ \ln\left(\frac{2k_c}{\lambda}\right) + \frac{E}{P} \ln\left(\frac{m}{E+P}\right) \right\} . \quad (2.62)$$

The test is done numerically by changing λ, the result is stable over 20 digits in quadruple precision calculation. The $k_c = 10^{-3}$ GeV is a default value for this test.

2.6.3 Gauge-parameters independence checks

The results are also independent of non-linear gauge parameters $\zeta = (\tilde{\alpha}, \tilde{\beta}, \tilde{\kappa}, \tilde{\delta}, \tilde{\epsilon})$. This test is performed by fixing $C_{UV} = 0$, and $\lambda = 10^{-17}$ GeV. By changing the value of ζ, it is expected that the results will be stable over 20 digits when quadruple precision is used.

2.6.4 k_c stability

Full one-loop radiative corrections must consider the hard photon bremsstrahlung. These processes are generated by GRACE-tree version via the helicity amplitude method. The k_c stability of the result is checked at cross section level. By changing the k_c from 10^{-5} GeV to 0.1 GeV, the sum of soft and hard photon bremsstrahlung cross section must be in agreement to an accuracy better then the statistical error in Monte Carlo integration.

Chapter 3

Full one-loop electroweak radiative corrections to the W-pair production in association with a jet at the LHC

This chapter presents an overview of the Large Hadron Collider (LHC). We then report the calculation of one-loop electroweak corrections to the W-pair and the W-pair productions in association with a jet at the LHC. In the physical results, the impact of electroweak corrections to the total cross section and its relevant distributions are studied in the full energy reach of future LHC.

3.1 The Large Hadron Collider

The Large Hadron Collider is the world's largest and most powerful particle accelerator. It is a proton-proton colliding accelerator with center-of-mass energy up to 14 TeV. The LHC has been constructed by the European Organization for Nuclear

Research (CERN) from 1998 to 2008. The operation of LHC started in September 2008. Its purpose is to allow physicists to discriminate different theories of elementary particles, such as the SM, SUSY, etc.

The LHC consists of a ring of 27-kilometer super-conducting magnets. It accelerates two proton beams to collide at four main dectors: ATLAS, CMS, LHCb, and ALICE.

- ATLAS: is one of two general purpose detectors at the LHC. It is used to search for the Higgs boson (to explain the origins of the mass) and new physics such as SUSY, Extra-Dimension, etc.
- CMS: is also a general purpose particle detector, like ATLAS, and it is designed to hunt for the Higgs boson as well as to search for the evidence of dark matter in the Universe and other signals of physics beyond SM.
- LHCb: (Large Hadron Collider beauty) is one of the particle detectors at the LHC. LHCb is designed to study B-physics, that is measuring the parameters of CP violation. It helps us to understand the slight differences between matter and anti-matter in the Universe.
- ALICE: (A Large Ion Collider Experiment) is a detector for heavy-ion collision at the LHC. It mainly focuses on studying the strongly interacting matter at extreme energy density (so-called quark-gluon plasma phase).

The number of events per second, which is generated in the LHC [69, 70], is obtained by

$$N_{\mathbf{events}} = L \cdot \sigma_{\mathbf{events}}, \tag{3.1}$$

where $\sigma_{\mathbf{events}}$ is the cross section of corresponding events. The factor L is the machine luminosity depending on beam parameters. The machine luminosity can be derived for a Gaussian beam distribution as

$$L = \frac{N_b^2 n_b f_{\mathbf{rev}} \gamma_r}{4\pi \epsilon_n \beta^*} F. \tag{3.2}$$

Table 3.1: LHC beam parameters relevant for the peak luminosity [69]

Number of particles per bunch (N_b)	1.6×10^{11}
Number of bunches per beam (n_b)	1380
Revolution frequency (f_{rev})	11245Hz
Relativistic gamma (γ_r)	7461 ($E = 7$TeV)
Normalized transverse emittance (ϵ_n)	2.2–2.5×10^{-4}cm
Full crossing angle at the IP (θ_c) for ATLAS/CMS	290 μrad
RMS bunch length (σ_z)	> 9cm
Transverse RMS beam size (σ^*) at ATLAS/CMS	19μm
Geometric luminosity reduction factor (F) at ATLAS/CMS	0.84
Optical beta function at ATLAS/CMS (β^*)	60cm

In this formula, N_b is the number of particles in a bunch, n_b is the number of bunches in a beam, $f_{\mathbf{rev}}$ is the revolution of frequency, γ_r is the relativistic gamma factor, ϵ_n is the normalized transverse beam emittance, and β^* is the beta function at the collision point. The factor F is the geometric luminosity reduction factor deal to the crossing angle at the interaction point (IP) as

$$F = 1/\sqrt{1 - \left(\frac{\theta_c \sigma_z}{2\sigma^*}\right)^2}, \tag{3.3}$$

where θ_c is the full crossing angle at the IP, σ_z is the root-mean-square (RMS) bunch length and σ^* is the RMS beam size at the IP.

In Table 3.1, we list the beam parameters which are required to reach the peak of luminosity at the LHC. ATLAS and CMS are to get the peak luminosity of L (ATLAS and CMS) $= 10^{34} cm^{-2} s^{-1}$ (It plans to get $\sim 3000\text{fb}^{-1}$ in 2023). LHCb for B-physics goal is to reach at the peak luminosity of L(LHCb)$= 10^{32} cm^{-2} s^{-1}$ and ALICE reach the peak luminosity of L (ALICE) $= 10^{27} cm^{-2} s^{-1}$.

In July 2012, the ATLAS and CMS experiments announced the discovery of a new boson whose properties were consistent with the SM Higgs boson [1, 2, 3, 4, 5, 6]. The mass of the new boson was reported by two experiments as:

- ATLAS: 126.0 ± 0.4(stat.)± 0.4(sys.) GeV;
- CMS: 125.3 ± 0.4(stat.)± 0.4(sys.) GeV.

Figure 3.1 shows the signal of the new boson reported by the ATLAS and CMS experiments. The figures are taken in Refs [1, 2]. After discovering the SM-like Higgs boson, the goals of LHC physics [12, 13] at 13 TeV and 14 TeV are

- precise study of the newly discovered Higgs boson properties such as mass, spin, Yukawa couplings, self coupling, etc. These measurements play a major role to open a portal to BSM physics.
- study for electroweak processes: vector boson and diboson productions in association with jets will be collected. The processes are important for understanding the background of Higgs boson and BSM searches. The measurements will also improve the future precision of vector boson properties.
- precise measurements of top quark properties and top quark electroweak couplings. It is potential to probe the new physics effects.
- searches for new physics signals such as SUSY, and extra-dimensions, etc.

Higher order QCD and electroweak corrections to relevant processes are mandatory for the future program at the LHC. In this thesis, we focus on full one-loop electroweak corrections to the W-pair and W-pair in association with a jet productions at the LHC. The motivation for these calculations are presented in the next section.

3.2 Motivation of the calculation

As discussed in the previous section, the W-pair and W-pair in association with a jet productions at the Large Hadron Collider play a major role to test the Standard

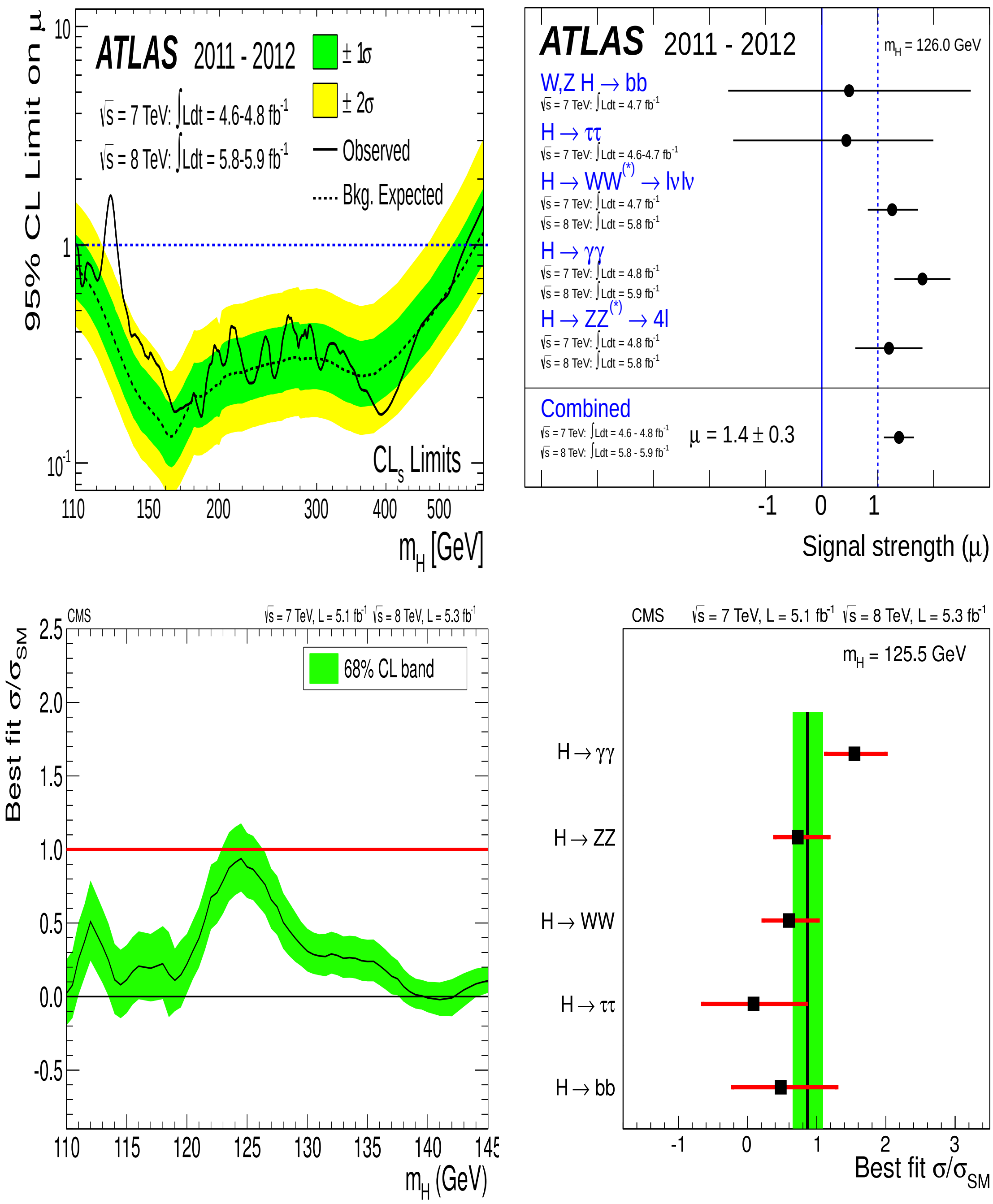

Figure 3.1: ATLAS and CMS experiments reported evidence for new boson.

theory structure at high energy as well as to search for new physics from the observation of anomalous couplings of gauge bosons (coupling of W, Z, γ). Beside that these productions also significantly contribute to background for Higgs boson searches which decay into a W-boson pair. Last but by no means least, the productions form a massive background to new-physics searches, such as SUSY particles, because of leptons and missing transverse momenta from the W decays.

In order to match the high precision of experimental data with future high luminosity of the LHC, precise calculations to these productions are greatly considered. Full one-loop QCD corrections to the process $pp \to W^-W^+$ at Hadron Colliders were performed by many authors [71, 72]. In addition, full one-loop QCD corrections to $pp \to W^-W^+ + 1$ jet were evaluated in Ref [73]. One finds that full $\mathcal{O}(\alpha_s)$ corrections are order 10% contribution to the lowest order cross section from these reports. It is clear that two-loop QCD and one-loop electroweak corrections to these production must be taken into account at the high precision program of future LHC.

The perspectives of present calculation are as follows. High energy experiment in the future LHC where energy scale far above the electroweak scale, the one-loop electroweak radiative corrections make significant contributions. These corrections are dominated by single and double logarithms with argument of ratio between the energy scale and weak boson masses. The logarithm functions appear once evaluating the diagrams in which the virtual or real gauge bosons are radiated by external legs. Such corrections are considered with order of two-loop QCD corrections.

For the above reasons, the full one-loop electroweak corrections to these productions are proposed by several groups. For given examples, a high energy approximated method for evaluating one-loop electroweak radiative corrections to $pp \to W^-W^+$ were calculated in Refs [74, 75, 76] for many years ago. **Recently, the full electroweak corrections to this process were also performed in Refs [77, 78, 79]. A full $\mathcal{O}(\alpha)$ electroweak radiative corrections to $pp \to W^+W^- + 1$ jet at LHC have so far not been computed. This chapter devotes to such calculation.**

One then examines the impact of electroweak corrections to the total cross section and its relevant distributions in the full energy reach of future LHC.

3.3 Calculation of $pp \to W^+W^- + 1$ jet at the LHC

The calculation of this process is presented in this section.

3.3.1 Setup of the calculation

The total cross section of the process $pp \to W^+W^- + 1$ jet at the Large Hadron Collider can be computed by using the factorization method which is described in Ref [80],

$$\sigma^{pp\to W^+W^-jet}_{\mathcal{O}(\alpha)}(s) = \sum_{a,b}\int_0^1 dx_a \int_0^1 dx_b\, f^h_a(x_a,\mu_F)\, f^h_b(x_b,\mu_F)\, \hat{\sigma}^{ab\to W^+W^-jet}_{\mathcal{O}(\alpha)}(\hat{s},\mu_F,\mu_R), \tag{3.4}$$

where

- $f^h_{a,b}(x_{a,b},\mu_F)$ are the parton distribution functions (PDFs), which depend on parton momentum fraction $x_{a,b}$ in the hadron h (h is proton in the case of LHC experiments), and on the factorization scale μ_F;

- $\hat{\sigma}^{ab\to W^+W^-jet}_{\mathcal{O}(\alpha)}(\hat{s},\mu_F,\mu_R)$ denotes for the parton-level cross section of the process that the parton 'a' and parton 'b' collide to produce W^+W^-jet. Here jet represents a quark or a gluon. The parton-level cross section, in general, depends on the factorization scale, renormalization scale (μ_R) and the partonic center-of-mass energy $\hat{s} = x_a x_b s$, where s is center-of-mass energy of pp collision.

A full electroweak corrections must take into account the one-loop virtual corrections as well as soft and hard photon bremsstrahlung. In general, the parton-level cross-section in full $\mathcal{O}(\alpha)$ electroweak radiative corrections can be written as

$$\begin{aligned} \hat{\sigma}_{\mathcal{O}(\alpha)}^{ab\to W^+W^-jet}(\hat{s},\mu_F,\mu_R) &= \int d\hat{\sigma}_{\mathbf{T}}^{ab\to W^+W^-jet} + \int d\hat{\sigma}_{\mathbf{V}}^{ab\to W^+W^-jet}(C_{UV},\zeta,\lambda) \\ &\quad +\delta_{\mathbf{soft}}(\lambda \le E_\gamma < k_c) \int d\hat{\sigma}_{\mathbf{T}}^{ab\to W^+W^-jet} \\ &\quad + \int d\hat{\sigma}_{\mathbf{H}}^{(ab\to W^+W^-jet)\gamma}(E_\gamma \ge k_c). \end{aligned} \tag{3.5}$$

In this formula $\hat{\sigma}_{\mathbf{T}}^{ab\to W^+W^-jet}$ is the tree-level cross-section of the parton-level process $ab \to W^+W^-jet$, $\hat{\sigma}_{\mathbf{V}}^{ab\to W^+W^-jet}$ is the cross-section due to the interference of the one-loop (including counterterms) and the tree diagrams of the corresponding process. As a result of renormalization procedure, the contribution $\hat{\sigma}_{\mathbf{V}}^{ab\to W^+W^-jet}$ must be independent of the ultraviolet cutoff parameter (C_{UV}). This part is also independent of the non-linear gauge parameters $\zeta =(\tilde{\alpha},\tilde{\beta},\tilde{\delta},\tilde{\epsilon},\tilde{\kappa})$, as discussed in Chapter 2. Because of the way we regularize the IR-divergences, $\hat{\sigma}_{\mathbf{V}}^{ab\to W^+W^-jet}$ must depend on the fictitious photon mass λ. The λ dependence of the result has to cancel against the soft photon bremsstrahlung contribution, the third term in Eq. (3.5). The soft part can be factorised into the soft factor in Eq. (2.62), and the cross section from the tree diagrams. Finally, one considers the contribution of the hard photon bremsstrahlung, the last term in Eq. 3.5, $\hat{\sigma}_{\mathbf{H}}^{(ab\to W^+W^-jet)\gamma}(E_\gamma \ge k_c)$. The hard photon is cross section of the process $ab \to W^+W^-jet + \gamma$, an additional photon γ with $E_\gamma \ge k_c$. By including hard photon contribution, the final results must be independent of photon energy cutoff parameter, k_c.

The steps of computing the cross section at the Hadron Collider in following the factorization method are clear from this point of view. Following the procedure, one first needs to generate all the partonic processes which contributed to the process $pp \to W^+W^- + 1$ *jet*. These partonic processes are classified in Table 3.2 where q denotes a quark: u,d,c,s,b; and g is a gluon.

Type	Patonic processes
1	$q\bar{q} \to W^+W^-\ g$
2	$qg \to W^+W^-\ q$
3	$\bar{q}g \to W^+W^-\ \bar{q}$

Table 3.2: The partonic processes contribute to the process $pp \to W^+W^- + 1$ jet at the LHC.

The current calculation does not consider the quark mixing. So that the processes in type 3 can be calculated by using the matrix element of the processes in type 2 with exchanging the PDFs from q to $\bar{q}$ in Eq. (3.4).

For the parton-level calculations, the GRACE-Loop program is employed to generate all these processes. Table (3.3) summarizes the number of Feynman diagrams of the partonic processes. Fig 3.2 shows some selected diagrams of the partonic process $u\bar{u} \to W^+W^-g$. The diagrams are counted in covariant gauge. $N_{\text{Tree diagrams}}$ is the number of tree diagrams. $N_{\text{Loop diagrams}}$ is that of the sum of one-loop and counterterm diagrams.

type	processes	$N_{\text{Tree diagrams}}$	$N_{\text{Loop diagrams}}$
$q_u\bar{q}_u \to W^+W^-g$	$u\bar{u} \to W^+W^-g$	9	1361
	$c\bar{c} \to W^+W^-g$	9	1361
$q_d\bar{q}_d \to W^+W^-g$	$d\bar{d} \to W^+W^-g$	9	1361
	$s\bar{s} \to W^+W^-g$	9	1361
	$b\bar{b} \to W^+W^-g$	9	1361
$q_ug \to W^+W^-q_u$	$ug \to W^+W^-u$	9	1361
	$cg \to W^+W^-c$	9	1361
$q_dg \to W^+W^-q_d$	$dg \to W^+W^-d$	9	1361
	$sg \to W^+W^-s$	9	1361
	$bg \to W^+W^-b$	9	1361

Table 3.3: Number of Feynman diagrams of the partonic processes are generated by GRACE-Loop.

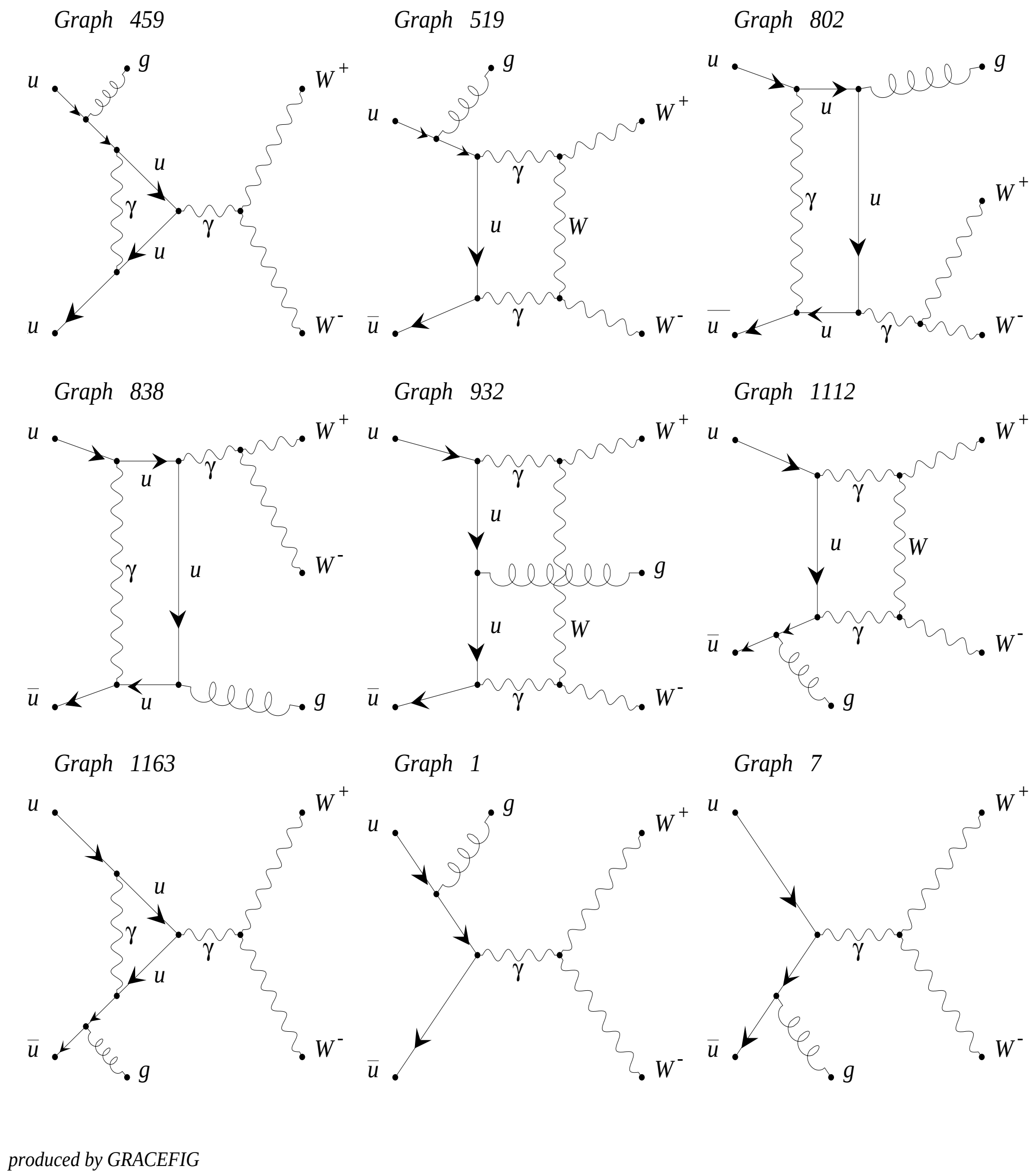

Figure 3.2: Selected Feynman diagrams are generated by the GRACE-Loop program.

3.3.2 Numerical checks

The calculation is verified numerically by consistency tests. In this subsection, the numerical checks for the process $u\bar{u} \to W^-W^+g$ are discussed as a typical example.

The results satisfy the Ward identities. For illustration one checks the identities numerically by taking a set of gauge invariant of diagrams which are described in figure 3.2. The polarization sum relation for gluon is given by

$$\mathcal{P}(\lambda) = \sum_{\lambda=0}^{3} \epsilon_\lambda^\mu(p)\epsilon_\lambda^\mu(p) \to -g^{\mu\nu} + \frac{n^\mu p^\nu + n^\nu p^\mu}{n \cdot p} - n^2 \frac{p^\mu p^\nu}{(n \cdot p)^2}, \tag{3.6}$$

where p^μ (ϵ_λ^μ) corresponds to 4-momentum (polarization vector) of gluon respectively and n is an axial vector. Once the polarization vector of gluon is replaced by its momentum, the amplitude of these diagrams must vanish. Subsequently, the results must be independent of the chosen gauge for the gluon. The numerical results of the tests are presented in Table 3.5. The first line in table 3.5 demonstrates that the result satisfies the Ward identity. The last two lines of Table 3.5 indicate that the results are in agreement over 19 digits in quadruple precision calculation with changing the gauge for the gluon. This test is performed at one arbitrary phase space point.

The partonic cross section of $u\bar{u} \to W^-W^+g$ is executed with different gauges for gluon. The cross section is evaluated by applying an energy cut of $E_g^{\text{cut}} \geq 10$ GeV and angle cut of $10° \leq \theta_g^{\text{cut}} \leq 170°$. The results are in excellent agreement among the different gauges for gluon. We choice the axial gauge vector as $n^\mu = (p^0, -\vec{p})$ for this test.

$\mathcal{P}(\lambda)$	$2\mathcal{R}(\mathcal{M}_{Tree}^{+}\mathcal{M}_{Loop})$
$-p^\mu p^\nu$	$\mathcal{O}(10^{-32})$
$-g^{\mu\nu}$	$-2.9088918728304840298524613165 02 \cdot 10^{-3}$
$-g^{\mu\nu} + \dfrac{p^\mu n^\nu + p^\nu n^\mu}{n \cdot p} - n^2 \dfrac{p^\mu p^\nu}{(n \cdot p)^2}$	$-2.908891872830484029246354625881 \cdot 10^{-3}$

Table 3.4: Result of the Ward-identities tests.

$\mathcal{P}(\lambda)$	$\hat{\sigma}_{2\mathcal{R}(\mathcal{M}^{+}_{Tree}\mathcal{M}_{Loop})}$ [pb]
$-g^{\mu\nu}$	-75.32350 ± 0.10658
$-g^{\mu\nu} + \dfrac{p^\mu n^\nu + p^\nu n^\mu}{n \cdot p} - n^2 \dfrac{p^\mu p^\nu}{(n \cdot p)^2}$	-75.32350 ± 0.10658

Table 3.5: Result of the Ward-identities tests in the partonic cross section.

The results are ultraviolet (UV), infrared finiteness (IR), and independent of the gauge parameters (NLG). In Tables (C.1, C.2, C.3) in Appendix C, the numerical results of the UV, NLG, IR are shown respectively at one random phase space point. This test is performed in quadruple precision. The results are stable over 19 digits in UV and NLG checks. For IR check, the results agree in 17 digits with 10^{-20} GeV $\leq \lambda \leq 10^{-17}$ GeV and over 20 digits when $\lambda \leq 10^{-20}$ GeV. The cause of the different precisions are due to the ways these parameters occur in the formulas. C_{UV} occurs only linearly as an extra term, the non-linear gauge parameters occur as products in terms that are by themselves typically much larger than the remaining terms. The infrared regulator λ will mainly contribute due to its appearance in the denominators (its appearance in the argument of logarithm function). As a result, the C_{UV} checks give much better accuracy than the other checks.

To complete numerical checks, one then considers the contribution of the hard photon bremsstrahlung. This part is the process $u\bar{u} \to W^-W^+g+\gamma$ with an additional photon $E_\gamma \geq k_c$. The process is generated by the tree level version of GRACE [20] with the use of the phase space integration by BASES. Table (C.4) in appendix C, the numerical results of the k_c stability check are shown. By changing the value of k_c from 10^{-3} GeV to 0.1 GeV, the results are in agreement to an accuracy which is better than 0.05% (the agreement is consistent with Monte Carlo integration accuracy).

The numerical checks will be repeated for all partonic processes. After verifying the numerical check, one sets the value of $\lambda = 10^{-17}$ GeV, $C_{UV} = 0$, $k_c = 10^{-3}$ GeV and $\tilde{\alpha} = \tilde{\beta} = \tilde{\delta} = \tilde{\kappa} = \tilde{\varepsilon} = 0$ for generating physical results of the calculation.

3.3.3 Physical results

The physical results of the calculations will be discussed in this subsection. As stated in the introduction section, full one-loop QCD corrections to these productions have been performed by several groups. **This thesis provides the full $\mathcal{O}(\alpha)$ electroweak corrections to these productions.** In general, the combination of QCD and electroweak corrections can be approximated [81] as

$$\sigma^{1-\text{loop}}_{QCD\oplus EW}(s) = K_{QCD} \cdot K_{EW} \cdot \sigma^{\text{LO}}_{QCD}(s), \tag{3.7}$$

where

$$K_{QCD/EW} = \frac{\sigma^{1-\text{loop}}_{QCD/EW}}{\sigma^{\text{LO}}_{QCD}}. \tag{3.8}$$

In the following we pay specially attention to discuss the physical results of full $\mathcal{O}(\alpha)$ electroweak corrections to the processes $pp \to W^-W^+$ and $pp \to W^-W^+ + 1\ jet$ at the 14-TeV LHC.

The process $pp \to W^-W^+$

The full one-loop electroweak corrections to W-pair production in association with a jet at the LHC have not been computed until this thesis. On the other hand, the full one-loop electroweak corrections to $pp \to W^-W^+$ at the LHC are available in Refs [77, 78, 79]. In order to check the performance of the GRACE-loop program as well as to gain the experience for the calculation of $pp \to W^-W^+ + 1$ jet, one starts the calculation for process $pp \to W^-W^+$. In order to cross-check our results with the one in paper [77], the same input parameters in Ref [77] are used. In particular, the input parameters are as follows:

$$\begin{aligned}
G_\mu &= 1.16637 \cdot 10^{-5}\ \text{GeV}^{-2}, \\
M_W &= 80.398\ \text{GeV}, && M_Z = 91.1876\ \text{GeV} \\
M_H &= 125\ \text{GeV}, && m_t = 173.4\ \text{GeV},
\end{aligned}$$

and using the value of M_W, M_Z and G_μ as above we then determine $\sin^2\theta_W$ and $\alpha_{e.m}(M_Z)$ as output. One obtains

$$\begin{aligned}\sin^2\theta_W &= 1 - M_W^2/M_Z^2 = 0.222646, \\ \alpha_{\rm e.m}(M_Z) &= \frac{\sqrt{2}G_\mu M_W^2 \sin^2\theta_W}{\pi} = \frac{1}{132.388}.\end{aligned} \tag{3.9}$$

The rapidity of the produced W bosons is defined as

$$Y_W = \frac{1}{2}\log\Big(\frac{E+p_z}{E-p_z}\Big), \tag{3.10}$$

where p_z is the component of the W boson momentum along the beam axis. The below results are presented with applying $|Y_W| \leq 2.5$ for the produced W bosons.

In consistence check with the paper [77], we use the PDF named MSTW2008 [82, 83, 84] and chose the factorization scale as

$$\mu_F = \frac{1}{2}\Big(\sqrt{M_W^2 + p_{T,W^-}^2} + \sqrt{M_W^2 + p_{T,W^+}^2}\Big)$$

Table 3.6 presents our results in comparison with the one in Ref [77]. By changing the value of $P_T^{\rm cut}$ of the W boson, the results in this work are in good agreement with the one in Ref [77].

$\sqrt{s} = 14$ TeV	$p_{T,W}^{\rm cut}$ [GeV]	$\sigma_{\rm Tree}^{G_\mu-\rm scheme}$ [pb]	$\delta_{EW}^{G_\mu-\rm scheme}$[%]
This work	100	5.377	-7.1
Ref [77]		5.379	-7.0
This work	250	$35.305 \cdot 10^{-2}$	-18.88
Ref [77]		$35.310 \cdot 10^{-2}$	-18.80
This work	500	$23.036 \cdot 10^{-3}$	-34.07
Ref [77]		$23.050 \cdot 10^{-3}$	-33.70

Table 3.6: Cross-check of the result in this calculation with the paper [77] by varying the $p_{T,W}^{\rm cut}$ of the W boson at 14 TeV of the LHC.

Table 3.7 shows our results with varying the invariant mass of W pair in comparison with the one in Ref [77]. We find a good agreement between this work and Ref [77].

$\sqrt{s} = 14$ TeV	$M^{\mathrm{cut}}_{W^-W^+}$ [GeV]	$\sigma^{G_\mu-\mathrm{scheme}}_{\mathrm{Tree}}$ [pb]	$\delta^{G_\mu-\mathrm{scheme}}_{EW}$ [%]
This work	200	28.81	−2.3
Ref [77]		28.84	−2.1
This work	300	9.495	−4.1
Ref [77]		9.492	−4.0
This work	500	1.841	−7.6
Ref [77]		1.841	−7.5

Table 3.7: Cross-check of the result in this calculation with the paper [77] by changing the invariant mass cut of the W-pair, ($M^{\mathrm{cut}}_{W^-W^+}$) at 14 TeV of the LHC.

The results also demonstrate that the electroweak corrections are of significant impact in the high P^{cut}_T of the W boson (or high invariant mass cut of W-pair). The corrections are of order 10% contributions and play an important role to study the new physics at the future LHC.

The process $pp \to W^-W^+ + 1$ *jet*

Now we turn our attention to the process $pp \to W^-W^+ + 1$ jet at the LHC. The input parameters for this calculation are presented in appendix C. In addition, cuts are applied to the jet as follows

$$P_{\mathrm{T,jet}} \geq 20 \text{ GeV}; \qquad |\eta_{\mathrm{jet}}| \leq 3. \tag{3.11}$$

Because the calculations are interested in the W boson properties, we apply a cut on the invariant mass of W boson and b-jet as $|M^{\mathrm{cut}}_{W^+,b-jet} - m_t| \geq 5$ GeV to reduce the background from single top production.

The pseudo-rapidity of the jet is given as

$$\eta_{jet} = -\log\left[\tan\left(\frac{\theta}{2}\right)\right], \tag{3.12}$$

where θ is the angle between the jet momentum $\mathbf{p}$ and the beam axis. The factorization scale is chosen as the invariant mass of the W-pair as

$$\mu_F^2 = \mu_R^2 = (P_{W^-} + P_{W^+})^2. \tag{3.13}$$

The strong coupling is thereof running from M_Z scale to μ_R by using the one-loop renormalization equation with $\alpha_s(M_Z) = 0.118$ or

$$\alpha_s(\mu_R^2) = \frac{\alpha_s(M_Z^2)}{1 + \beta_0 \log\left(\frac{\mu_R^2}{M_Z^2}\right)}. \tag{3.14}$$

The factor β_0 is given by

$$\beta_0 = \frac{11N_C - 2N_f}{12\pi}, \quad \text{with} \quad N_f = 5 \quad \text{and} \quad N_C = 3. \tag{3.15}$$

Table 3.8 shows the cross section and electroweak correction at the LHC 14 TeV of center-of-mass energy. The electroweak correction is -2.25% in α-scheme and -7.49% in G_μ-scheme.

In Figure 3.3, the differential cross section and electroweak corrections are presented as a function of transverse momentum of the jet, $P_{\mathrm{T,jet}}$. The distributions indicate clearly that electroweak corrections make significant contributions at high $P_{T,jet}$ region. The corrections range from -6% to -25% in α-scheme (and from -12% to -32% in corresponding to the G_μ-scheme) when varying $P_{\mathrm{T,jet}}$ from 50 GeV to 240 GeV. Its large contribution at high $P_{\mathrm{T,jet}}$ region is attributed to the enhancement of logarithm contributions, as remarked in section 3.2. In Figure 3.4, the cross section is presented as a function of the pseudo-rapidity of the jet. The electroweak corrections are of sizeable impact, order 10% in both schemes. Such corrections are very important to study the new physics signals in the future LHC experiments.

A short conclusion of this chapter: We find that the electroweak corrections to vector boson pair and boson pair in association with a jet at the LHC 14 TeV are

$\sqrt{s} = 14$ TeV	$\sigma_{\text{Tree}}^{G_\mu-\text{scheme}}$ [pb]	$\delta_{EW}^{\alpha-\text{scheme}}$ [%]	$\delta_{EW}^{G_\mu-\text{scheme}}$ [%]
$q\bar{q} \to W^-W^+g$	16.01	-3.53	-8.63
$qg \to W^-W^+q$	33.29	5.14	-0.06
$pp \to W^-W^+ + 1\text{jet}$	49.30	-2.25	-7.49

Table 3.8: The cross section and electroweak corrections are shown for the LHC 14 TeV.

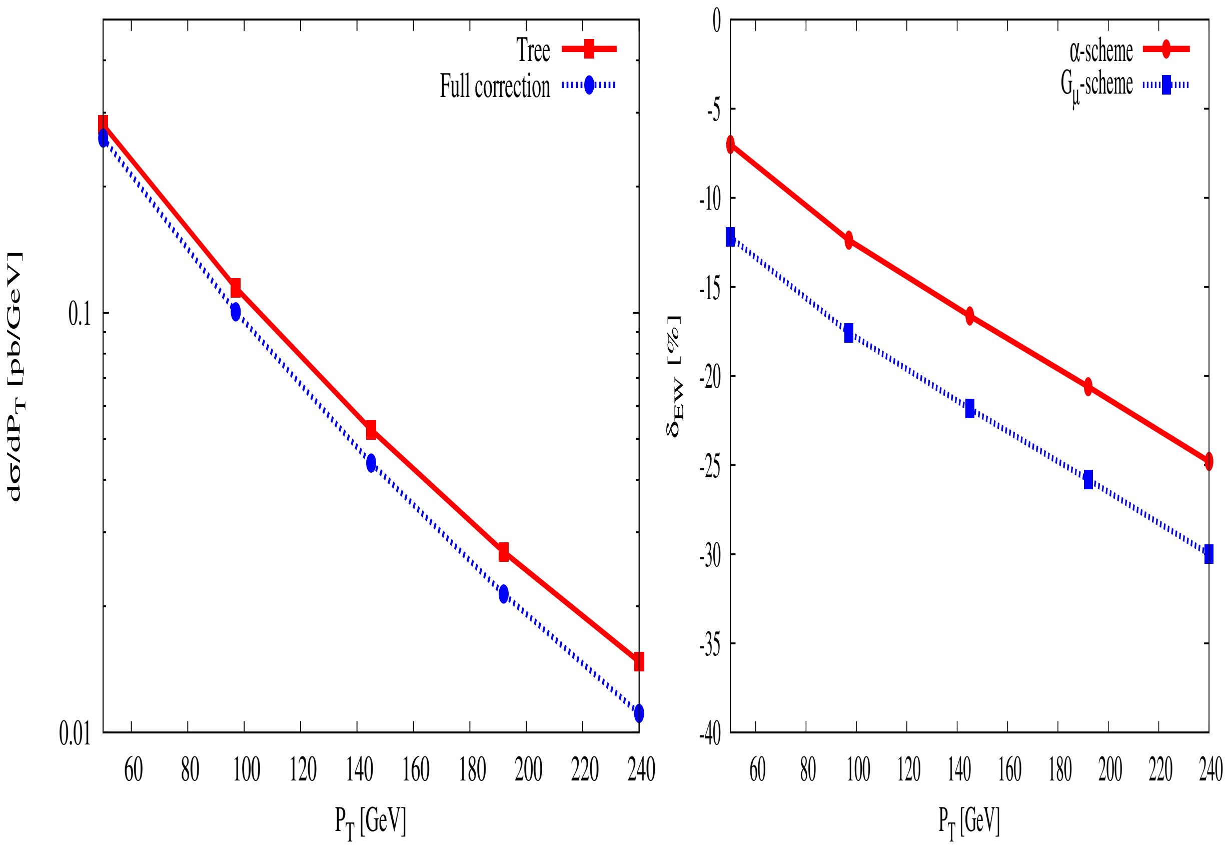

Figure 3.3: Distributions of cross-section (left) and full electroweak corrections (right) are presented as a function of $P_{\text{T,jet}}$.

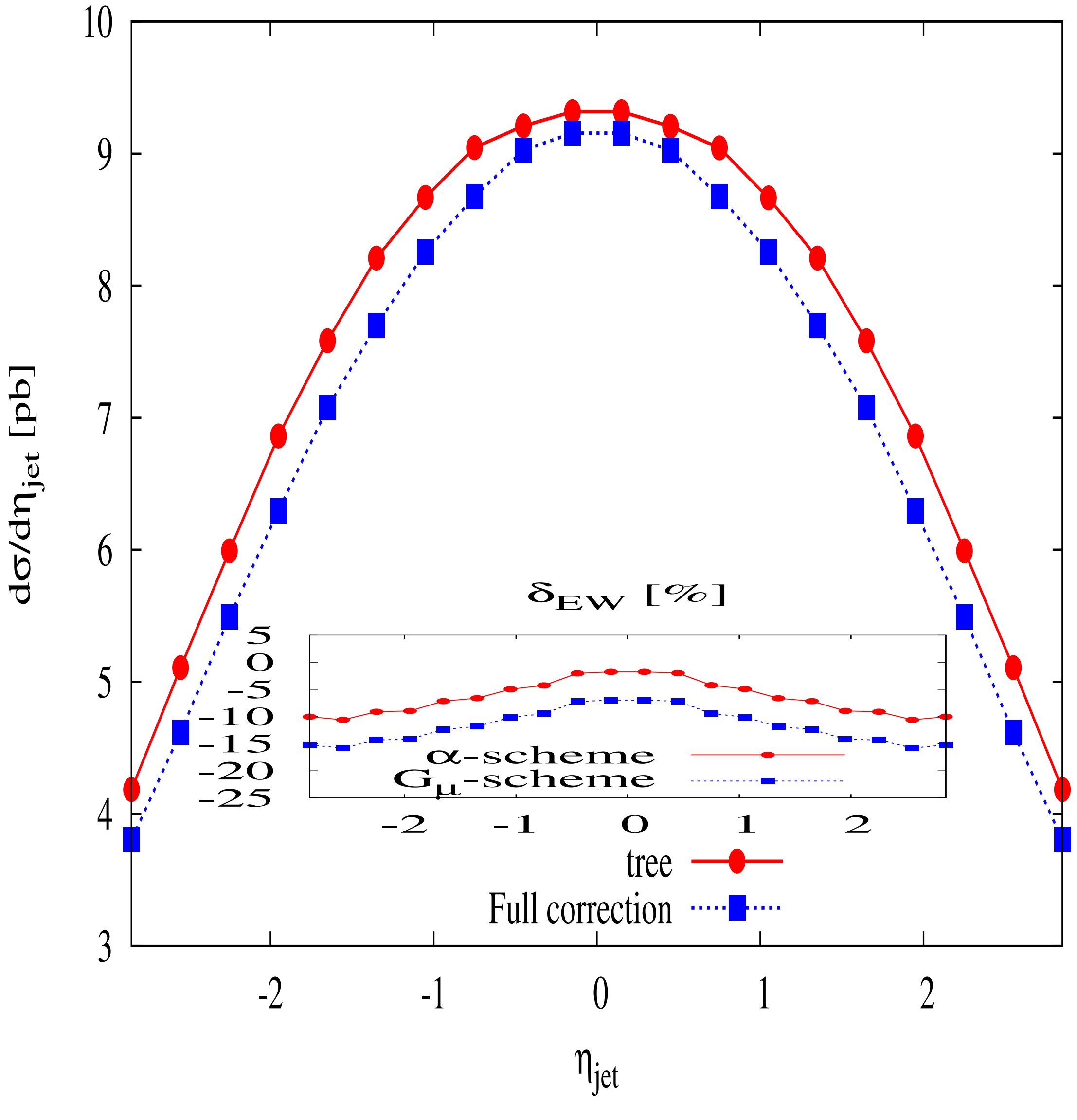

Figure 3.4: Distribution of cross-section is presented as a function of the pseudo-rapidity of the jet.

of significant impact (order 10%) at high P_{T} region where the new physics signatures are expected. Such corrections provide an important information to study the new physics signals at the LHC.

Chapter 4

Full $\mathcal{O}(\alpha)$ electroweak radiative corrections to $e^+e^- \to e^+e^-\gamma$ at the ILC

In this chapter, we present a calculation of the full $\mathcal{O}(\alpha)$ electroweak radiative corrections to the process $e^+e^- \to e^+e^-\gamma$ at the International Linear Collider. One then investigates the impact of electroweak corrections to total cross section and the relevant distributions: the differential cross section as a function of the invariant masses, energies as well as angles of final particles.

4.1 Luminosity measurement at ILC

The International Linear Collider is a high-luminosity linear electron-positron collider based on superconducting accelerating cavities [85]. The center-of-mass-energy of the ILC ranges from 200 to 500 GeV (it can be extendable up to 1 TeV).

It is widely accepted from the high energy physics community that the main goals of the ILC program [85] are:

- precise measurements of the Higgs boson properties such as: Higgs mass, spin, and interaction strengths of Higgs boson;
- precise measurements of the interactions of top quark, gauge bosons;
- searches for physics Beyond the Standard Theory.

The measurements will be performed with high precision in which the expected statistical error is typically below 0.1% at the ILC. The precision will be achieved by requiring a very precise measurement of the luminosity.

At the ILC, the integrated luminosity is measured [86] by counting Bhabha events and comparing it with the corresponding theoretical cross section:

$$\int dt\, \mathcal{L} = \frac{N_{\text{events}} - N_{\text{bgk}}}{\epsilon\ \cdot \sigma_{\text{theory}}}. \tag{4.1}$$

In this formula $N_{\text{events}}(N_{\text{bgk}})$ is the number of the observed Bhabha events (the estimated background events). σ_{theory} is the Bhabha scattering cross section which is calculated from the perturbation theory. ϵ is the total selection efficiency for the events and $\int dt\, \mathcal{L}$ is the integrated luminosity.

It is clear that the precise calculations of Bhabha scattering play an important role for high precision of luminosity measurement. Thus the one-loop electroweak corrections to Bhabha scattering are of great interest by many authors. The full one-loop electroweak corrections to the $e^+e^- \to e^+e^-$ reaction were calculated in Refs [87, 88] and in Refs [89, 90] for many years ago. These calculations were performed independently in Refs [91, 92]. From these reports, one finds that the electroweak corrections are significant contribution to total cross section, about $\mathcal{O}(10\%)$ at high energy.

With high precision at the ILC, two-loop electroweak corrections to Bhabha scattering must be taken into consideration. Such calculations were also of great concern by many authors for many years. However, the calculations have only been performed mostly at the level of two-loop QED corrections. A full two-loop electroweak corrections are by far under development. In this thesis, several typical papers for two-loop QED calculations are referred. Two-loop photonic corrections to Bhabha scattering were completed in Refs [93, 94]. Other calculations which kept the electron mass in the squared amplitude were also done in Ref [95]. In a later publication, the same authors included the soft photon emission's contribution to differential cross-section, as presented in Ref [96]. In addition, two-loop QED corrections to Bhabha cross-section involving the vacuum polarization by heavy fermions of arbitrary mass were also considered and presented in Refs [97, 98]. Moreover, an approximated calculation of two-loop electroweak corrections to Bhabha scattering were computed in Ref [99]. In this calculation, the authors proposed the dominant logarithmically enhanced two-loop electroweak corrections to the differential cross section in the high energy limit at large scattering angles.

The perspectives of the calculation are as follows. First, one-loop electroweak radiative corrections to the process $e^+e^- \to e^+e^-\gamma$ with soft bremsstrahlung photon, are necessary for calculating the two-loop electroweak corrections to Bhabha scattering. The process is employed to cancel against the infrared divergence appeared in two-loop calculation. Secondly, in order to correct the Bhabha events, the evaluation of its background is also important for the luminosity measurement. Experiment may misidentify $e^+e^-\gamma$ as e^+e^- events for following reasons: (i) the photon has a small opening angle to the final electron (positron); (ii) the photon is emitted in parallel direction to the beam axis. With these misidentifications, the process $e^+e^- \to e^+e^-\gamma$ is one of the channels that forms a significant contribution to the background of Bhabha events. Thus, precise calculation of this process has to be concerned. Last but by no means least, the process will become a good candidate for luminosity measurements if the theoretical calculation is well-controlled.

For the above reasons, the precise calculation to this process is proposed. Noted that the lowest-order calculation to this process was obtained in Ref [100]. Moreover, one-loop QED corrections to hard-bremsstrahlung process $e^+e^- \to e^+e^-\gamma$ can be found in Ref [101]. An analytical calculation of one-loop QED corrections to the process $e^+e^- \to e^+e^-\gamma$ is also considered in Ref [102].

In this chapter, full $\mathcal{O}(\alpha)$ electroweak radiative corrections to this process are reported. In the physical results, one examines the electroweak corrections to the total cross-section and its relevant distributions: the differential cross sections as a function of the invariant masses, energies as well as angles of final particles.

4.2 The process $e^+e^- \to e^+e^-\gamma$ at the ILC

The main calculation and the physical results of this process are presented in this section.

4.2.1 The calculation

The full set of Feynman diagrams with the non-linear gauge fixing as described in several previous chapters consists of 32 tree diagrams and 3456 one-loop diagrams including the counterterm diagrams. In Fig 4.1 some selected diagrams are shown.

For this calculation, we apply an axial gauge for external photon by using the polarization sum of photon as follows

$$\mathcal{P}(\lambda) = \sum_{\lambda=0}^{3} \epsilon_\lambda^\mu(p)\epsilon_\lambda^\mu(p) = -g^{\mu\nu} + \frac{n^\mu p^\nu + n^\nu p^\mu}{n \cdot p} - n^2 \frac{p^\mu p^\nu}{(n \cdot p)^2}, \tag{4.2}$$

where p^μ (ϵ_λ^μ) corresponds to 4−momentum (polarization vector) of external photon respectively. n is an axial vector which takes the form

$$n = (p^0, -\vec{p}). \tag{4.3}$$

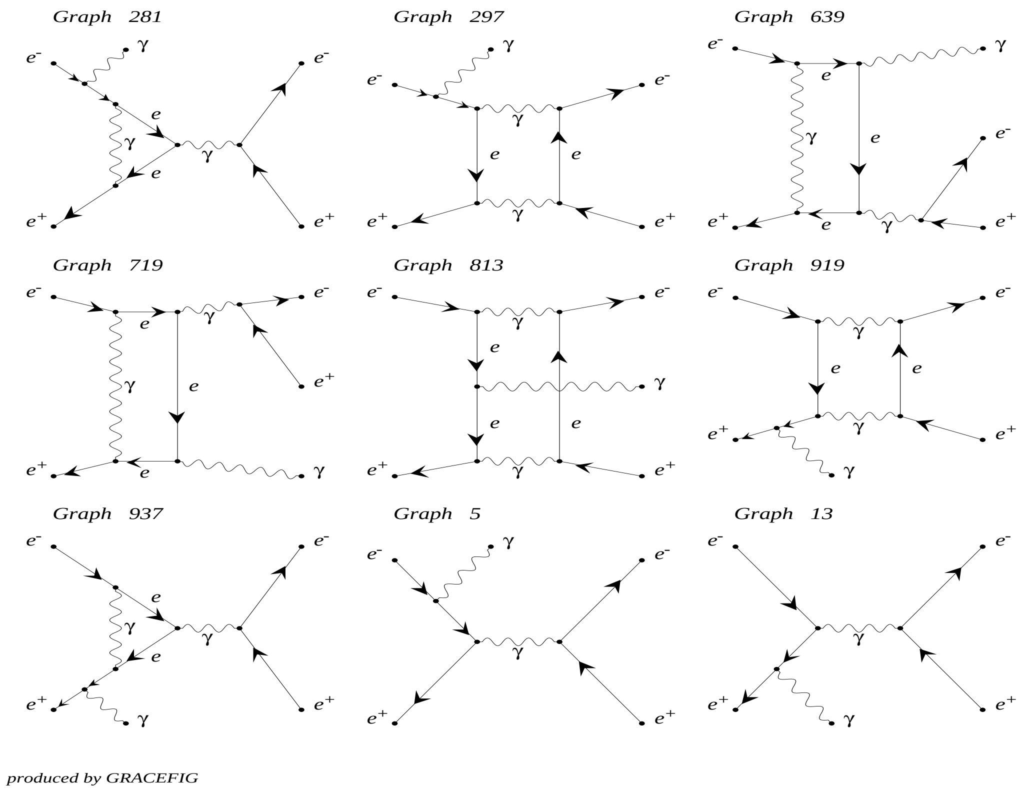

Figure 4.1: Selected Feynman diagrams are generated by the GRACE-Loop program.

with this choice, the third term in formula (4.2) vanishes. That is light-cone gauge of photon.

As stated in chapter 2, there are two advantages for the axial gauge for external photon. The first advantage is to cure the problem with large numerical cancellations. This is very useful when calculating the processes with the light particles in the final states and with applying a small angle as well as energy cuts for these particles. For example, the total squared amplitude of the diagrams 5 and 13 in figure 4.1 is investigated. In table 4.1, the numerical results of the amplitude of these diagrams at a phase space point (it is chosen in the small opening angle of photon and electron region) are shown. The first column shows results corresponding to $\mathcal{P}(\lambda) \to -g^{\mu\nu}$ case. It is called the non-axial gauge for external photon later. One finds the large numerical cancellation problem appeared in this case. It is resolved when using the axial gauge for photon, as indicated in the second column.

Amplitude	non-axial gauge	axial gauge
$\mathcal{M}_5^2 + \mathcal{M}_{13}^2$	$0.1116212357 \cdot 10^{13}$	$0.3644158264 \cdot 10^{2}$
$2\mathcal{M}_5^*\mathcal{M}_{13}$	$-0.1116212356 \cdot 10^{13}$	$0.1546482734 \cdot 10^{3}$
$\lvert\mathcal{M}_5 + \mathcal{M}_{13}\rvert^2$	$0.1910871582 \cdot 10^{3}$	$0.1910898560 \cdot 10^{3}$

Table 4.1: The problem with large numerical cancellation.

The second advantage is to provide a useful tool to check the consistency of the results. Because of the Ward identities, the results must be independent of the choice of the gauge. We will discuss this point in further detail in the next subsection.

4.2.2 Numerical check

The calculation is checked numerically by consistency tests. The results satisfy the Ward identities. For illustration, the identities are verified numerically by taking the gauge invariant diagrams described in Figure 4.1. The numerical results are presented in table 4.2. Because of the large numerical cancellation problem, the results only agree to 18 digits between different gauges for photon when quadruple precision is used. Therefore, the axial gauge for external photon is employed for generating the physical results later.

$\mathcal{P}(\lambda)$	$2\mathcal{R}(\mathcal{M}^+_{Tree}\mathcal{M}_{Loop})$
$-p^\mu p^\nu$	$\mathcal{O}(10^{-34})$
$-g^{\mu\nu}$	$-0.151855791025554810790201559163474$
$-g^{\mu\nu} + \dfrac{p^\mu n^\nu + p^\nu n^\mu}{n.p}$	$-0.151855791025554810828810542464352$

Table 4.2: The result must be independent of the choice of gauge for photon.

Together with check of Ward identities, the results must also have ultraviolet and infrared finiteness, and independence of the gauge parameters. In tables (C.5, C.6, C.7) in appendix C, the numerical results of the ultraviolet finiteness checks, the gauge invariance and the infrared finiteness at one random phase space point, are presented. This test is performed in quadruple precision. The numerical results are stable over 20 digits in UV and NLG checks. For IR check, the results are in agreement in 17 digits with 10^{-20} GeV $\leq \lambda \leq 10^{-17}$ GeV and in 20 digits when $\lambda \leq 10^{-20}$ GeV.

Furthermore the contribution of the hard photon bremsstrahlung is considered. This part is the process $e^+e^- \to e^-e^+\gamma(\gamma)$ with an additional photon $E_\gamma \geq k_c$. By including this contribution to the total cross section, the final results have to be independent of k_c. Table (C.8) in appendix C, the numerical result of the k_c stability check is shown. By changing the value of k_c from 10^{-3} GeV to 0.1 GeV, the results are in agreement to an accuracy which is better than 0.05% (this agreement is consistent with the Monte Carlo accuracy). For the k_c stability checks, it is important to note that we have two photons at the final state. One of them is the hard photon which will be applied an energy cut of $E_\gamma^{\mathrm{cut}} \geq 10$ GeV and an angle cut of $10^\circ \leq \theta_\gamma^{\mathrm{cut}} \leq 170^\circ$. The other one is a real photon radiation of which the energy is greater than k_c and smaller than the first photon's energy.

After checking the results successfully, we can proceed with the computations of the physical results of the process. We set $\lambda = 10^{-17}$ GeV, $C_{UV} = 0$, $k_c = 10^{-3}$ GeV and $\tilde{\alpha} = \tilde{\beta} = \tilde{\delta} = \tilde{\kappa} = \tilde{\varepsilon} = 0$. In order to reduce the calculation time, we neglect the diagrams which contain the coupling of Higgs boson to electron and positron in the integration step, because their contributions are negligible.

4.2.3 The physical results

The input parameters for this calculation are presented in appendix B. Moreover the decay width of the Z boson will be taken to be 2.35 GeV which is calculated by using the tree version of GRACE [20] with the same input parameters. All the decay channels of the Z boson within the Standard Model are taken into account to generate this value. One then use this for the propagators of the Z boson exchange. It helps to avoid the singularity due to the Z boson resonance.

In the physical discussion, this thesis only focus on the case in which the process is considered as a candidate for luminosity measurements. For this reason, full $\mathcal{O}(\alpha)$ electroweak corrections to $e^-e^+ \to e^-e^+\gamma$ are evaluated by applying the follow cuts. For final particles, one applies an energy cut of $E^{\rm cut} \geq 10$ GeV and an angle cut of $10^\circ \leq \theta^{\rm cut} \leq 170^\circ$ with respect to the beam axis. In addition, to isolate the photon from the electron (positron) we apply an opening angle cut between the photon and the $e^-(e^+)$ of 10°. Finally, to distinguish $e^-e^+\gamma$ events from $\gamma\gamma$ events, an angle cut between the final state electron and positron of 10° is applied.

The total cross section and electroweak corrections

In fig 4.2, the cross section and the electroweak corrections are shown as a function of $\sqrt{s}$. The center-of-mass energy ranges from 250 GeV (which is near the threshold of $M_H + M_Z$) to 1 TeV. The cross section decreases more and more with increasing center-of-mass energy. In the bottom part of figure 4.2, the electroweak corrections are presented. The electroweak corrections are from -4% to $\sim -21\%$ when varying $\sqrt{s}$ from 250 GeV to 1 TeV. Fig 4.2 clearly indicates that QED corrections make dominant contribution in comparison with the weak corrections. It goes to -14% at $\sqrt{s} = 1$ TeV, while the weak corrections change from $\sim 0.5\%$ to $\sim 6\%$. The weak corrections are also expressed in G_μ-scheme. In the energy range of 250 GeV to 1 TeV, the weak corrections in G_μ-scheme change from around -5.5% to around -11%. It is clear that the corrections make significant contribution to the total cross section and cannot be ignored for the high precision program at the ILC.

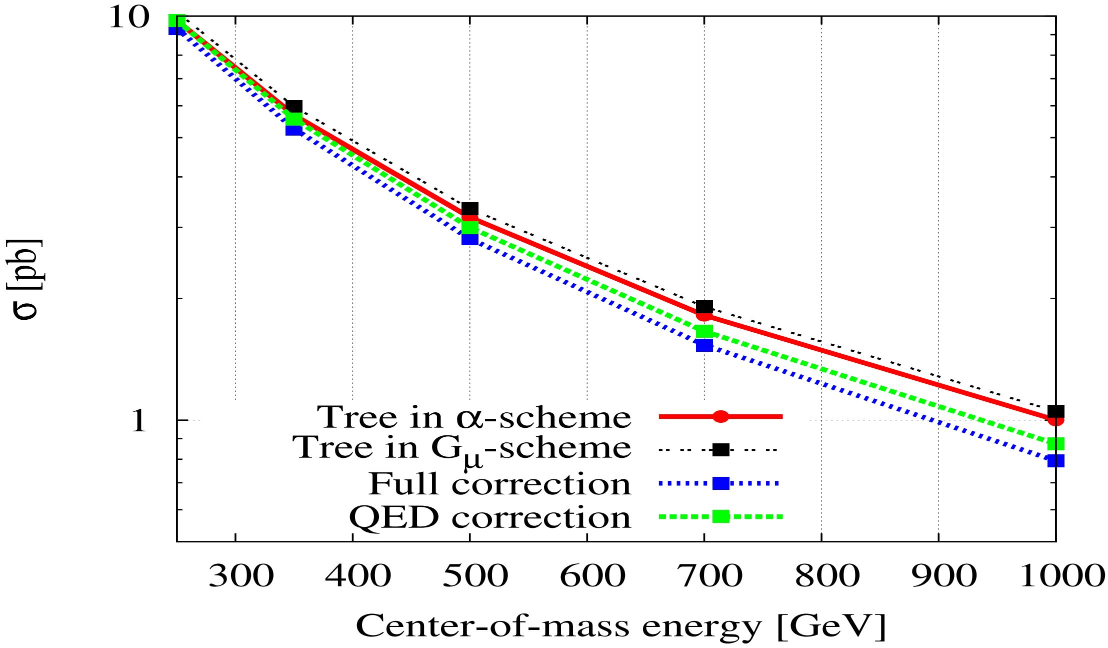

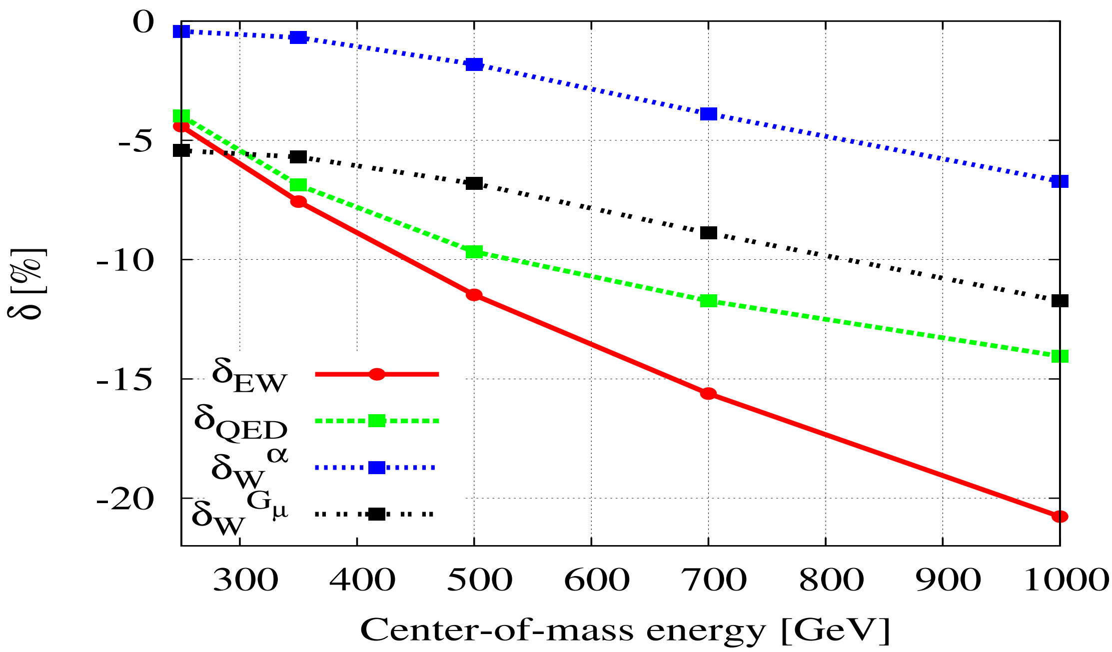

Figure 4.2: In this figure, the cross-section (upper) and full electroweak corrections (right) are presented as a function of the center-of-mass energy.

Relevant distributions

We now generate relevant distributions that are the differential cross sections as a function of invariant mass, energies, and angles of final particles. In these distributions, the red line is the result of the tree level calculation and the blue points with error-bar are the result of including the full radiative corrections. The left (right) figures show the given distributions at $\sqrt{s} = 250$ GeV (1 TeV) respectively. The K_{EW} factor is also shown below these distributions to present the electroweak corrections to the differential cross sections. The K_{EW} factor is defined as the ratio of the cross section from full one-loop radiative corrections to the cross section from tree-level.

Figure 4.3 presents the cross-section distributions as a function of the photon energy for $\sqrt{s} = 250$ GeV and $\sqrt{s} = 1$ TeV. Overall, the cross section decreases with increasing photon energy. At $\sqrt{s} = 250$ GeV, two peaks appear, one at $E_\gamma = \dfrac{s - M_Z^2}{2\sqrt{s}}$ and one at $\dfrac{\sqrt{s}}{2}$. The first peak corresponds to the photon energy recoiling against an on-shell Z boson, and the right peak corresponds to the photon energy recoiling against a virtual photon that creates a small-mass electron-positron pair. Due to the high energy the peaks overlap within our resolution at $\sqrt{s} = 1$ TeV. The distributions also indicate clearly that the radiative corrections make a sizeable impact and are important for the luminosity monitor at the ILC.

Figure 4.4 presents the differential cross sections as a function of positron energy for $\sqrt{s} = 250$ GeV and $\sqrt{s} = 1$ TeV. The cross section increases with increasing positron energy. Two peaks appear in the distributions; the first of which is attributed to the highest-energy positron $E_{e^+} \sim \dfrac{\sqrt{s}}{2}$ (or the smallest invariant mass of the photon and electron). The second peak corresponds to a minimum-energy photon emitted from the electron. This peak appears at $E_{e^+} \sim \dfrac{\sqrt{s}}{2} - E_\gamma^{\min}$. Within our resolution at $\sqrt{s} = 1$ TeV, the two peaks overlap. Again, the radiative corrections make a significant impact.

In figure 4.5 the differential cross sections are a function of the invariant mass of

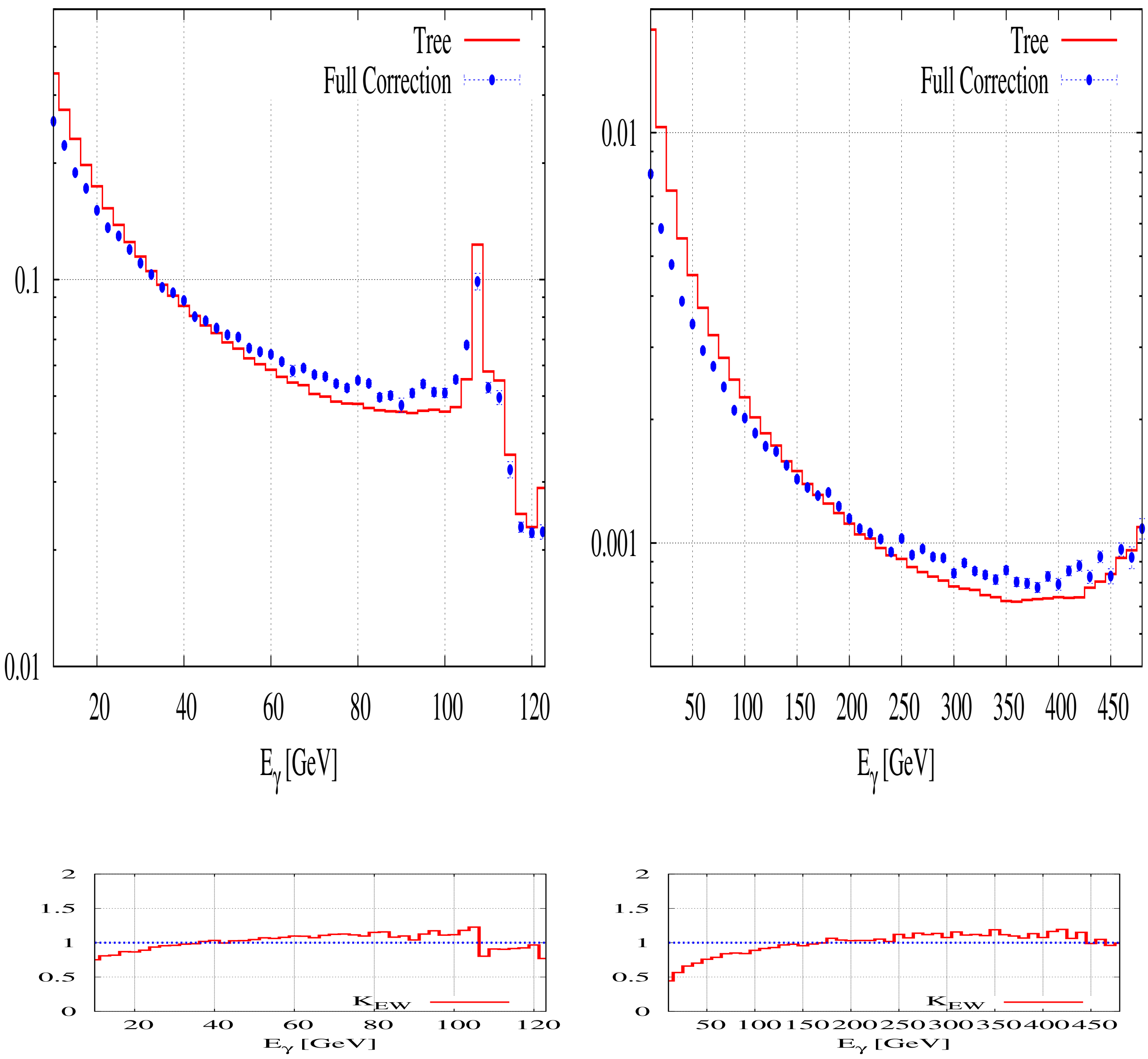

Figure 4.3: The differential cross-sections as a function of the photon energy at $\sqrt{s}$ = 250 GeV (left) and $\sqrt{s}$ = 1 TeV (right). The bottom figures are the K_{EW} factor which is a function of photon energy.

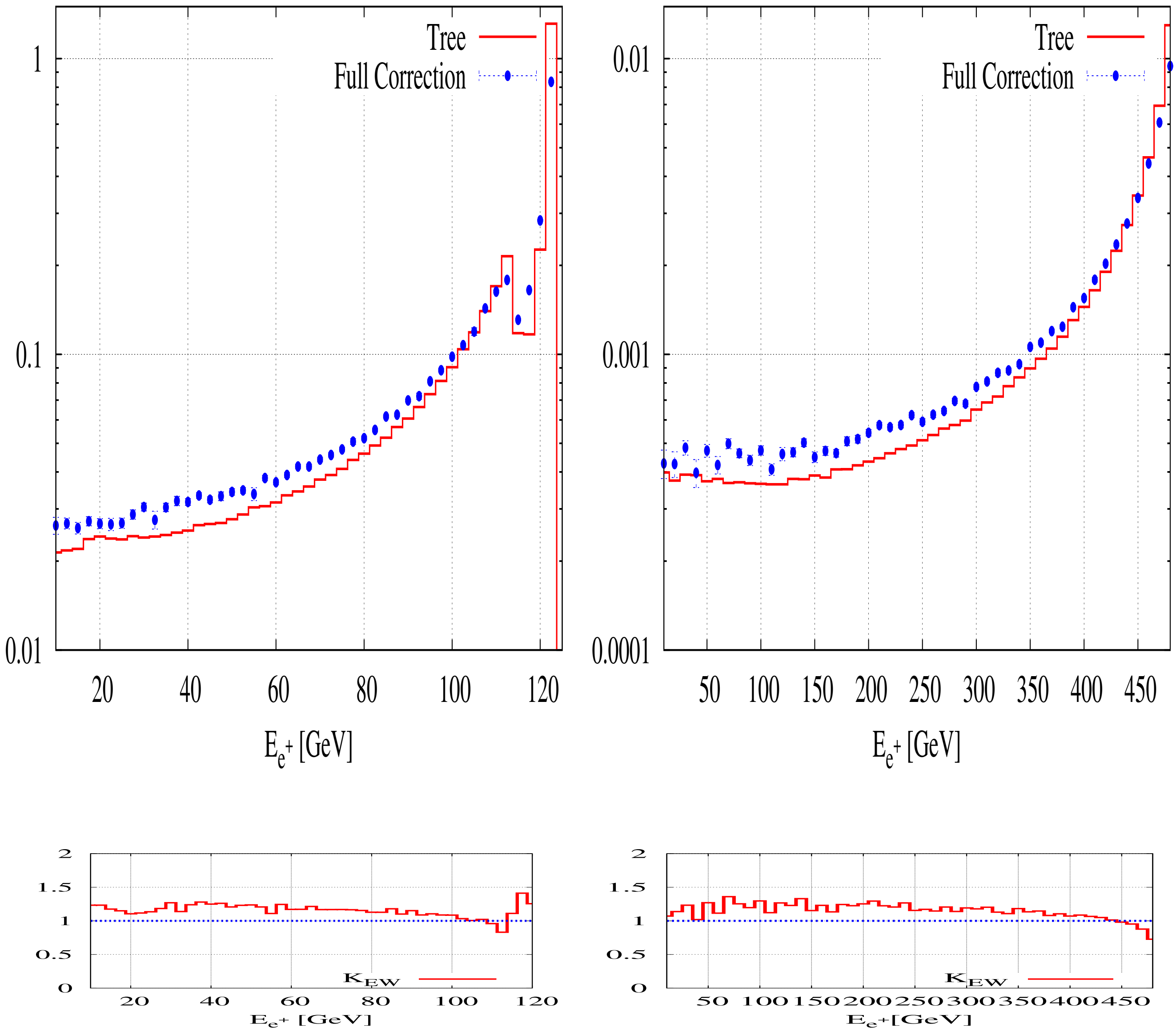

Figure 4.4: The differential cross-sections as a function of the positron's energy. At $\sqrt{s} = 250$ GeV (left) and at $\sqrt{s} = 1$ TeV (right). The bottom figures present for the K_{EW} factor.

the e^-, e^+ pair at $\sqrt{s} = 250$ GeV and $\sqrt{s} = 1$ TeV. We observe the peaks at the M_Z pole and at the high mass region (corresponding to the radiative tail or the virtual photon mass pole). Again, the radiative corrections are clearly observed.

The differential cross section as a function of invariant mass of the e^- and photon ($m_{\gamma e^-}$) are discussed in figure 4.6 at $\sqrt{s} = 250$ GeV and $\sqrt{s} = 1$ TeV. The cross section decreases with increasing $m_{\gamma e^-}$. Two peaks appear in the distributions, which are attributed as for the case of the positron energy distributions. It can be observed that the radiative corrections form a significant contribution at the peaks of the distributions. The corrections provide an important information to distinguish $e^-e^+\gamma$ from e^-e^+ events.

In fig 4.7, the angular distributions of photon are shown at $\sqrt{s} = 250$ GeV and $\sqrt{s} = 1$ TeV. One finds a symmetric shape of the cross-section with respect to $\cos\theta_\gamma$. At $\sqrt{s} = 1$ TeV, the radiative corrections are more visible in comparison with the one at 250 GeV of center-of-mass energy.

The angular distributions of positron in final states are shown at $\sqrt{s} = 250$ GeV and $\sqrt{s} = 1$ TeV in fig 4.8. At $\sqrt{s} = 1$ TeV, the radiative corrections are more effective than the one at 250 GeV of center-of-mass energy.

In figure 4.9, the differential cross-sections as a function of the cosine of opening angle between photon and electron in the final states, are presented. The left figure is at $\sqrt{s} = 250$ GeV and the right figure is at $\sqrt{s} = 1$ TeV. Again one observes more visible corrections at 1 TeV than at 250 GeV. This corrections provide useful information to distinguish $e^-e^+\gamma$ from e^-e^+ events at the ILC.

A short conclusion of this chapter: The physical results of the calculation indicates that the electroweak corrections are of significant contribution. It varies from $\sim -4\%$ to $\sim -21\%$ for the center-of-mass energy ranging from 250 GeV to 1 TeV. The corrections also make a sizeable impact to the differential cross section. Therefore, this calculation is important for determining the luminosity at the ILC. In future work, we consider the process with soft bremsstrahlung photon aiming at the

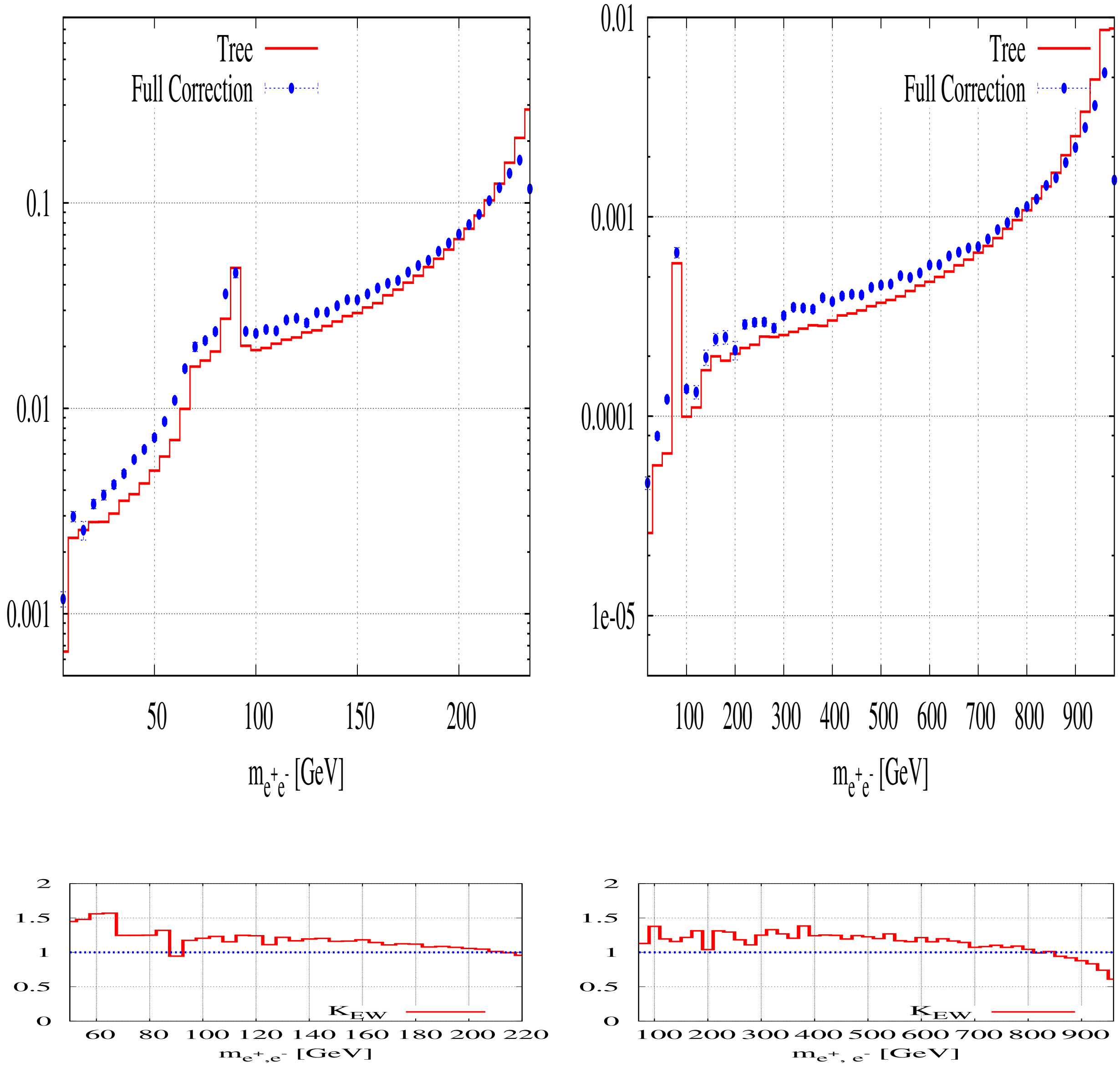

Figure 4.5: The differential cross sections are a function of the invariant mass of the e^-, e^+ pair. The left figure is at $\sqrt{s} = 250$ GeV and the right figure is at $\sqrt{s} = 1$ TeV.

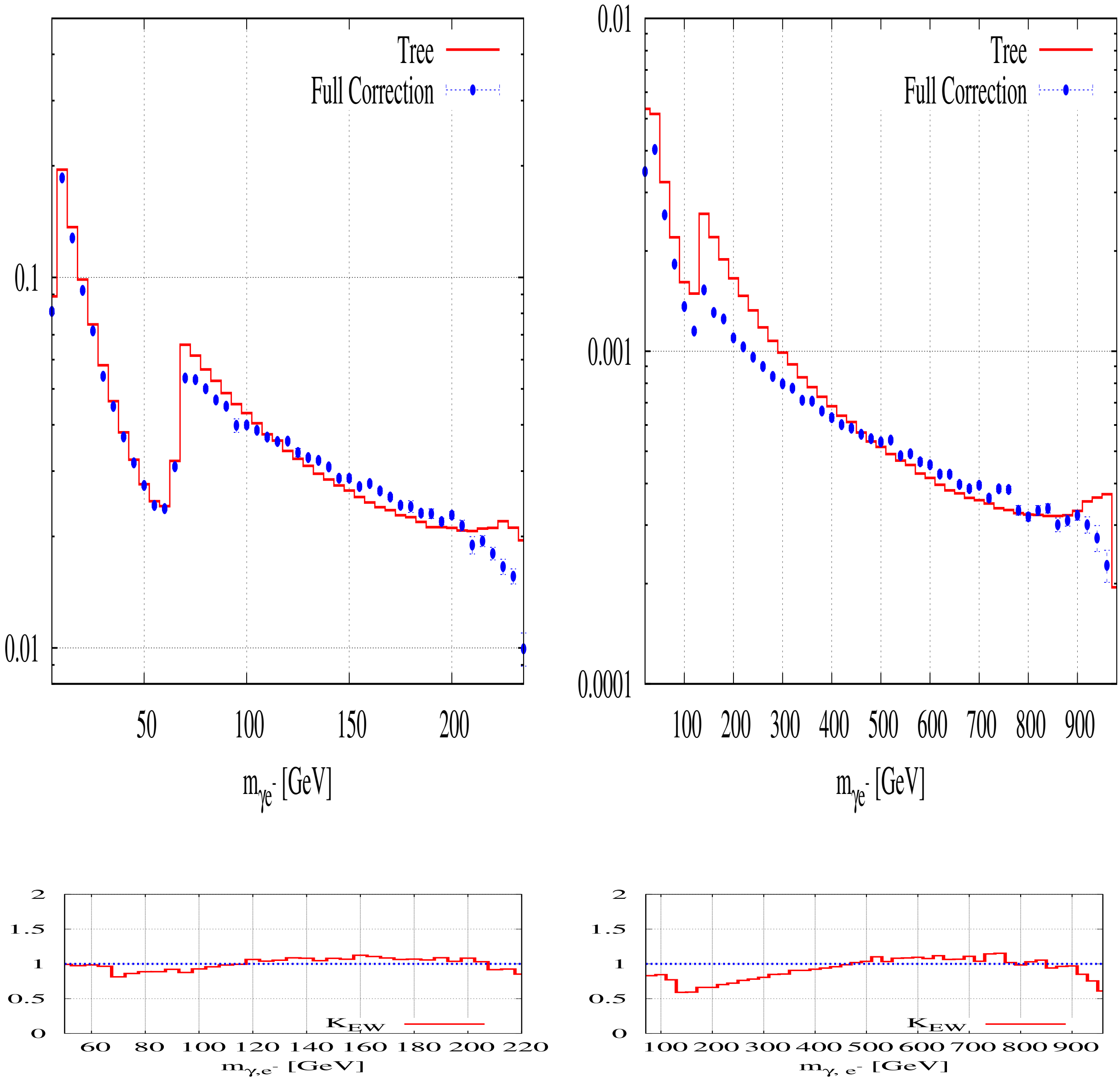

Figure 4.6: The differential cross-sections as a function of the invariant mass of the e^-, photon. The left figure is at $\sqrt{s} = 250$ GeV and the right figure at $\sqrt{s} = 1$ TeV.

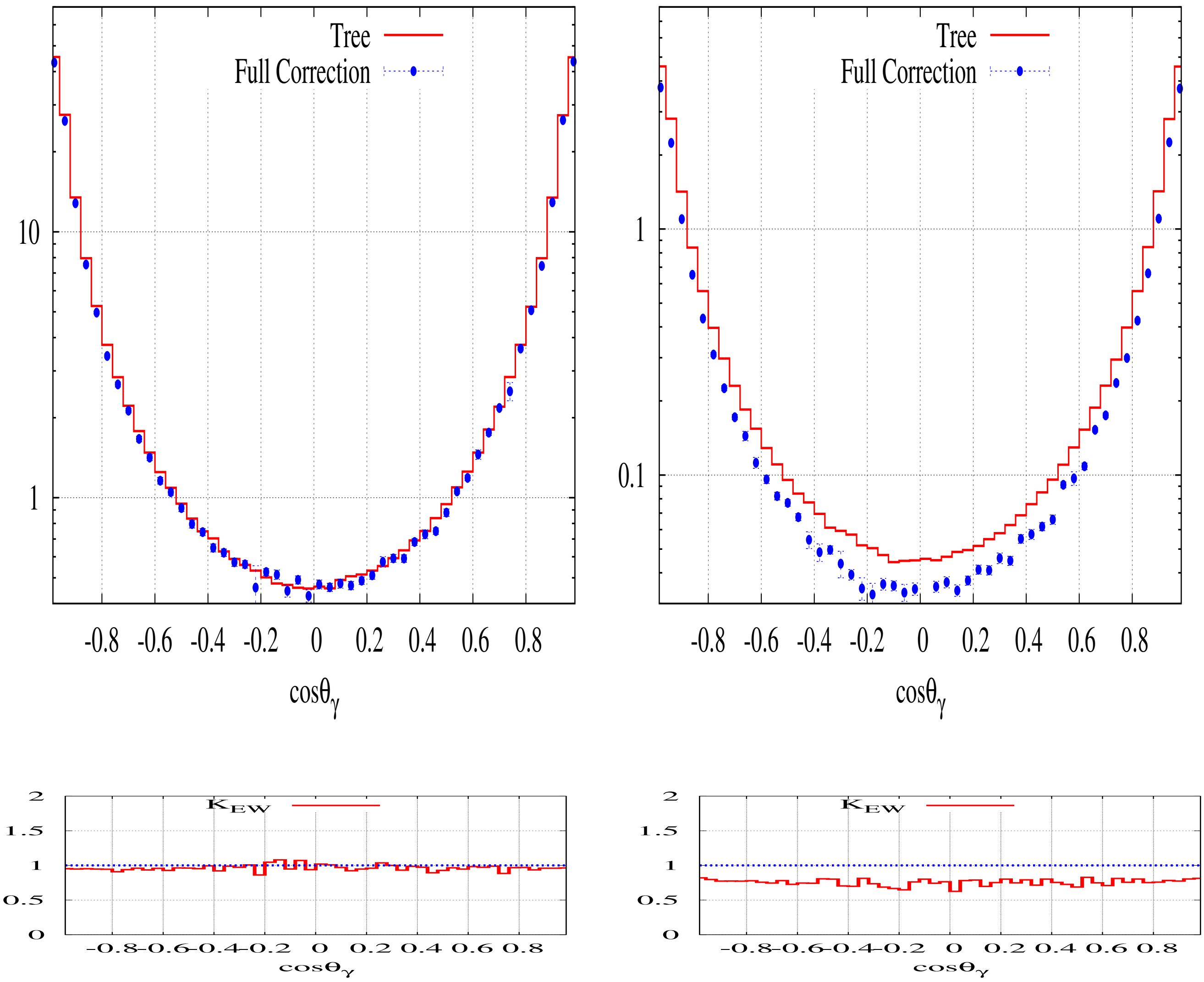

Figure 4.7: The angular distributions of photon are shown at $\sqrt{s}$ = 250 GeV and $\sqrt{s} = 1$ TeV.

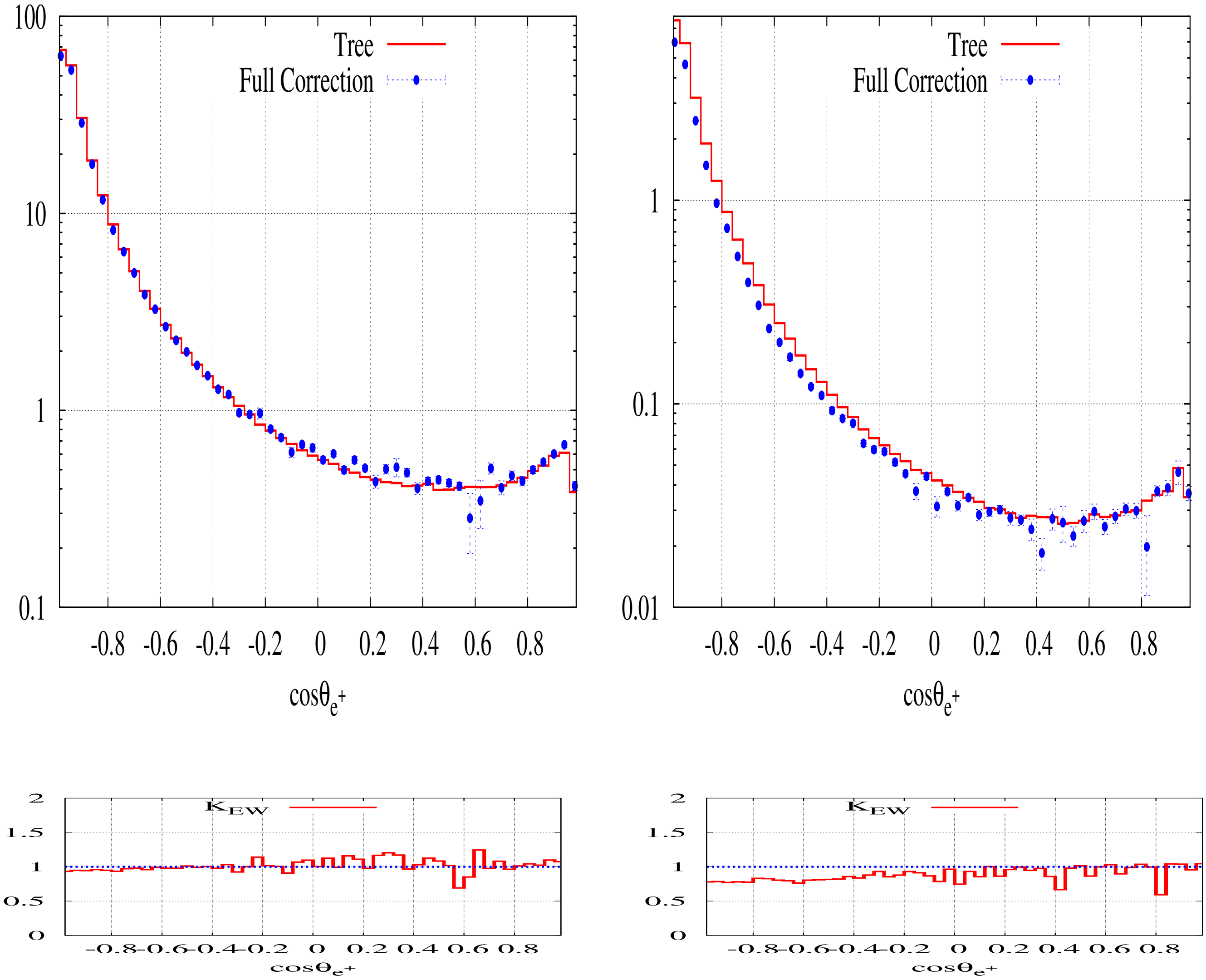

Figure 4.8: The angular distributions of positron in final states are shown at $\sqrt{s} = 250$ GeV and $\sqrt{s} = 1$ TeV.

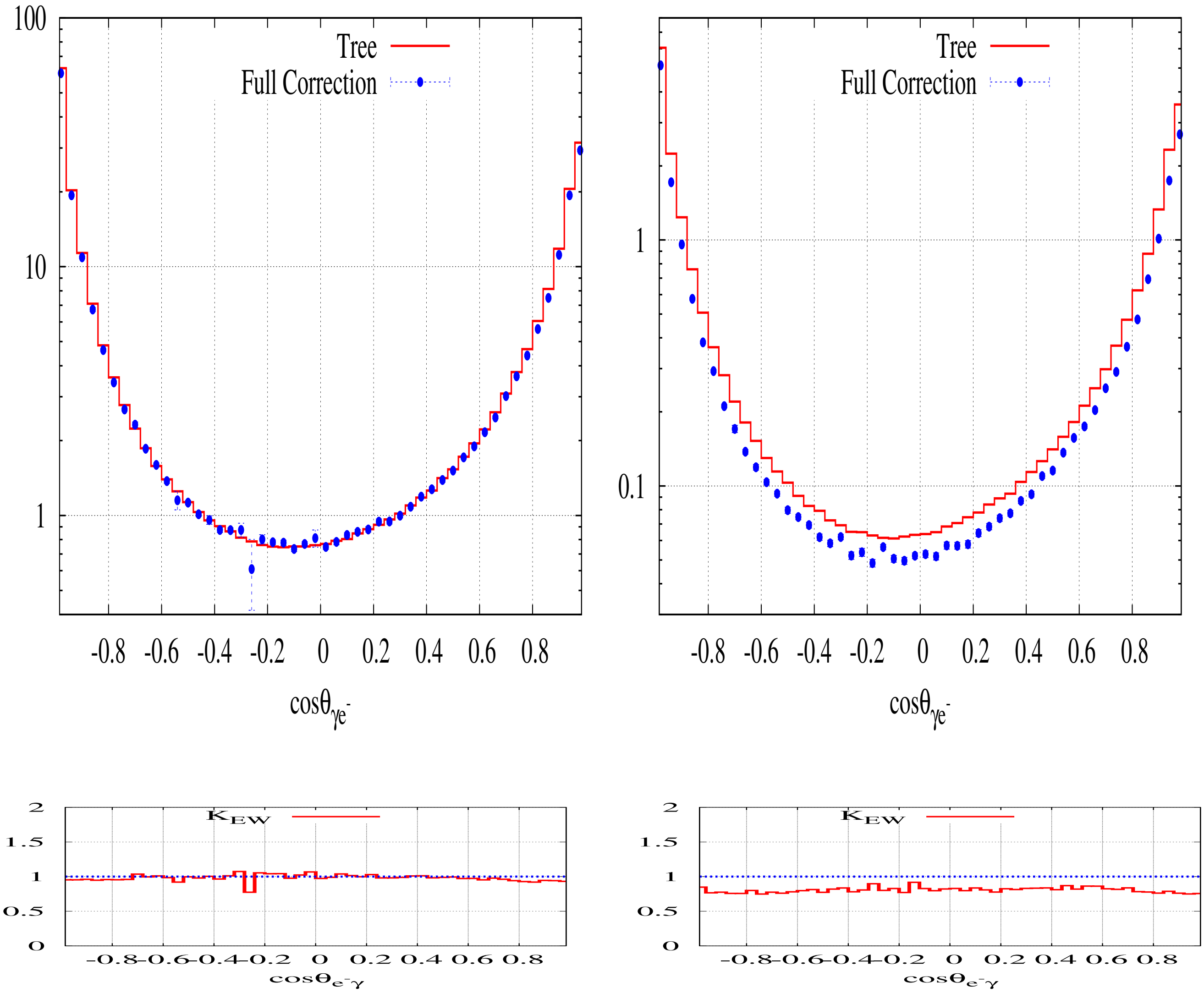

Figure 4.9: The angular distributions of opening angle between photon and electron in the final states. The left figure is at $\sqrt{s}$ = 250 GeV and the right figure is at $\sqrt{s} = 1$ TeV.

calculation for full two-loop corrections to Bhabha scattering.

Chapter 5

Full $\mathcal{O}(\alpha)$ electroweak radiative corrections to the processes $e^+e^- \to t\bar{t}$ and $e^+e^- \to t\bar{t}\gamma$ at the ILC

Top quark is the heaviest elementary particle in the Standard Model theory. Thank to its large mass, top quark most strongly couples to the Higgs boson. Moreover, the top quark mass is one of the fundamental parameters of the Standard theory. It plays a key role in the global SM fit of electroweak precision data. Therefore the precise measurements of top quark properties are one of the most important goals at future colliders. The measurements provide useful information to understand the EWSB as well as to open a window for physics Beyond the SM. To match the high precision data at future colliders on the top quark properties, precise calculations of top quark productions are mandatory. In this chapter, full one-loop electroweak corrections to the processes $e^+e^- \to t\bar{t}$ and $e^+e^- \to t\bar{t}\gamma$ at the ILC are reported. One then investigates the effect of electroweak corrections to the total cross section and the top quark forward-backward asymmetry A_{FB}.

5.1 Top quark physics at the ILC

There are six quarks in the SM theory. They are named up-, down-, charm-, bottom- and top-quark. They are arranged into three generations. The top quark belongs to the third generation with weak-isopin $T_3 = 1/2$ and charge $Q = 2/3$. It is by far the heaviest elementary particle in the SM theory with a mass $m_t = 173.07 \pm 0.52 \pm 0.72$ GeV [59].

Top quark was discovered by D0 and CDF experiments at Tevatron [103, 104] in proton-antiproton collisions. Up to now, the top quark properties have been studied at Tevatron with 1.8 TeV and 1.96 TeV center-of-mass energies. At the LHC, the experimental data have been collected at $\sqrt{s} = 7$ TeV in 2011. The machine has been operated at $\sqrt{s} = 8$ TeV in 2012 [105, 106]. The experimental data, excluding the top quark forward-backward asymmetry, is in agreement with the SM prediction within the large uncertainties.

The ILC is expected to measure top quark properties precisely [14, 107, 118, 108, 109]. To be more specific, the ILC will perform precise measurement on the top quark mass, its decay width and the top quark electroweak couplings as well as the top quark forward-backward asymmetry and the top quark spin correlations, etc. In the following sections, we will discuss the future measurements of the top quark properties at the ILC in greater detail.

The top quark mass

At the ILC the top quark mass will be measured by threshold scan method [14, 107, 108]. Because the top quark is a spin 1/2 fermion, $t\bar{t}$ pairs can be produced as an S-wave state. The production cross section will show a remnant peak in the threshold line shape. Furthermore, the top pairs will be created as a color singlet state in which theoretical prediction of its cross section is obtained very accuracy without hadronization effects. Therefore the study of the cross-section of $t\bar{t}$ production at the threshold allows us to extract the top quark mass m_t, as well as the top quark's decay width Γ_t, and QCD coupling α_s precisely.

QCD corrections to the top pair production at threshold were done by many authors using the non-relativistic effective theories. An NNLO QCD calculation was performed in Ref [111]. In this calculation, the authors performed summation of QCD coulomb singularities at fixed-order expansion. Its method has been extended to NNNLO QCD corrections, as discussed in Ref [112]. Recently, the ultra-soft NNLL corrections have been calculated in Ref [113]. At the current stage, the accuracy from QCD calculation is better than 5%, as shown in the figure 5.1. With high precision

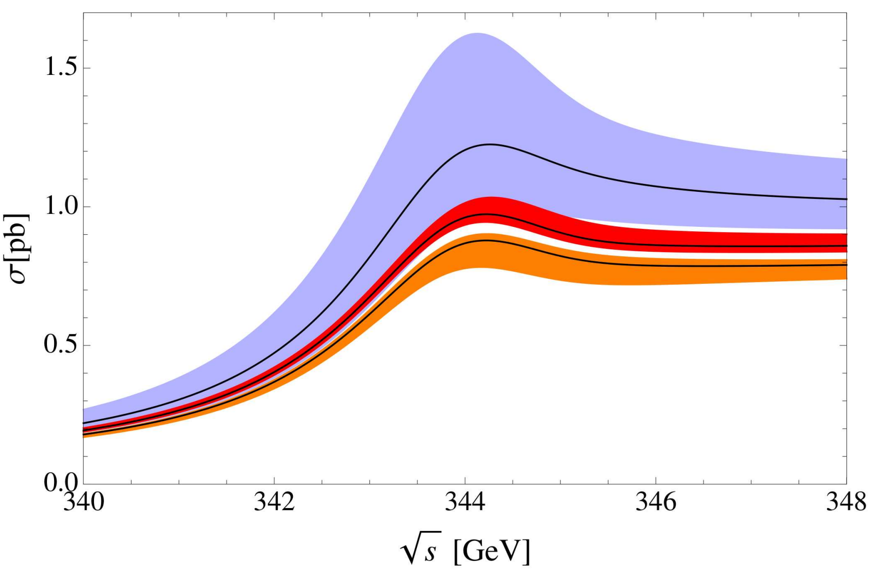

Figure 5.1: The currently stage of the accuracy from QCD calculation is presented. The figure is taken in Ref [114].

at the ILC, the electroweak corrections to the top pairs must be taken into account. Its calculation will be discussed in the next several sections.

The top quark electroweak coupling

The coupling of the top quark to photon and the Z boson can be expressed as the following formula

$$\Gamma_\mu^{t\bar{t}X}(k^2, q, \bar{q}) = ie\Big\{\gamma_\mu\Big(\widetilde{F}_{1V}^X(k^2) + \gamma_5\widetilde{F}_{1A}^X(k^2)\Big) + \frac{(q-\bar{q})_\mu}{2m_t}\Big(\widetilde{F}_{2V}^X(k^2) + \gamma_5\widetilde{F}_{2A}^X(k^2)\Big)\Big\}, \tag{5.1}$$

where k, q and $\bar{q}$ are 4-momenta of photon, top and anti-top quark, respectively. In this formula, X denotes γ or Z. The $\widetilde{F}$ are written in terms of the usual form factors F_1 and F_2 by

$$\widetilde{F}_{1V}^X = -(F_{1V}^X + F_{2V}^X), \quad \widetilde{F}_{2V}^X = F_{2V}^X, \quad \widetilde{F}_{1A}^X = -F_{1A}^X, \quad \widetilde{F}_{2A}^X = -iF_{2A}^X. \tag{5.2}$$

In the SM theory, the form factors $F_{1V}^\gamma(k^2)$ and $F_{1A}^Z(k^2)$ are non-zero. The quantities $F_{2V}^{\gamma,Z}(k^2)$ are the electric (EDM) and weak magnetic dipole moment (MDM) form factors. While $F_{2A}^{\gamma,Z}(k^2)$ are the CP-violating electric dipole moment and the weak electric dipole moment form factors. The precise measurements of these couplings (or these form factors) can be used to explore the new physics contributions.

At the LHC, these couplings are measured by considering the process $pp \to t\bar{t}\gamma$ and $pp \to t\bar{t}Z$. The QCD corrections to these processes were done in Refs [115, 124]. The measurements were performed with taking QCD corrections into account. The results are still with large uncertainties, 10% for F_{1A}^Z and 40% for $F_{2V,A}^Z$ for example [14]. The full electroweak corrections to these processes are ambitious. So far these calculations have not been performed yet.

The ILC provides an ideal environment to measure these couplings. Because the cross section of the process $e^-e^+ \to t\bar{t}$ with γ and Z exchange in s-channel is large. It is order 1 [pb], almost all the SM background can be eliminated. In addition, with the polarized beams of electron and positron the ILC can access independently the couplings of left- and right-handed polarized top quark to the Z boson. Therefore, it is expected that the ILC will measure these couplings precisely. From this, one can extract the new physics effects.

A comparison of precision for CP conserving form factors of top quark coupling to γ and the Z boson at the LHC [117] and the ILC [118]. The LHC results assume an integrated luminosity of 300 fb^{-1}. At the ILC, the results are generated with the integrated luminosity of 500 fb^{-1} in 500 GeV center-of-mass energy and with polarization beams of 80% for electron and 30% for positron. The result shows that the ILC can measure these couplings much more precise than the LHC.

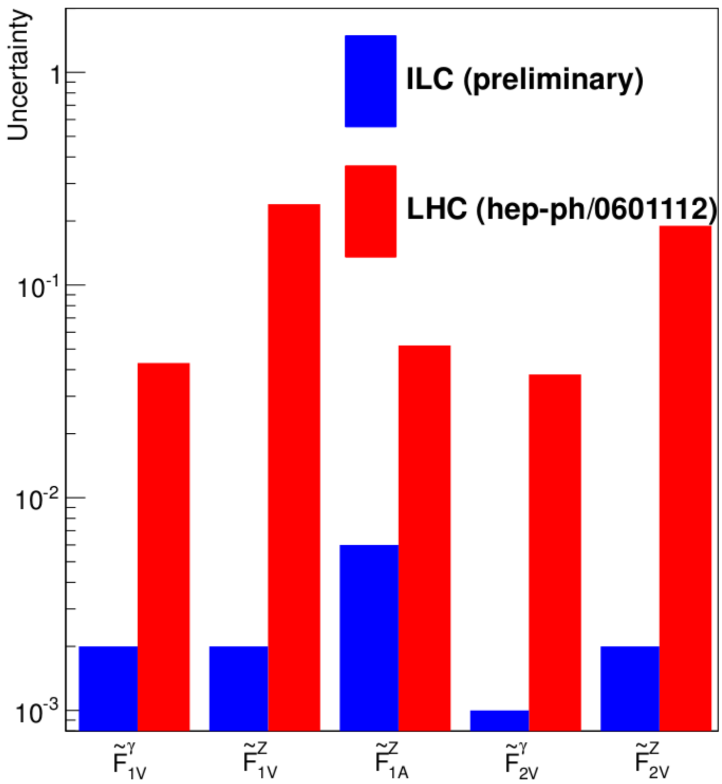

Figure 5.2: A comparison of precision for CP conserving form factors of top quark couplings to γ and the Z boson at LHC and ILC. The figure is taken in Ref [118].

The top quark forward-backward asymmetry

The experimental results of CDF and D0 on the measurement of top-pair production at Tevatron reported an unexpected large top quark forward-backward asymmetry [119, 120]. The precise theoretical calculations of the top-pair production play an important role in explaining the experimental data. One-loop QCD radiative corrections to the production from proton-antiproton collision were calculated by several authors [121], [122], [123],[124], [125]. However, the experimental results are still deviated by almost 3σ from the SM prediction including the NLO QCD and electroweak corrections effects.

The LHC is a proton-proton collider, at 7 TeV for example, only 15% of the interaction happen through $q\bar{q}$ and 85% remaining of the interaction arises from gg. Therefore, the LHC experiment does not measure top quark forward-backward asymmetry. Instead of A_{FB}, the LHC will measure charged asymmetry (A_C). The CMS experiment measured A_C and reported $A_C = 0.004 \pm 0.010$ (stat.)± 0.012 (syst.) [126]. The data agrees with the SM prediction within the relatively large uncertainties.

The measurements at Tevatron and the LHC on top quark production are affected by a huge background from QCD. A good example is the $gg \to t\bar{t}$ reaction. The current result of Tevatron measurements on A_{FB} and the relatively large uncertainties on A_C measurements at the LHC, will be great motivation for the ILC. The top quark forward-backward asymmetry will be measured without QCD background at the ILC.

In summary, top quark properties will be studied precisely at the ILC in the future. In order to match the high precision of experimental data, precise calculations of top pair production and top pair production with hard photon bremsstrahlung are considered. Because the QCD corrections can be factorized into $\sim \frac{\alpha_s}{\pi}$ contribution in the high energy which is far from the top pair threshold. Therefore the electroweak corrections will be more indispensable than the QCD one in these energy region. **For this reason, the full $\mathcal{O}(\alpha)$ electroweak radiative corrections to the both processes $e^+e^- \to t\bar{t}$ and $e^+e^- \to t\bar{t}\gamma$ at the ILC are considered and reported**

in this chapter.

5.2 The process $e^+e^- \to t\bar{t}$ at the ILC

In this section, the calculation of full $\mathcal{O}(\alpha)$ electroweak radiative corrections to the process $e^+e^- \to t\bar{t}$ at ILC is presented. The GRACE-Loop is used to generate the FORTRAN code of this process's amplitude. Before generating the physical results of this reaction, one has to perform firstly the numerical check on the calculation. The results must have ultraviolet and infrared finiteness, and independence of the gauge parameters as usual. In tables (C.9,C.11,C.10) in appendix C, the numerical results of these tests at one random phase space point, are presented. The tests are executed in quadruple precision. One finds that the results are stable over 24 digits. The stability of the results versus the soft photon cutoff parameter (k_c) also is checked. This test includes both the soft photon and the hard photon bremsstrahlung contributions. The hard photon part is the process $e^+e^- \to t\bar{t}\gamma$ with additional photon $E_\gamma \geq k_c$. The result is verified by changing the value of k_c from 10^{-5} GeV to 0.1 GeV. Table (C.12) shows that the results are in agreement with an accuracy which is better than 0.02% (this accuracy is consistent with Monte Carlo integration accuracy).

A completed full one-loop electroweak correction calculation to the process $e^+e^- \to t\bar{t}$ has already been presented in Refs [127, 128, 129]. In this section, the results of this calculation are also cross-checked with previous one in Ref [128]. Table 5.1 shows that the results in this work are in good agreement with the one in Ref [128].

After verifying the calculation, the physical results for this process will be generated by fixing $\lambda = 10^{-17}$ GeV, $C_{UV} = 0$, $k_c = 10^{-3}$ GeV and $\tilde{\alpha} = \tilde{\beta} = \tilde{\delta} = \tilde{\kappa} = \tilde{\varepsilon} = 0$. The total cross section, electroweak corrections as well as top quark forward-backward asymmetry which are shown as a function of center-of-mass energy will be discussed in the next paragraphs.

Table 5.1: Comparison of the total cross section $e^+e^- \to t\bar{t}$ between this work and [128]. The corrections refer to the full one-loop electroweak corrections including hard photon radiation.

$e^+e^- \to t\bar{t}$	This work	[128]
$\sqrt{s} = 500$GeV		
Tree-level (in pb)	0.512275	0.512274
$\mathcal{O}(\alpha)$ (in pb)	0.526371	0.526337
δ (in %)	2.75163	2.74513
$\sqrt{s} = 1$TeV		
Tree-level (in pb)	0.155918	0.155918
$\mathcal{O}(\alpha)$ (in pb)	0.171931	0.171916
δ (in %)	10.2696	10.2602

The total cross-section and electroweak corrections

In fig 5.3, the total cross-section and the full electroweak corrections are presented as a function of the center-of-mass energy $\sqrt{s}$ which is varying from 350 GeV to 1 TeV. In the upper figure, the total cross-section is shown. The red points are the result of the tree level cross-section, while the green points represent the full one-loop QED cross-section, and the blue points are the sum of the tree level cross-section combined with the full one-loop electroweak radiative corrections. The cross-section is largest near the threshold, $\sqrt{s}$ around 440 GeV and it will decrease more and more with increasing center-of-mass energy.

In bottom part of fig 5.3, the full electroweak correction, the genuine weak correction in both the α and the G_μ schemes is presented. The green points represent the QED corrections, the red points are the results of the full electroweak corrections. The triangle points with blue color are the results of the genuine weak correction in the α scheme by subtracting QED corrections. The filled rectangle points in blue represent the results of the genuine weak correction in the G_μ scheme. These corrections are shown as a function of the center-of-mass energy, $\sqrt{s}$ which is ranging from 350 GeV to 1 TeV. The figure indicates clearly that the QED correction is dominant in the low energy region. In the high energy region it is much smaller ($\sim 12\%$ at 1 TeV). One also finds that the genuine weak correction in the G_μ scheme varies from 5% to -5% over a range of $\sqrt{s}$ from 350 GeV to 1 TeV. The corrections make significant contributions and must be taken into account at the ILC.

The relevant distributions

In fig 5.4, the angular distributions of top quark are presented at $\sqrt{s} = 500$ GeV (left figure) and at $\sqrt{s} = 1$ TeV (right figure). The points in red color are the result of the tree level calculation and the points in blue color represent the result of including the full radiative corrections. One observes clearly that the corrections are of sizeable contribution in the negative region of $\cos\theta_{\rm top}$. It is very important information for the precise evaluation of top quark asymmetry.

Now we turn our attention to the top quark forward-backward asymmetry A_{FB}. This quantity is defined as

$$A_{FB} = \frac{\sigma(0^\circ \le \theta_t \le 90^\circ) - \sigma(90^\circ \le \theta_t \le 180^\circ)}{\sigma(0^\circ \le \theta_t \le 90^\circ) + \sigma(90^\circ \le \theta_t \le 180^\circ)}, \tag{5.3}$$

with θ_t the angle of the top quark.

The top quark forward-backward asymmetry and its electroweak corrections are shown as a function of the center-of-mass energy in Fig 5.5. It is observed clearly that the top quark asymmetry in the full results is smaller than the asymmetry at the tree level results only. In the bottom Fig 5.5, the electroweak corrections are significant impact to A_{FB}. It ranges from -12% to -10% with 500 GeV $\le \sqrt{s} \le 1$ TeV. Such corrections must be taken into account at the ILC. Moreover, with high precision program at the ILC, it is clear that a two-loop correction must be considered to this process. This topic will be discussed in the future.

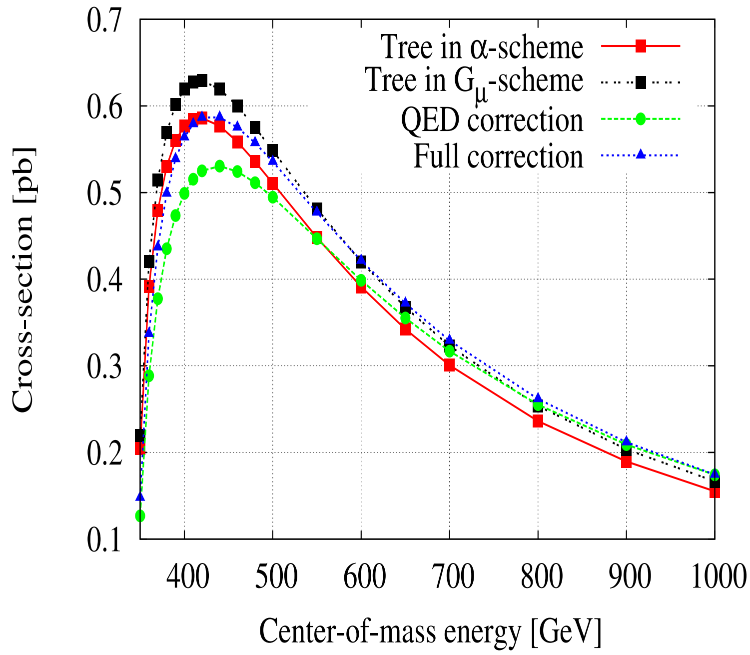

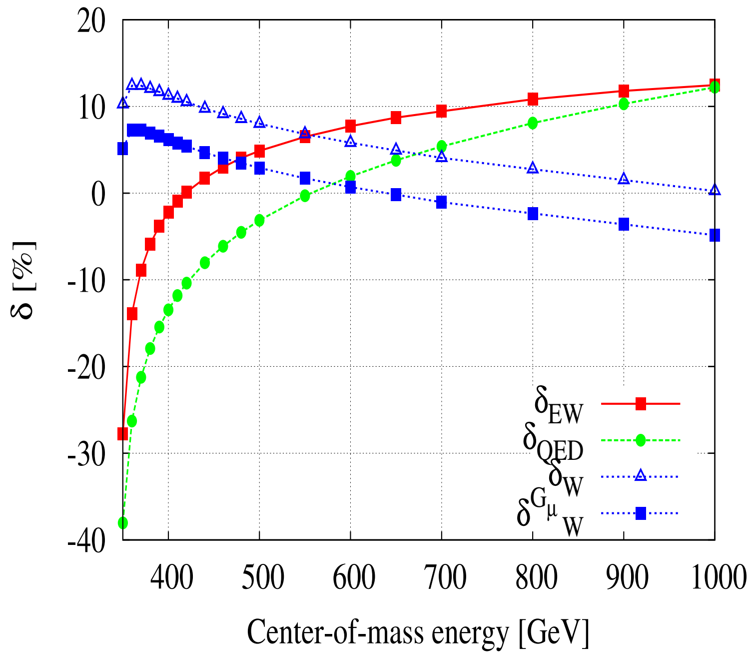

Figure 5.3: The total cross-section and the full electroweak corrections as a function of the center-of-mass energy $\sqrt{s}$.

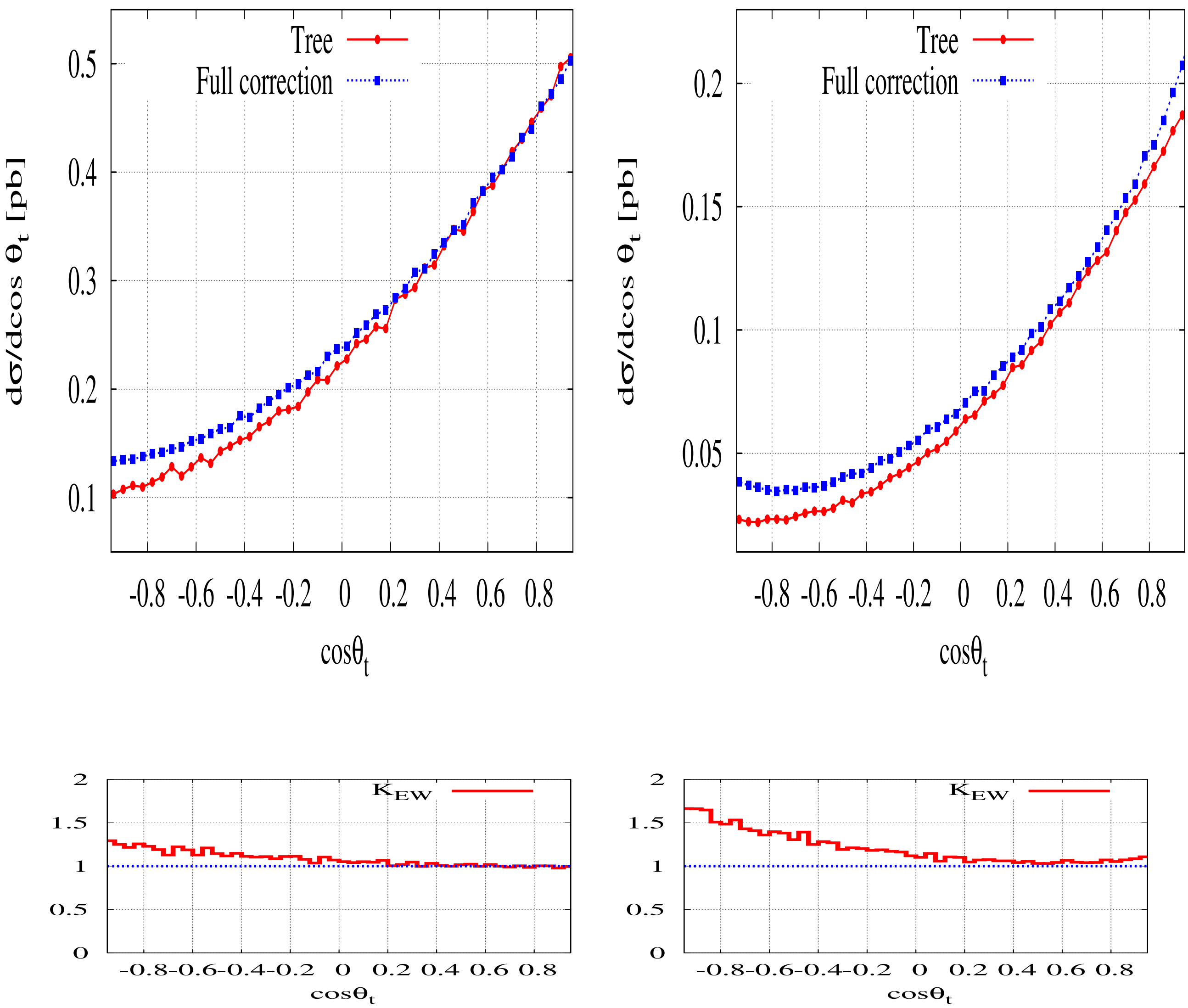

Figure 5.4: The angular distributions of the top quark at $\sqrt{s} = 500$ GeV and $\sqrt{s} = 1$ TeV.

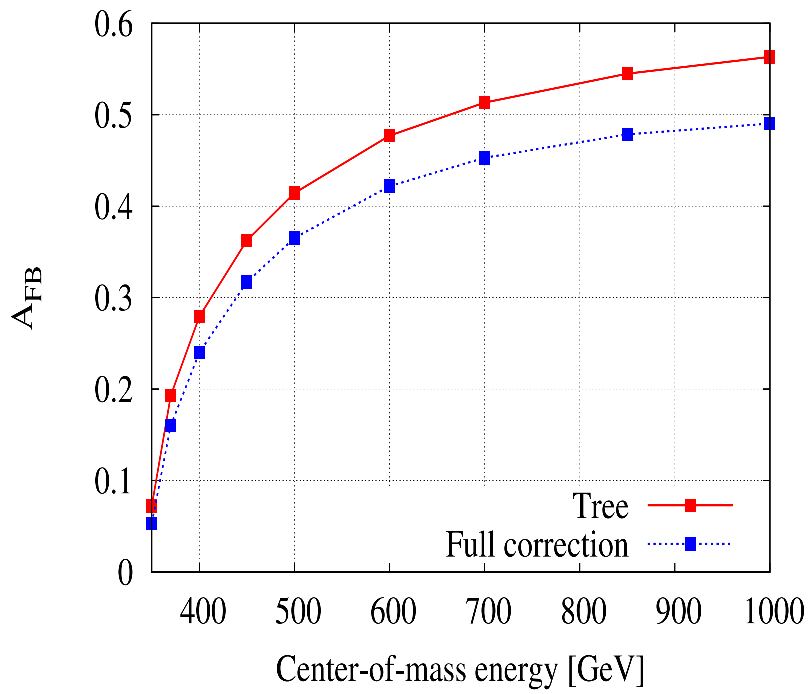

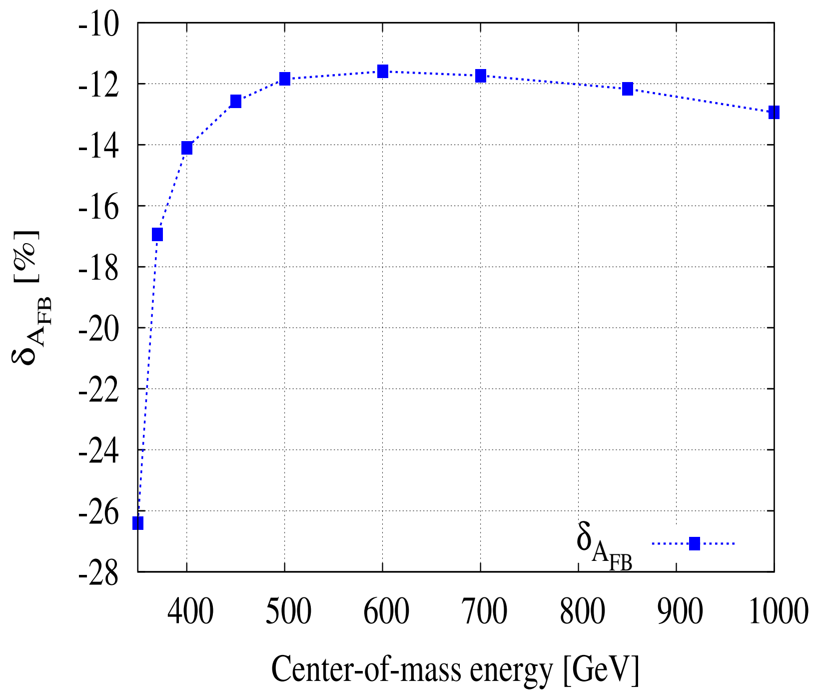

Figure 5.5: The top quark forward-backward asymmetry and its electroweak correction as a function of the center-of-mass energy.

5.3 The process $e^+e^- \to t\bar{t}\gamma$ at the ILC

We are changing our topic to the process $e^+e^- \to t\bar{t}\gamma$ at the ILC. The calculations are performed with the help of GRACE-Loop program. The full Feynman diagrams will be generated automatically by GRACE-Loop. With the non-linear gauge fixing as described in chapter 2, the full set of Feynman diagrams includes 16 tree diagrams and 1704 one-loop diagrams (of which 168 are pentagon diagrams) in covariant gauge. Fig 5.6 shows some selected diagrams.

The axial gauge for external photon which is discussed in chapter 4, is carried out for this calculation. After obtaining the FORTRAN code of the squared amplitude of the process. The calculation will be checked numerically as usual. In tables (C.13,C.15,C.14) of appendix C, the numerical results of the ultraviolet finiteness, the gauge invariance and the infrared finiteness are presented at one random phase space point. The k_c stability of the result is also presented in table C.16 of appendix C. The tests are performed in quadruple precision. The results are stable over 20 digits in the checks. For the k_c stability of the results, one also finds that the results are in good agreement to an accuracy of 0.05% which is consistent with the one in Monte Carlo integration. In order to generate the physical results, we again set $\lambda = 10^{-17}$ GeV, $C_{UV} = 0$, $k_c = 10^{-3}$ GeV and $\tilde{\alpha} = \tilde{\beta} = \tilde{\delta} = \tilde{\kappa} = \tilde{\varepsilon} = 0$.

The total cross-section and electroweak corrections

Our input parameters for the calculation are used as in appendix B. In addition, an energy cut of $E_\gamma^{\rm cut} \geq 10$ GeV and an angle cut of $10^\circ \leq \theta_\gamma^{\rm cut} \leq 170^\circ$ are implied for the external photon.

In fig 5.7 the total cross section and the full electroweak corrections are presented as a function of the center-of-mass energy $\sqrt{s}$ varying from 360 GeV to 1 TeV. In the upper figure, the red points are the result of the tree level cross-section while the blue points are the sum of the tree level cross-section combined with the full one-loop

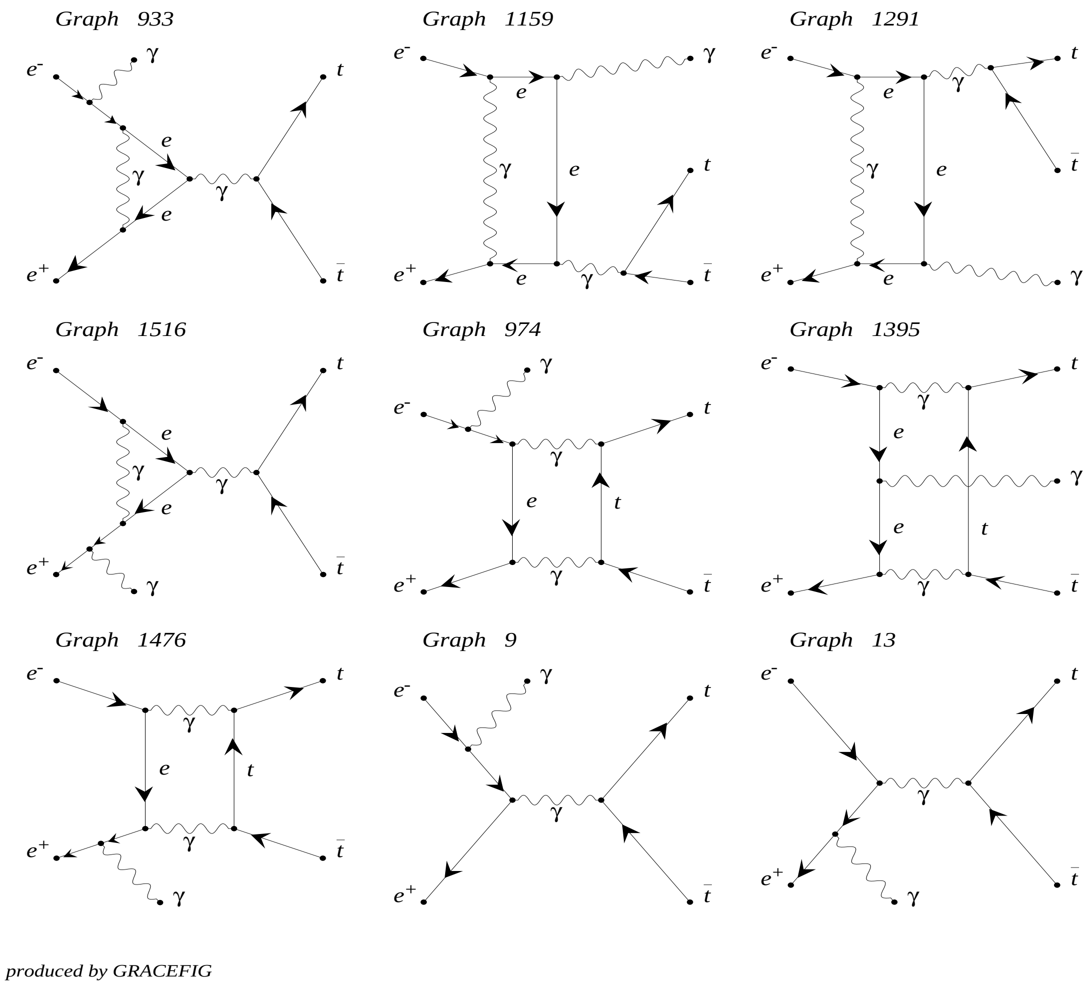

Figure 5.6: Selected Feynman diagrams generated by the GRACE-Loop program.

electroweak radiative corrections. The cross section is largest near the threshold, $\sqrt{s}$ around 550 GeV. It will decrease with increasing center-of-mass energy. In comparison with $t\bar{t}$ production, the total cross section of the $t\bar{t}\gamma$ production is considerable less than 10% of the one in the $t\bar{t}$ reaction. In addition one finds a negative correction for the $t\bar{t}\gamma$ production in contrast to the positive correction for the $t\bar{t}$ production.

In bottom part of fig 5.7, the full electroweak correction and the genuine weak correction are presented in both the α and G_μ schemes. The green points represent the QED correction, the red points are the results of the full electroweak correction. While the blue points are the results of the genuine weak correction in the α scheme. The filled rectangle points in blue color represent the results of the genuine weak correction in the G_μ scheme. These corrections are shown as a function of the center-of-mass energy. The figure shows clearly that the QED correction is dominant in the low energy region. In the high energy region it is much smaller ($\sim$ 5% at 1 TeV). In contrast to the QED correction the weak correction in the α scheme is less than 10% for low energies but reaches -24% at 1 TeV center-of-mass energy. The genuine weak correction in G_μ scheme varies from $\sim$ 2% to -31% over $\sqrt{s}$ from 360 GeV to 1 TeV. The corrections are significant contributions and must be taken into account at the ILC.

The relevant distributions

In fig 5.8, the distributions of the cross section as a function of photon energy are presented at $\sqrt{s} = 500$ GeV (left figure) and $\sqrt{s} = 1$ TeV (right figure). The points in red color are the result of the tree level calculation and the points in blue color represent the result including the full radiative corrections. The distributions also indicate that the radiative corrections are significant in the boundary region of these distributions.

The angular distributions of photon are shown at $\sqrt{s} = 500$ GeV and 1 TeV in figure 5.9. One observes a symmetric shape for the distributions. The distributions

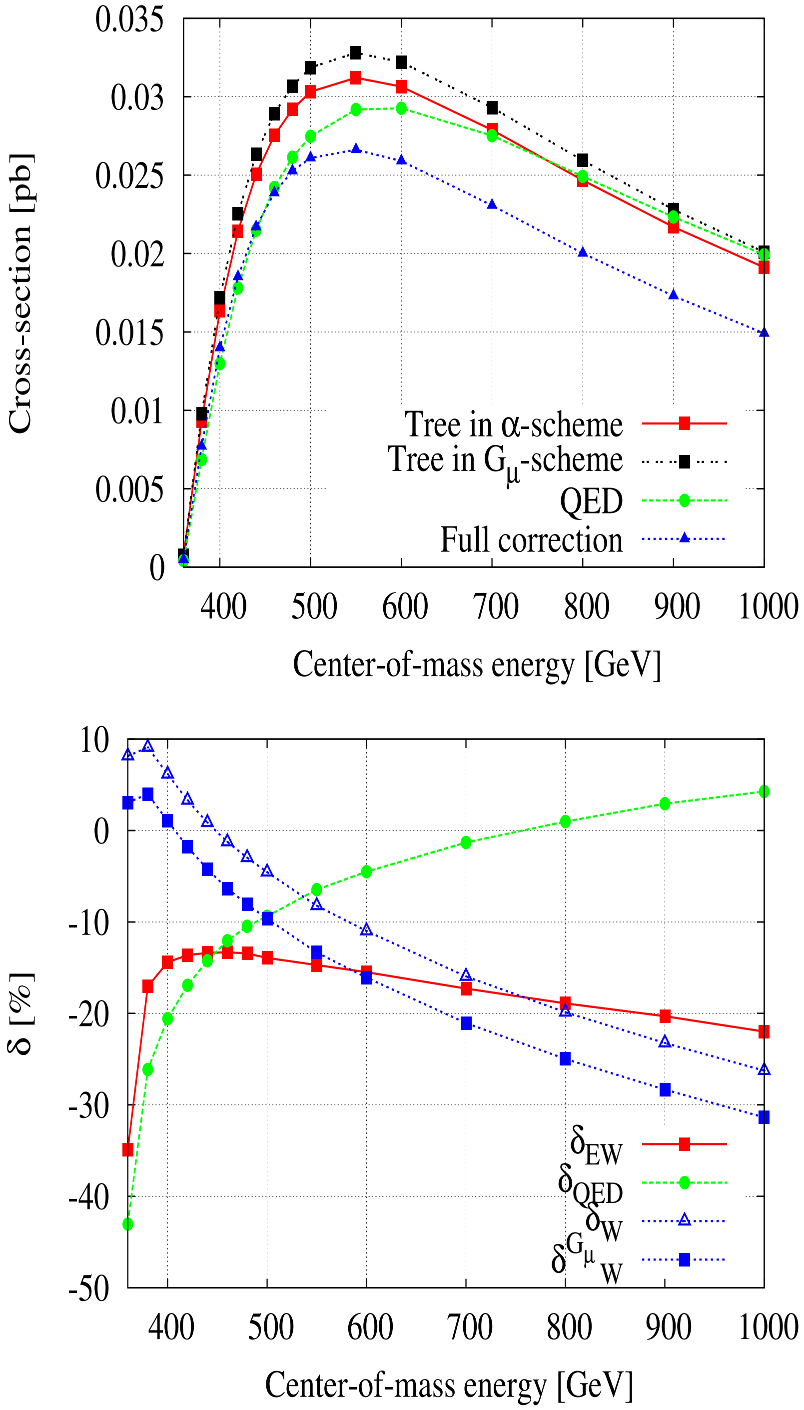

Figure 5.7: The total cross-section and the full electroweak corrections are presented as a function of the center-of-mass energy $\sqrt{s}$.

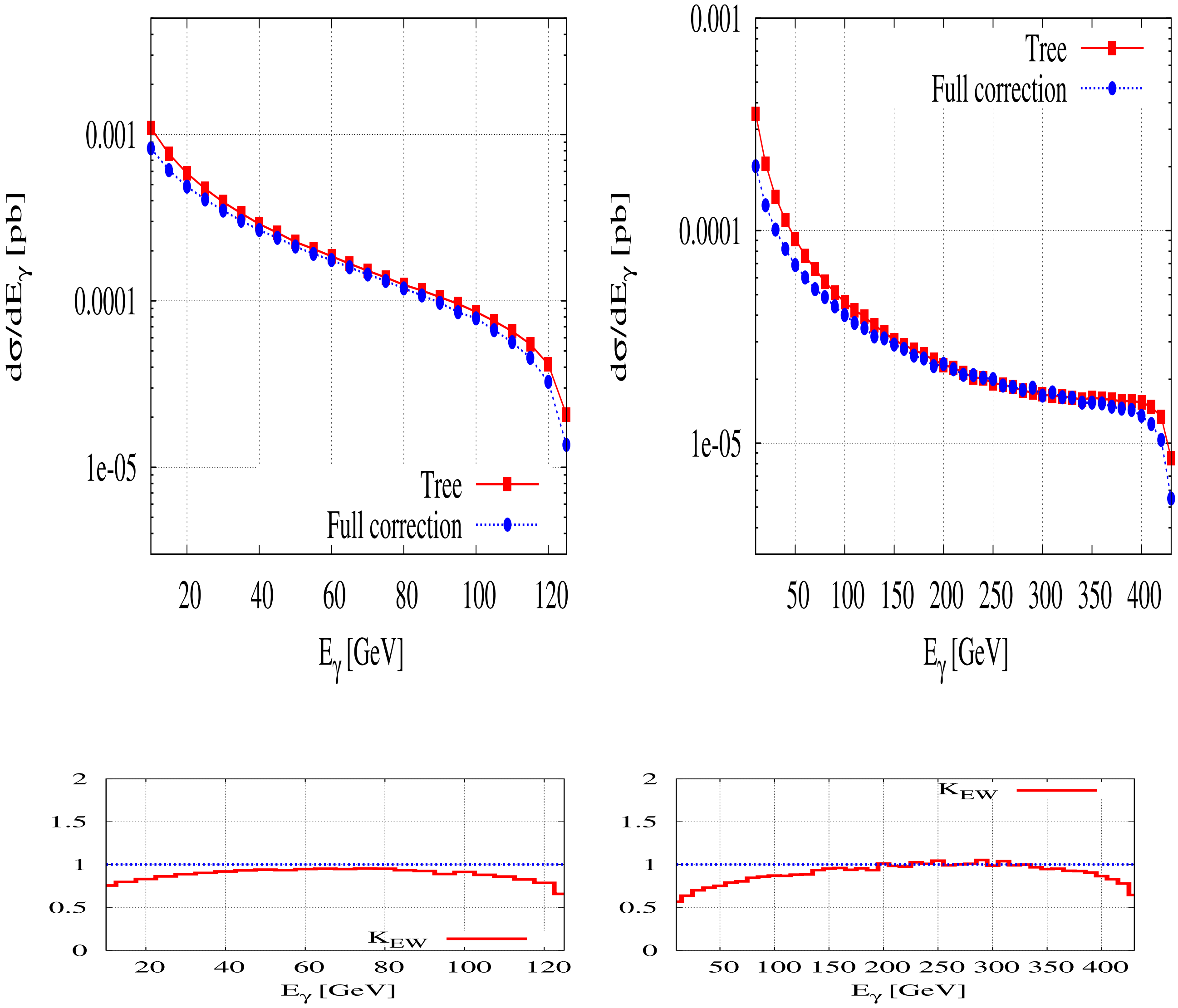

Figure 5.8: The distribution of the cross section as a function of photon energy at $\sqrt{s} = 500$ GeV (left figure) and at $\sqrt{s} = 1$ TeV (right figure).

show clearly that the electroweak corrections make visible impact.

The angular distributions of the top quark are shown at $\sqrt{s}$ = 500 GeV and at 1 TeV in figure 5.10. We find that electroweak corrections form a significant contribution in the region of $\cos\theta_{\rm top} > 0$.

In fig 5.11, the distributions of the cross section as a function of the invariant mass of the top quark and photon ($m_{\gamma t}$), are presented at $\sqrt{s}$ = 500 GeV and at $\sqrt{s}$ = 1 TeV. The cross section decreases with increasing $m_{\gamma t}$. One finds that the radiative corrections are of sizeable contributions at the peak ($m_{\gamma t}$ = 182 GeV) and at the boundary of the distributions. The corrections provide important information to distinguish $t\bar{t}\gamma$ from $t\bar{t}$ events at the ILC.

Fig 5.12 shows the results for A_{FB} as a function of the center-of-mass energy. The figure indicates clearly that the top quark asymmetry in the full results is smaller than the asymmetry at the tree level results only. In the bottom figure, the electroweak corrections to A_{FB} are presented as a function of the center-of-mass energy. It is very interesting to observe that the electroweak corrections make sizeable impact (order 10% contribution). Such corrections must be considered in future colliders.

A short conclusion of this chapter: The electroweak corrections to $t\bar{t}$ and $t\bar{t}\gamma$ productions are of significant impact to the total cross section as well as its relevant distributions. With high precision at the ILC, the corrections must be taken into account. The results in this calculation also point out that a two-loop electroweak correction to the $t\bar{t}$ production is necessary for the future collider, the ILC.

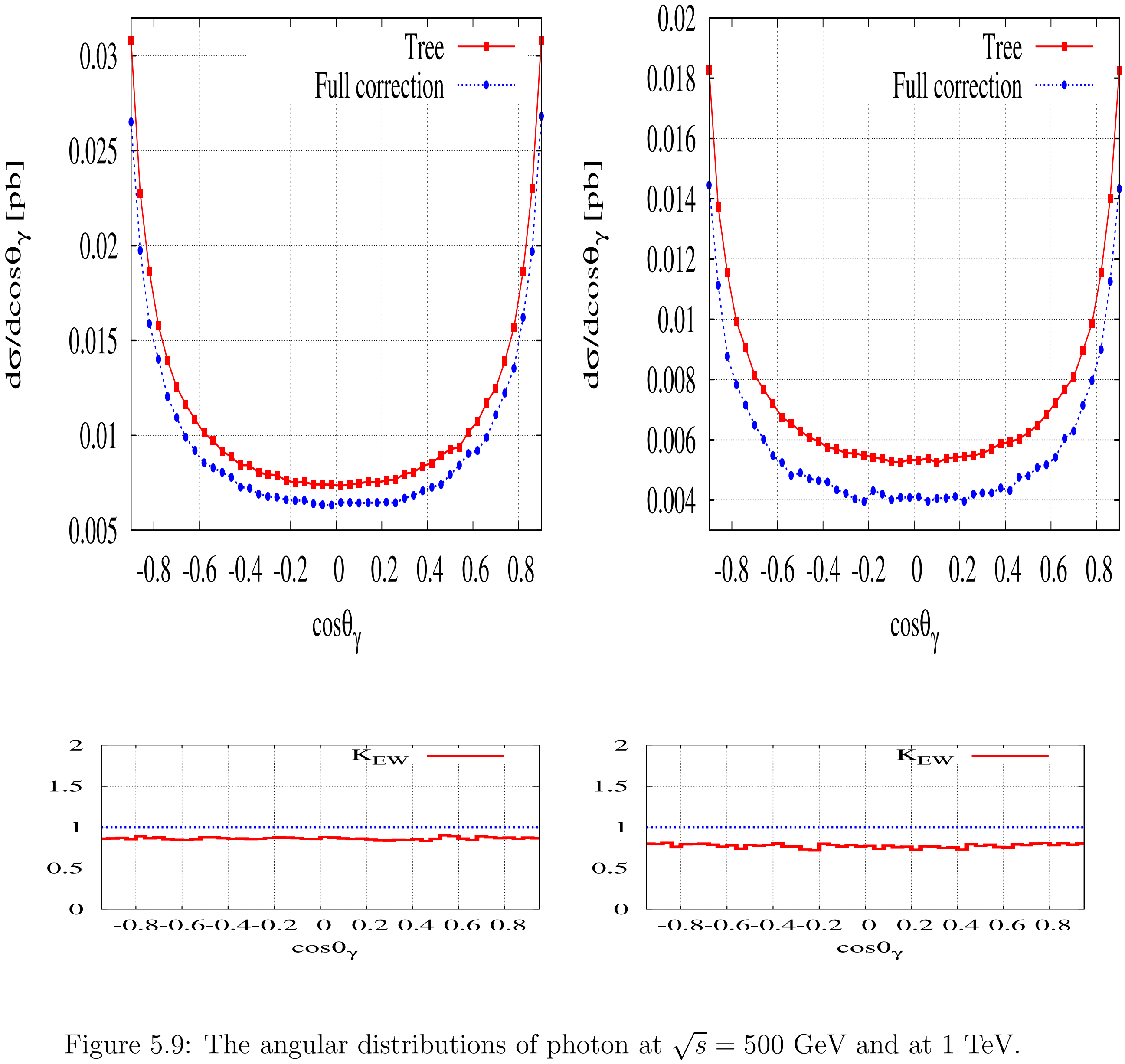

Figure 5.9: The angular distributions of photon at $\sqrt{s} = 500$ GeV and at 1 TeV.

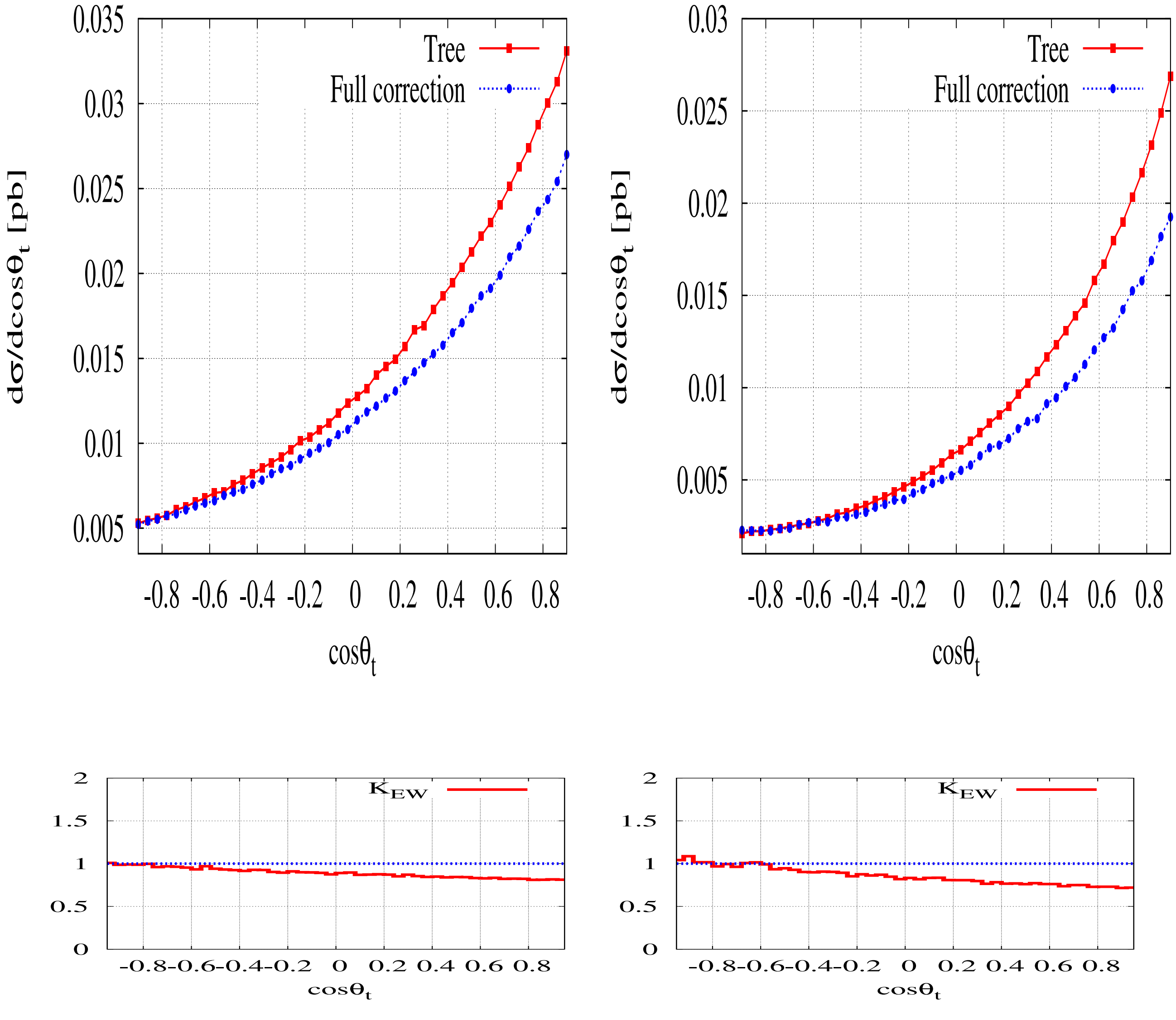

Figure 5.10: The angular distributions of top at $\sqrt{s} = 500$ GeV and at 1 TeV.

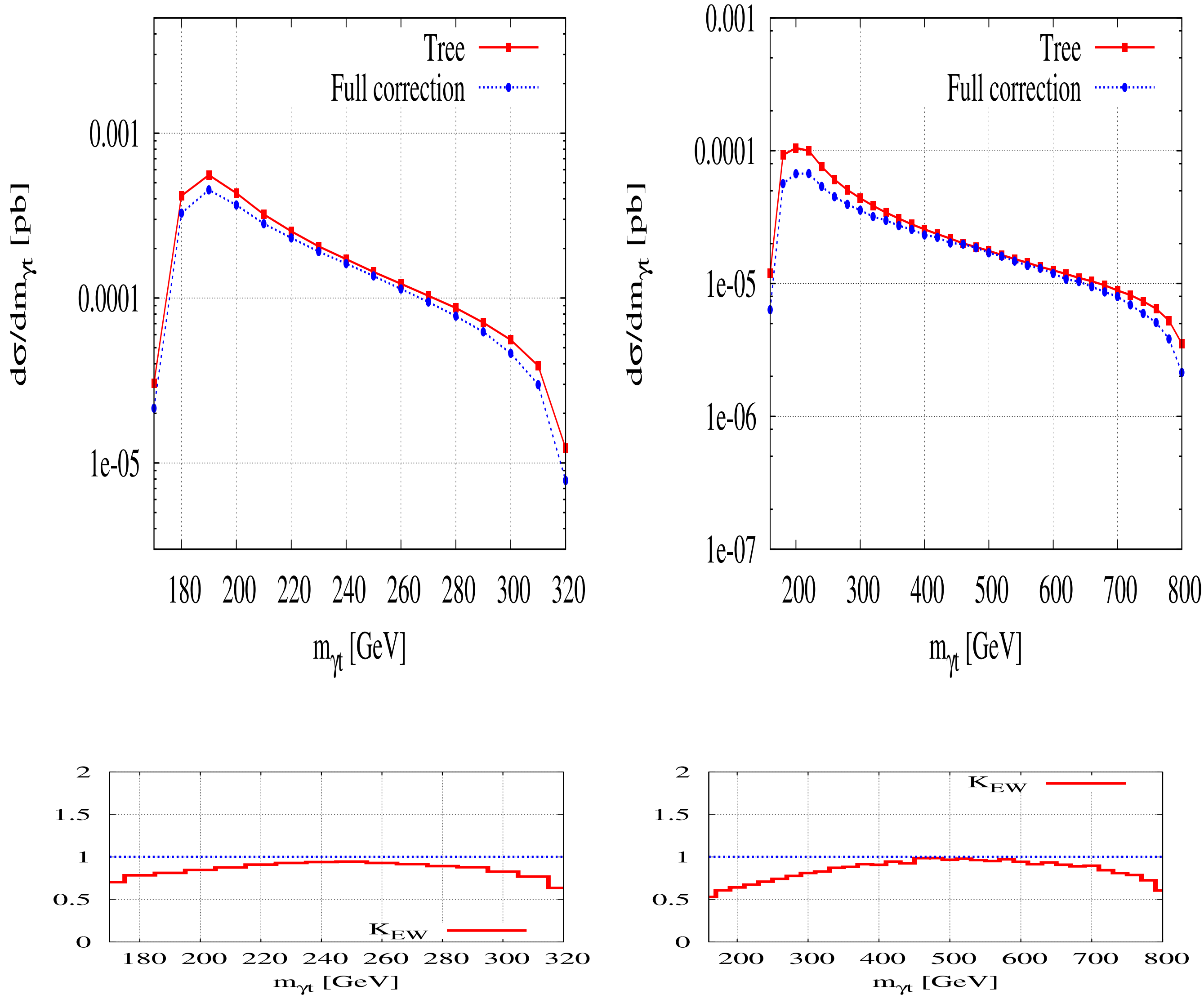

Figure 5.11: The distributions of the cross section as a function of the invariant mass of the top quark and photon ($m_{\gamma t}$) at $\sqrt{s} = 500$ GeV and $\sqrt{s} = 1$ TeV.

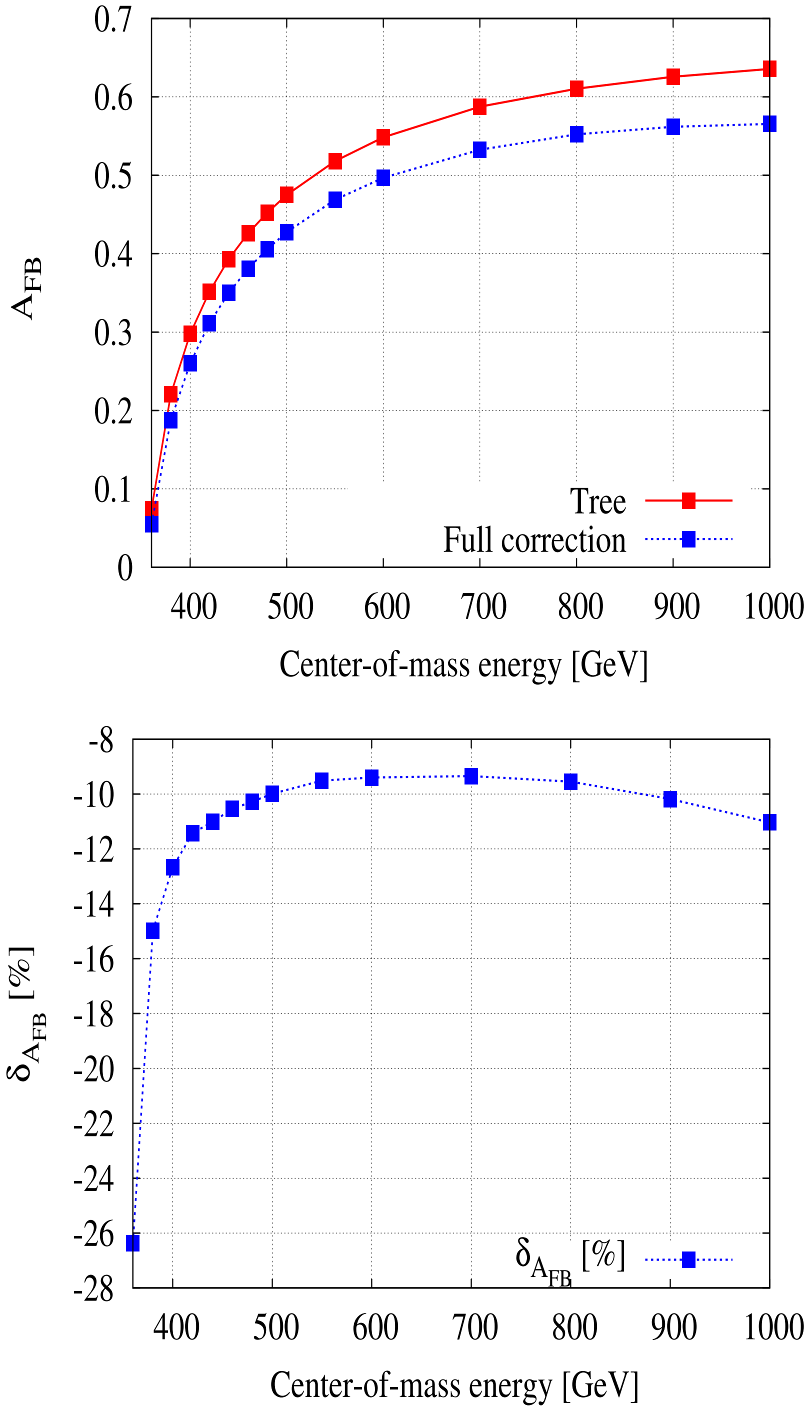

Figure 5.12: The top quark forward-backward asymmetry and its electroweak corrections as a function of the center-of-mass energy.

Chapter 6

Conclusions

In this thesis, we upgraded the GRACE-Loop which is a generic automatic computer program for calculating High Energy Physics processes at one-loop electroweak corrections. In particular, the thesis is concerned to study the method for the tensor reduction for one-loop five-point functions in Ref [16]. We then implemented it into GRACE-Loop thereby providing a useful tool to check the calculation on one-loop five-point functions. The test is performed by comparing the result of one-loop five point functions generated by the method in Ref [16] to the one in GRACE-Loop [21].

The full $\mathcal{O}(\alpha)$ electroweak radiative corrections to some of the most important processes at future colliders are performed successfully in this thesis. These processes are calculated firstly in the thesis.

At the LHC, the calculation of $pp \rightarrow W^-W^+$ and $pp \rightarrow W^-W^+ + 1$ jet are performed. Such processes are very important to reduce the background for Higgs searches. The processes also improve the future precision on vector boson properties. The physical results of the calculations are discussed, one finds that in high P_{T}-region of the jet where the new physics signatures are expected, the electroweak corrections are of significant impact (order 10%). Such corrections play an important role to study the new physics signals at the future LHC.

At the ILC, full $\mathcal{O}(\alpha)$ electroweak radiative corrections to $e^-e^+ \to e^-e^+\gamma$ are also done successfully in this thesis. The electroweak corrections form a significant contributions to the total cross section as well as its relevant distributions. These contributions must be taken into account for luminosity measurement at the ILC. The calculation provides a framework for future calculation that is the process $e^-e^+ \to e^-e^+\gamma$ with soft bremsstrahlung photon, and subsequently the calculation for full two-loop corrections to Bhabha scattering later.

Moreover, we computed full one-loop electroweak corrections to the processes $e^-e^+ \to t\bar{t}$ and $e^-e^+ \to t\bar{t}\gamma$ at the ILC. In the physical results, the impact of electroweak corrections to the total cross section, the top quark forward-backward asymmetry A_{FB} are examined. The electroweak corrections make a sizeable impact (order 10%) to the total cross section and its relevant distributions. The impact must be taken into consideration for high precision measurements on the top quark properties at the ILC. The results in this thesis also point out that a two-loop electroweak corrections to the top pair production are necessary for the ILC.

For the future development, we plan to focus on implementing polarized beams for electron and positron into GRACE-Loop. One-loop corrections to the ILC processes with polarized beams for electron and positron will be performed automatically with the GRACE-loop program in near future. In addition, full two-loop electroweak corrections to the top pair production as well as Bhabha scattering will be proposed in the next step. As a far future project, we are also interested in the event generation at the LHC and the ILC at level of one-loop corrections with GRACE-Loop.

Appendix A

The counterterm

In the GRACE-Loop program, the electroweak counterterms of gluon-quark-antiquark are missing ($\delta_{gQ\bar{Q}}$) with Q noted for quarks. These counterterms will be calculated analytically and implemented into GRACE-Loop in this section.

In order to calculate the counterterms, one considers all one-loop vertex diagrams contributed to the process $g \to u\bar{u}$. Then the electroweak counterterms of $\delta_{gQ\bar{Q}}$, will be general from this result. In this calculation, we keep non-zero of quark masses and apply on-shell condition as Eq. 2.22. The field strength renormalization of u-quark is written by (see Ref [68] for more detail)

$$\Big(Z_\psi^{1/2}\Big)_{uu} = \Big(Z_\psi^{1/2}\Big)_{\bar{u}\bar{u}} = 1 - \frac{1}{2}\Bigg\{\Big(\delta Z_\psi^{1/2}\Big)^\gamma_{uu} + \Big(\delta Z_\psi^{1/2}\Big)^Z_{uu} + \Big(\delta Z_\psi^{1/2}\Big)^W_{uu} + \Big(\delta Z_\psi^{1/2}\Big)^\chi_{uu}\Bigg\},$$

with

$$\begin{aligned}
\Big(\delta Z_\psi^{1/2}\Big)^\gamma_{uu} &= e^2 Q_u^2\Big(C_{UV} - \log(m_u^2) + 4 - 2\log(\frac{m_u^2}{\lambda^2})\Big), \\
\Big(\delta Z_\psi^{1/2}\Big)^Z_{uu} &= (C_V^{(u)} + C_A^{(u)}\gamma_5)^2\Big(C_{UV} - \frac{1}{2} - \log(M_Z^2)\Big), \\
\Big(\delta Z_\psi^{1/2}\Big)^W_{uu} &= 2C_W^2(1-\gamma_5)\Big(C_{UV} - \frac{1}{2} - \log(M_W^2)\Big)\Bigg\}, \\
\Big(\delta Z_\psi^{1/2}\Big)^\chi_{uu} &= -C_W^2(1-\gamma_5)\frac{m_d^2}{M_W^2}\Big(C_{UV} - 2F_0(m_d, M_W, m_u^2)\Big).
\end{aligned}$$

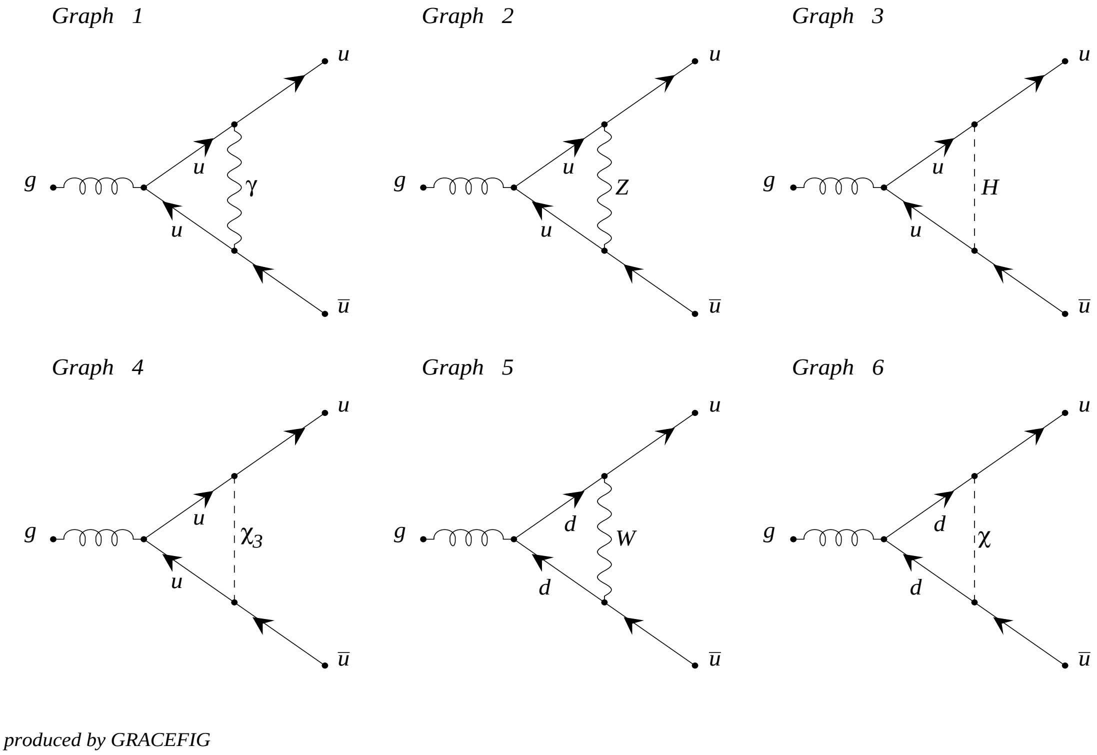

Figure A.1: One-loop vertex diagrams which contributed to the $g \to u\bar{u}$

Where the functions F_0, F_1 are presented in the appendix E and the coefficients $C_V^{(f)}$, $C_A^{(f)}$ (f is denoted for the fermions), C_W are given

$$\begin{aligned} C_V^{(f)} &= C_Z(T_{3f} - 2Q_f \frac{M_Z^2 - M_W^2}{M_Z^2}), \\ C_A^{(f)} &= -C_Z T_{3f}, \end{aligned}$$

with

$$C_Z = -\frac{eM_Z^2}{2M_W\sqrt{M_Z^2 - M_W^2}}, \quad C_W = \frac{eM_Z}{2\sqrt{2(M_Z^2 - M_W^2)}}.$$

- The contribution of diagram 1:

$$\Gamma_{(\gamma)}(q^2=0) \;=\; \frac{e^2Q_f^2}{16\pi^2}\left(C_{UV}-\log(m_u^2)+4-2\log\left(\frac{m_u^2}{\lambda^2}\right)\right)=\frac{1}{16\pi^2}\left(\delta Z_\psi^{1/2}\right)_{uu}^{\gamma}$$

- The contribution of diagram 2:

$$\Gamma_{(Z)}(q^2=0) \;=\; \frac{1}{16\pi^2}(C_v^{(f)}+C_A^{(f)}\gamma_5)^2\left(C_{UV}-\frac{1}{2}-\log(M_Z^2)\right)=\frac{1}{16\pi^2}\left(\delta Z_\psi^{1/2}\right)_{uu}^{Z}$$

- The contribution of diagram 3 + 4:

$$\Gamma_{(H+\chi_3)}(q^2=0)\Big|_{m_{u,d}<<M_W} \;=\; 0$$

- The contribution of diagram 5:

$$\begin{aligned}\Gamma_{(W)}(q^2=0) &= \frac{2C_W^2(1-\gamma_5)}{16\pi^2}\left(C_{UV}-2-2F_1(M_W^2,m_d,m_u^2)\right)\\ &= \frac{2C_W^2(1-\gamma_5)}{16\pi^2}\left(C_{UV}-\frac{1}{2}-\log(M_W^2)\right)\Big|_{m_{u,d}<<M_W}\end{aligned}$$

- The contribution of diagram 6:

$$\Gamma_{(\chi)}(q^2=0)\Big|_{m_{u,d}<<M_W} \;=\; 0$$

The sum of all the contributions is

$$\begin{aligned}g_sT_{ij}^a\Gamma_{g\to u\bar{u}}(q^2\to 0) &= g_sT_{ij}^a+g_sT_{ij}^a\left[\left(\delta Z_\psi^{1/2}\right)_{uu}^{\gamma}+\left(\delta Z_\psi^{1/2}\right)_{uu}^{Z}\right]\\ &\quad+g_sT_{ij}^a\frac{2C_W^2(1-\gamma_5)}{16\pi^2}\left[C_{UV}-\frac{1}{2}-\log(M_W^2)\right]\\ &\quad+g_sT_{ij}^a\left[\delta Y_s+2\left(\delta Z_\psi^{1/2}\right)_{uu}\right]\end{aligned} \tag{A.1}$$

The last term in Eq. (A.1) comes from the counterterm definition in on-shell renormalization where δY_s play the same role as δY in Eq. (2.23). Because we calculate the electroweak counteterms, the strong coupling can be factorized, we can then apply condition $q^2 \to 0$ to get these counterterms.

At the limit $q^2 \to 0$, the right hand side of Eq. (A.1), $g_s T^a_{ij} \Gamma_{g\, u\bar{u}}(q^2 = 0) \to g_s T^a_{ij}$. By solving this equation, one obtains δY_s is

$$0 = -\frac{2C_W^2(1-\gamma_5)}{16\pi^2}\left(C_{UV} - \frac{1}{2} - \log(M_W^2)\right) + \delta Y_s - \left(\delta Z_\psi^{1/2}\right)^W_{uu}, \tag{A.2}$$

or

$$\begin{aligned}\delta Y_s &= -\frac{2C_W^2(1-\gamma_5)}{16\pi^2}\left(C_{UV} - \frac{1}{2} - \log(M_W^2)\right) \\ &\quad + \frac{2C_W^2}{16\pi^2}(1-\gamma_5)\Big(C_{UV} - \frac{1}{2} - \log(M_W^2)\Big) \\ &= 0.\end{aligned}$$

The counterterms of $gQ\bar{Q}$ are

$$\delta_{gQ\bar{Q}} = g_s T^a_{ij}\left[\left(\delta Z_\psi^{1/2}\right)_L P_L + \left(\delta Z_\psi^{1/2}\right)_R P_R\right]$$

where $P_{L,R} = \dfrac{1 \mp \gamma_5}{2}$.

Appendix B

The input parameters

1. For the calculation of the processes $pp \to W^+W^- + 1$ jet at the LHC and $e^-e^+ \to t\bar{t}, t\bar{t}\gamma$ at the ILC. Our input parameters for the calculation are as follows.

   The fine structure constant in the Thomson limit is $\alpha^{-1} = 137.0359895$. For the boson masses, we input $M_H = 126$ GeV, $M_Z = 91.1876$ GeV and $M_W = 80.385$ GeV. For the lepton masses we take $m_e = 0.510998928$ MeV, $m_\tau = 1776.82$ MeV and $m_\mu = 105.6583715$ MeV. For the quark masses we take $m_u = 2.3$ MeV, $m_d = 4.8$ MeV, $m_c = 1.275$ GeV, $m_s = 95$ MeV, $m_t = 173.5$ GeV and $m_b = 4.18$ GeV.

2. For the calculation of the processes $e^-e^+ \to e^-e^+\gamma$ at the ILC. We used the following input parameters for the calculation:

   The fine structure constant in the Thomson limit is $\alpha^{-1} = 137.0359895$. The mass of the Z boson is $M_Z = 91.1876$ GeV and its decay width is $\Gamma_Z = 2.35$ GeV. The mass of W boson is 80.370 GeV. The mass of the Higgs boson is taken to be $M_H = 126$ GeV. For the lepton masses we take $m_e = 0.51099891$ MeV,

$m_\mu = 105.658367$ MeV and $m_\tau = 1776.82$ MeV. For the quark masses, we take $m_u = 63$ MeV, $m_d = 63$ MeV, $m_c = 1.5$ GeV, $m_s = 94$ MeV, $m_t = 173.5$ GeV, and $m_b = 4.7$ GeV.

Appendix C

The numerical checks

In this section, we present the numerical checks of the processes: $e^-e^+ \to t\bar{t}$, $e^-e^+ \to t\bar{t}\gamma$, $e^-e^+ \to e^-e^+\gamma$ and $pp \to W^-W^+$+1 jet. This test is done in quadruple precision. The test is performed with the input parameters in the appendix B and all particle decay widths are zero.

C.1 The process $pp \to W^-W^+ + 1$ jet

We present here the numerical check of the partonic process $u\bar{u} \to W^-W^+\mathrm{g}$ as a typical example.

Table C.1: Test of the C_{UV} independence of the amplitude. In this table, we take the non-linear gauge parameters to be 0, $\lambda = 10^{-17}$GeV and we use 1 TeV for the center-of-mass energy.

C_{UV}	$2\Re(\mathcal{M}_{Loop}\mathcal{M}^+_{Tree})$
0	$-2.17621522282445555075451409469966 2\cdot 10^{-2}$
100	$-2.176215222824455550754514094641724 \cdot 10^{-2}$
10000	$-2.176215222824455550754514086675337 \cdot 10^{-2}$

Table C.2: Gauge invariance of the amplitude. In this table, we set $C_{UV} = 0$, the photon mass is 10^{-17}GeV and a 1 TeV center-of-mass energy.

$(\tilde{\alpha}, \tilde{\beta}, \tilde{\delta}, \tilde{\kappa}, \tilde{\epsilon})$	$2\Re(\mathcal{M}_{Loop}\mathcal{M}^{+}_{Tree})$
(0, 0, 0, 0, 0)	$-2.1762152228244555507545140946996 62 \cdot 10^{-2}$
(10, 20, 30, 40, 50)	$-2.176215222824455541082878599204204 \cdot 10^{-2}$
(100,200,300,400,500)	$-2.176215222824454748167191081738448 \cdot 10^{-2}$

Table C.3: Test of the IR finiteness of the amplitude. In this table we take the non-linear gauge parameters to be 0, $C_{UV} = 0$ and the center-of-mass energy is 1 TeV.

λ [GeV]	$2\Re(\mathcal{M}_{Loop}\mathcal{M}^{+}_{Tree})$+ soft contribution
10^{-17}	$-6.467836618603578841914360532356915 \cdot 10^{-3}$
10^{-20}	$-6.467836618603578834862850466823008 \cdot 10^{-3}$
10^{-25}	$-6.467836618603578834855574257897242 \cdot 10^{-3}$

Table C.4: Test of the k_c-stability of the result. We choose the photon mass to be 10^{-17} GeV and the center-of-mass energy is 200 GeV. The second column presents the hard photon cross section and the third column presents the soft photon cross section. The final column is the sum of both. The statistical error of integration step is below 0.1% for this test.

k_c [GeV]	σ_S [pb]	σ_H [pb]	σ_{S+H} [pb]
10^{-1}	0.551	3.834	4.385
10^{-2}	0.829	3.557	4.386
10^{-3}	1.107	3.281	4.388

C.2 The process $e^-e^+ \to e^-e^+\gamma$

Table C.5: Test of the C_{UV} independence of the amplitude. In this table, we take the non-linear gauge parameters to be 0, $\lambda = 10^{-17}$GeV and we use 1 TeV for the center-of-mass energy.

C_{UV}	$2\Re(\mathcal{M}_{Loop}\mathcal{M}^{+}_{Tree})$
0	$-1.88001614070088633160096380252506$
10^2	$-1.88001614070088633160096380252504$
10^4	$-1.88001614070088633160096380252483$

Table C.6: Gauge invariance of the amplitude. In this table, we set $C_{UV} = 0$, the photon mass is 10^{-17}GeV and a 1 TeV center-of-mass energy.

$(\tilde{\alpha}, \tilde{\beta}, \tilde{\delta}, \tilde{\kappa}, \tilde{\epsilon})$	$2\Re(\mathcal{M}_{Loop}\mathcal{M}^{+}_{Tree})$
(0, 0, 0, 0, 0)	$-1.88001614070088633160096380252506$
(1.1,1.2,1.3,1.4,1.5)	$-1.88001614070088633160096380252527$
(11,12,13,14,15)	$-1.88001614070088633160096380260499$

Table C.7: Test of the IR finiteness of the amplitude. In this table we take the non-linear gauge parameters to be 0, $C_{UV} = 0$ and the center-of-mass energy is 1 TeV.

λ [GeV]	$2\Re(\mathcal{M}_{Loop}\mathcal{M}^{+}_{Tree})$+ soft contribution
10^{-17}	$-0.392635564863145920331840202138979$
10^{-20}	$-0.392635564863145860698638985751228$
10^{-25}	$-0.392635564863145860639598148071754$

Table C.8: Test of the k_c-stability of the result. We choose the photon mass to be 10^{-17} GeV and the center-of-mass energy is 1 TeV. The second column presents the hard photon cross-section and the third column presents the soft photon cross-section. The final column is the sum of both. The statistical error of integration step is below 0.1% for this test.

k_c [GeV]	σ_S [pb]	σ_H [pb]	σ_{S+H} [pb]
10^{-1}	6.829	1.454	8.284
10^{-2}	6.302	1.983	8.286
10^{-3}	5.776	2.512	8.289

C.3 The process $e^-e^+ \to t\bar{t}$

Table C.9: Test of C_{UV} independence of the amplitude. In this table, we take the non-linear gauge parameters to be 0, $\lambda = 10^{-17}$GeV, $k_c = 0.001$ GeV and we use 1 TeV for the center-of-mass energy.

C_{UV}	$2\Re(\mathcal{T}^+_{Tree}\mathcal{T}_{Loop})$
0	$-0.31484432217751533010224560709400 6$
100	$-0.314844322177515330102245607094006$
10000	$-0.314844322177515330102245607094022$

Table C.10: Test of the IR finiteness of the amplitude. In this table we take the non-linear gauge parameters to be 0, $C_{UV} = 0$, $k_c = 0.001$ GeV and the center-of-mass energy is 1 TeV.

λ [GeV]	$2\Re(\mathcal{T}^+_{Tree}\mathcal{T}_{Loop})$+soft contribution
10^{-17}	$-9.955861975463389719535255330215330 \cdot 10^{-2}$
10^{-21}	$-9.955861975463388891063512557747683 \cdot 10^{-2}$
10^{-25}	$-9.955861975463388890980665383470468 \cdot 10^{-2}$

Table C.11: Gauge invariance of the amplitude. In this table, we set $C_{UV} = 0$, the photon mass is 10^{-17}GeV and a 1 TeV center-of-mass energy.

$(\tilde{\alpha}, \tilde{\beta}, \tilde{\kappa}, \tilde{\delta}, \tilde{\epsilon})$	$2\Re(\mathcal{T}^+_{Tree}\mathcal{T}_{Loop})$
$(0, 0, 0, 0, 0)$	$-0.314844322177515330102245607094006$
$(10, 20, 30, 40, 50)$	$-0.314844322177515330102245607094044$
$(100, 200, 300, 400, 500)$	$-0.314844322177515330102245607094390$

Table C.12: Test of the k_c-stability of the result. We choose the photon mass to be 10^{-17} GeV and the center-of-mass energy is 1 TeV. The second column presents the hard photon cross-section and the third column presents the soft photon cross-section. The final column is the sum of both. The statistical error of integration step is below 0.1% for this test.

k_c [GeV]	σ_H	σ_S	σ_{S+H}
10^{-5}	$3.899 \cdot 10^{-1}$	$4.751 \cdot 10^{-1}$	8.650
10^{-3}	$2.894 \cdot 10^{-1}$	$5.757 \cdot 10^{-1}$	8.651
10^{-1}	$1.888 \cdot 10^{-1}$	$6.763 \cdot 10^{-1}$	8.651

C.4 The process $e^-e^+ \to t\bar{t}\gamma$

Table C.13: Test of C_{UV} independence of the amplitude. In this table, we take the non-linear gauge parameters to be 0, $\lambda = 10^{-17}$GeV and we use 1 TeV for the center-of-mass energy.

C_{UV}	$2\Re(\mathcal{T}^+_{Tree}\mathcal{T}_{Loop})$
0	$-1.479425611153907833172729692371911 \cdot 10^{-3}$
100	$-1.479425611153907833172729692371906 \cdot 10^{-3}$
10000	$-1.479425611153907833172729692371514 \cdot 10^{-3}$

Table C.14: Test of the IR finiteness of the amplitude. In this table we take the non-linear gauge parameters to be 0, $C_{UV} = 0$ and the center-of-mass energy is 1 TeV.

λ [GeV]	$2\Re(\mathcal{T}^+_{Tree}\mathcal{T}_{Loop})$+soft contribution
10^{-17}	$-3.942163564873669410370612777244471 \cdot 10^{-4}$
10^{-21}	$-3.942163564873668923305357052304267 \cdot 10^{-4}$
10^{-25}	$-3.942163564873668923256647278347548 \cdot 10^{-4}$

Table C.15: Gauge invariance of the amplitude. In this table, we set $C_{UV} = 0$, the photon mass is 10^{-17}GeV and a 1 TeV center-of-mass energy.

$(\tilde{\alpha}, \tilde{\beta}, \tilde{\kappa}, \tilde{\delta}, \tilde{\epsilon})$	$2\Re(\mathcal{T}^+_{Tree}\mathcal{T}_{Loop})$
$(0, 0, 0, 0, 0)$	$-1.479425611153907833172729692371911 \cdot 10^{-3}$
$(10, 20, 30, 40, 50)$	$-1.479425611153907833172728540520892 \cdot 10^{-3}$
$(100, 200, 300, 400, 500)$	$-1.479425611153907833172650177990101 \cdot 10^{-3}$

Table C.16: Test of the k_c-stability of the result. We choose the photon mass to be 10^{-17} GeV and the center-of-mass energy is 1 TeV. The second column presents the hard photon cross-section and the third column presents the soft photon cross-section. The final column is the sum of both. The statistical error of integration step is below 0.1% for this test.

k_c[GeV]	σ_H	σ_S	σ_{S+H}
10^{-5}	$4.172723 \cdot 10^{-2}$	$5.885469 \cdot 10^{-2}$	0.10058192
10^{-3}	$2.926684 \cdot 10^{-2}$	$7.131737 \cdot 10^{-2}$	0.10058421
10^{-1}	$1.678994 \cdot 10^{-2}$	$8.377319 \cdot 10^{-2}$	0.10056313

Appendix D

The phase space integration

D.1 Two-body phase space integral

For a simple case, one should start with the definition of the two-body phase space integral. That is

$$\Phi_2(s, m_1, m_2) = \int d^4p_1 d^4p_2 \delta(p_1^2 - m_1^2)\delta(p_2^2 - m_2^2)\delta^4(p - p_1 - p_2)\Theta(p_1^0)\Theta(p_2^0), \tag{D.1}$$

with the incoming momentum sum $p = (p_a + p_b), p^2 = s$ and outgoing momenta $p_{1,2}^2 = m_{1,2}^2$. As a result of Lorentz invariance, the integral is a function of the Lorentz scalars s, m_1 and m_2. In the formula $\Theta(p_1^0)$ and $\Theta(p_2^0)$ are appeared by the requirement of the positiveness of the energy of particles $p_{1,2}$. The delta functions are represented for on-shell conditions on $p_{1,2}$ and the total momentum conservation.

In the center-of-mass system (CMS) of $p_a + p_b$ or with $p = (\sqrt{s}, 0, 0, 0)$, one take into form

$$\begin{aligned}
\Phi_2(s, m_1, m_2) &= \int d^4p_1\delta(p_1^2 - m_1^2)\delta((p - p_1)^2 - m_2^2)\Theta(p_1^0) \qquad \text{(D.2)}\\
&= \int \frac{d^3p_1^*}{2E_1^*}\delta(s + m_1^2 - 2\sqrt{s}E_1^* - m_2^2)\\
&= \frac{1}{4\sqrt{s}}\int p_*^1 dE_1^* d\Omega_1^*\delta\left(E_1^* - \frac{s + m_1^2 - m_2^2}{2\sqrt{s}}\right)\\
&= \frac{p_1^*(s, m_1, m_2)}{4\sqrt{s}}\int d\Omega_1^*,
\end{aligned}$$

where

$$E_1^* = \frac{s + m_1^2 - m_2^2}{2\sqrt{s}}, E_2^* = \sqrt{s} - E_1^* = \frac{s + m_2^2 - m_1^2}{2\sqrt{s}}, \qquad \text{(D.3)}$$

and momenta

$$p_1^* = |\vec{p_1^*}| = \frac{\sqrt{\lambda(s, m_1^2, m_2^2)}}{2\sqrt{s}}, \quad p_2^* = p_1^* \qquad \text{(D.4)}$$

The Lorentz invariant function $\lambda(s, m_1^2, m_2^2)$ is defined

$$\lambda(s, m_1^2, m_2^2) = (s - (m_1 + m_2)^2)(s - (m_1 - m_2)^2), \qquad \text{(D.5)}$$

with $\sqrt{s} \geq m_1 + m_2$.

D.2 The n-body phase space integral

The n-body phase space Φ_n of the processes $a + b \to p_1 + p_2 +, \cdots, +p_n$ depends on center-of-mass energy and final particle masses. Its Lorentz invariant form as

$$\Phi_n = \int \delta^4(p_a + p_b - \sum_{i=1}^{n} p_i)\prod_{i=1}^{n} d^4p_i\delta(p_i^2 - m_i^2)\Theta(p_i^0) \qquad \text{(D.6)}$$

The general idea is to split the Φ_n into product of Π_2. For this purpose, one define the momentum sum as

$$k_i = \sum_{j=1}^{i} p_i; \quad k_i^2 = M_i^2. \qquad \text{(D.7)}$$

One continues by introducing the identities:

$$1 = \int dM_{n-1}^2 \delta(k_{n-1}^2 - M_{n-1}^2)\Theta(k_{n-1}^0) \tag{D.8}$$

and

$$1 = \int d^4k_{n-1}\delta^4(p - k_{n-1} - p_n) \tag{D.9}$$

into the integral of Equation D.6; separating out the arguments containing k_{n-1} and p_n terms one obtains:

$$\begin{aligned}
\Phi_n(M_n^2, m_1, m_2, \ldots, m_n) &= \int dM_{n-1}^2 \int d^4k_{n-1}d^4p_n\delta(k_{n-1}^2 - M_{n-1}^2) \\
&\times \delta(p_n^2 - m_n^2)\delta^4(p - k_{n-1} - p_n)\Theta(k_{n-1}^0)\Theta(p_n^0) \\
&\times \int \delta^4(k_{n-1} - \sum_{i=1}^{n-1} p_i) \prod_{i=1}^{n-1} d^4p_i\delta(p_i^2 - m_i^2)\Theta(p_i^0) \\
&= \int dM_{n-1}^2 \int d^4k_{n-1}d^4p_n\delta(k_{n-1}^2 - M_{n-1}^2) \qquad \text{(D.10)} \\
&\times \delta(p_n^2 - m_n^2)\delta^4(p - k_{n-1} - p_n)\Theta(k_{n-1}^0)\Theta(p_n^0) \\
&\times \Phi_{n-1}(M_{n-1}^2, m_1, m_2, \ldots, m_{n-1}), \\
&= \int dM_{n-1}^2 \Phi_2(M_n^2, M_{n-1}^2, m_n)\Phi_{n-1}(M_{n-1}^2, m_1, m_2, \ldots, m_{n-1}),
\end{aligned}$$

Performing the recurrence of above relation, one then arrive

$$\begin{aligned}
\Phi_n(M_n^2, m_1, m_2, \ldots, m_n) &= \int_{(M_{n-2}+m_{n-1})^2}^{(M_n-m_n)^2} dM_{n-1}^2 \frac{\sqrt{\lambda(M_n^2, M_{n-1}^2, m_n^2)}}{8M_n^2} \int d\Omega_n^* \\
&\times \int_{(M_{n-3}+m_{n-2})^2}^{(M_n-m_n-m_{n-1})^2} dM_{n-2}^2 \frac{\sqrt{\lambda(M_{n-1}^2, M_{n-2}^2, m_{n-1}^2)}}{8M_{n-1}^2} \int d\Omega_{n-1}^* \\
&\times \ldots \int_{(M_{i-1}+m_i)^2}^{(M_n-\sum_{j=i+1}^n m_j)^2} dM_{i-1}^2 \frac{\sqrt{\lambda(M_i^2, M_{i-1}^2, m_i^2)}}{8M_i^2} \int d\Omega_i^* \ldots \\
&\times \int_{(m_1+m_2)^2}^{(M_n-\sum_{j=3}^n m_j)^2} dM_2^2 \frac{\sqrt{\lambda(M_3^2, M_2^2, m_3^2)}}{8M_3^2} \int d\Omega_3^* \\
&\times \frac{\sqrt{\lambda(M_2^2, m_1^2, m_2^2)}}{8M_2^2} \int d\Omega_2^*,
\end{aligned}$$

where $d\Omega_n^* = d\cos\theta_n^* d\phi_n^*$.

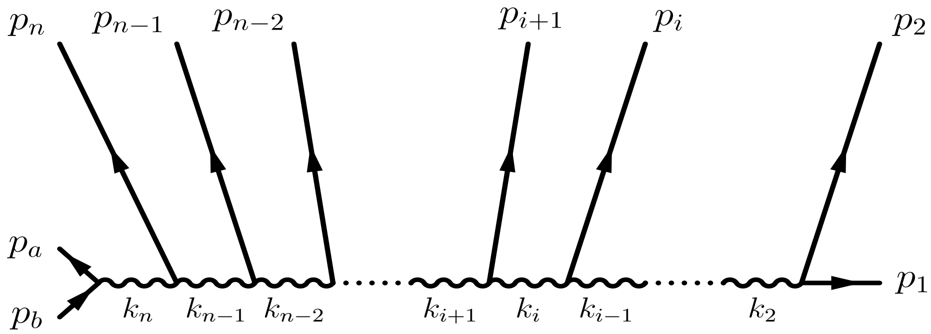

Figure D.1: The diagrammatic representation of splitting phase space of n particle.

Applying the relation D.11 one obtain the three-body phase space integral directly

$$\begin{aligned}\Phi_n(M_3^2, m_1, m_2, m_3) &= \int\limits_{(m_1+m_2)^2}^{(M_n-m_3)^2} dM_2^2 \frac{\sqrt{\lambda(M_3^2, M_2^2, m_3^2)}}{8M_3^2} \int d\Omega_3^* \\ &\times \frac{\sqrt{\lambda(M_2^2, m_1^2, m_2^2)}}{8M_2^2} \int d\Omega_2^*,\end{aligned}$$

It is important to note that $d\Omega_2^* = d\cos\theta_2^* d\phi_2^*$ is defined in CMS $(1+2)$ and $d\Omega_3^* = d\cos\theta_3^* d\phi_3^*$ is defined in CMS $(a+b)$.

In the CMS $(1+2)$, one have

$$\begin{aligned}E_1 &= \frac{M_2^2 + m_1^2 - m_2^2}{2M_2}, \quad E_2 = \frac{M_2^2 + m_2^2 - m_1^2}{2M_2}, \\ |\mathrm{p}_1| &= |\mathrm{p}_2| = \frac{\lambda^{1/2}(M_2^2, m_1^2, m_2^2)}{2M_2}.\end{aligned}$$

Three component of p_1 is written as

$$\begin{cases}\mathrm{p}_{1\mathrm{z}} = |\mathrm{p}_1|\cos\theta_{b1} \\ \mathrm{p}_{1\mathrm{x}} = |\mathrm{p}_1|\sin\theta_{b1}\cos\phi_{b1} \\ \mathrm{p}_{1\mathrm{y}} = |\mathrm{p}_1|\sin\theta_{b1}\sin\phi_{b1}\end{cases} \tag{D.11}$$

In the CMS $(a + b)$,

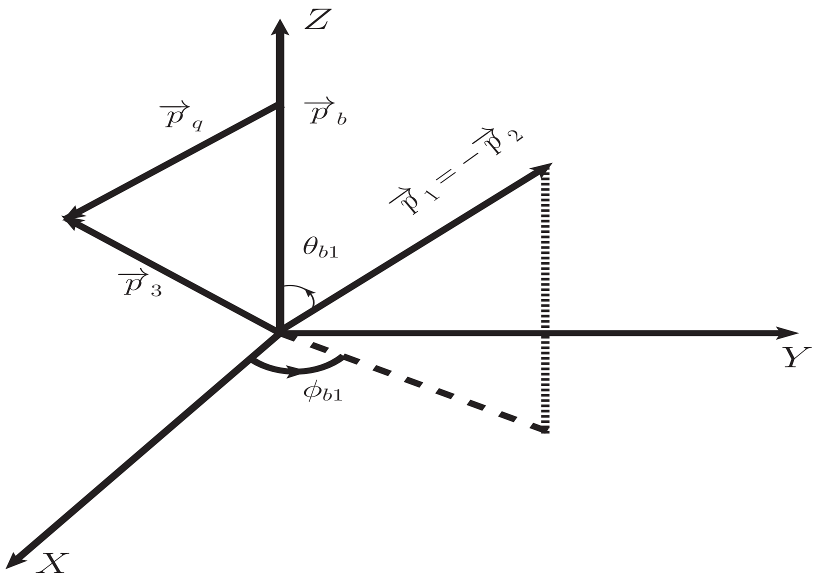

Figure D.2: In the CMS $(1 + 2)$.

$$p_a = (\sqrt{s}/2, 0, 0, |\overrightarrow{p}|) \quad \text{and} \quad p_b = (\sqrt{s}/2, 0, 0, -|\overrightarrow{p}|). \tag{D.12}$$

Four component of particle 3 in this frame is

$$|\mathrm{p}_3| = \frac{\lambda^{1/2}(s, M_2^2, m_3^2)}{2\sqrt{s}}, \quad E_3 = \frac{s + m_3^2 - M_2^2}{2\sqrt{s}}. \tag{D.13}$$

One define $Q = -p_1 - p_2$ which is defined in the CMS $(a + b)$ as

$$\begin{cases} Q_0 = \dfrac{s + M_2^2 - m_3^2}{2\sqrt{s}} \\ \mathrm{Q_z} = |\mathrm{p}_3|\mathrm{cos}\theta_{b3} \\ \mathrm{Q_x} = |\mathrm{p}_3|\mathrm{sin}\theta_{b3} \\ \mathrm{Q_y} = 0 \end{cases} \tag{D.14}$$

Finally we perform a boost the p_1 and p_2 in CMS $(1 + 2)$ to CMS $(a + b)$ by using the Lorentz transformation with four vector boost is Q_μ.

Appendix E

The F function

A general form of F_n function is defined as

$$F_n(A,B,s) = \int_0^1 dx\; x^n \log D_2 = \int_0^1 dx\; x^n \log\left[(1-x)M_A^2 + xM_B^2 - x(1-x)s\right] \tag{E.1}$$

The $F_{1,2}(A,B,s)$ can reduce to $F_0(A,B,s)$ as

$$F_1(A,B,s) = \frac{1}{2}\left(1+\frac{M_A^2-M_B^2}{s}\right)F_0(A,B)+\frac{1}{2s}\left(M_B^2\log M_B^2 - M_A^2\log M_A^2 - M_B^2 + M_A^2\right) \tag{E.2}$$

and

$$\begin{aligned} F_2(A,B,s) = \; & \frac{2}{3}\left(1+\frac{M_A^2-M_B^2}{s}\right)F_1(A,B) - \frac{M_A^2}{3s}F_0(A,B) \\ & +\frac{1}{3s}\left(M_B^2\log M_B^2 + \frac{1}{2}(M_A^2-M_B^2)\right) - \frac{1}{18} \end{aligned} \tag{E.3}$$

where $F_0(A,B,s)$ is given by

$$F_0(A,B,s) = \log M_B^2 - 2 - \frac{1}{2}(1+\delta)\log\frac{M_2^2}{M_1^2} + \frac{1}{2}r\log(\rho), \tag{E.4}$$

with $\delta = \frac{M_A^2-M_B^2}{s}$; $r = \sqrt{(1+\delta)^2 - 4M_A^2/s}$ and $\rho = \frac{M_A^2+M_B^2-(1+r)s}{M_A^2+M_B^2-(1-r)s}$.

In the special case, the function $F_0(A,B,0)$ is obtained

$$F_0(A,B,0) = \begin{cases} \log M_A^2 & (A = B) \\ \\ \dfrac{M_B^2 \log M_B^2 - M_A^2 \log M_A^2}{M_B^2 - M_A^2} - 1 & (A \neq B) \end{cases} \tag{E.5}$$

Bibliography

[1] G. Aad *et al.* [ATLAS Collaboration], Phys. Lett. B **716** (2012) 1 [arXiv:1207.7214 [hep-ex]].

[2] S. Chatrchyan *et al.* [CMS Collaboration], Phys. Lett. B **716** (2012) 30 [arXiv:1207.7235 [hep-ex]].

[3] G. Aad *et al.* [ATLAS Collaboration], Phys. Lett. B **726** (2013) 88.

[4] G. Aad *et al.* [ATLAS Colaboration], Phys. Lett. B **726** (2013) 120.

[5] S. Chatrchyan *et al.* [CMS Collaboration], JHEP **1401** (2014) 096.

[6] S. Chatrchyan *et al.* [CMS Collaboration], arXiv:1312.5353 [hep-ex].

[7] S. L. Glashow, Nucl. Phys. **22** (1961) 579;
S. Weinberg, Phys. Rev. Lett. **19** (1967) 1264;
A. Salam, In the Proceedings of 8th Nobel Symposium, Lerum, Sweden, 19-25 May 1968, p. 367;
S. L. Glashow, J. Iliopoulos, L. Maiani, Phys. Rev. D **2** (1970) 1285.

[8] F. Englert, R. Brout, Phys. Rev. Lett. **13** (1964) 321.

[9] P. W. Higgs, Phys. Lett. **12** (1964) 132 and Phys. Rev. Lett. **13** (1964) 508.

[10] http://home.web.cern.ch/about/accelerators/large-electron-positron-collider.

[11] http://lhc.web.cern.ch/lhc.

[12] [ATLAS Collaboration], arXiv:1307.7292 [hep-ex].

[13] [CMS Collaboration], arXiv:1307.7135.

[14] H. Baer, T. Barklow, K. Fujii, Y. Gao, A. Hoang, S. Kanemura, J. List and H. E. Logan *et al.*, arXiv:1306.6352 [hep-ph].

[15] G. Passarino and M. J. G. Veltman, Nucl. Phys. B **160** (1979) 151.

[16] A. Denner and S. Dittmaier, Nucl. Phys. B **734** (2006) 62 [hep-ph/0509141].

[17] A. Denner, S. Dittmaier, M. Roth and L. H. Wieders, Nucl. Phys. B **724** (2005) 247 [Erratum-ibid. B **854** (2012) 504] [hep-ph/0505042].

[18] A. Denner, S. Dittmaier, M. Roth and L. H. Wieders, Phys. Lett. B **612** (2005) 223 [Erratum-ibid. B **704** (2011) 667] [hep-ph/0502063].

[19] A. Denner, S. Dittmaier, M. Roth and L. H. Wieders, Nucl. Phys. Proc. Suppl. **157** (2006) 68 [hep-ph/0601122].

[20] T. Ishikawa, T. Kaneko, K. Kato, S. Kawabata, Y. Shimizu and H. Tanaka, KEK Report 92-19, 1993, `GRACE` manual Ver. 1.0.

[21] G. Belanger, F. Boudjema, J. Fujimoto, T. Ishikawa, T. Kaneko, K. Kato and Y. Shimizu, Phys. Rept. **430**, 117 (2006) [hep-ph/0308080].

[22] Z. Bern, L. J. Dixon and D. A. Kosower, Annals Phys. **322** (2007) 1587 [arXiv:0704.2798 [hep-ph]].

[23] C. F. Berger, Z. Bern, L. J. Dixon, F. Febres Cordero, D. Forde, H. Ita, D. A. Kosower and D. Maitre, Phys. Rev. D **78** (2008) 036003 [arXiv:0803.4180 [hep-ph]].

[24] T. Binoth, J. -P. .Guillet, G. Heinrich, E. Pilon and T. Reiter, Comput. Phys. Commun. **180** (2009) 2317 [arXiv:0810.0992 [hep-ph]].

[25] G. Cullen, N. Greiner, A. Guffanti, J. -P. Guillet, G. Heinrich, S. Karg, N. Kauer and T. Kleinschmidt *et al.*, Nucl. Phys. Proc. Suppl. **205-206** (2010) 67 [arXiv:1007.3580 [hep-ph]].

[26] J. P. .Guillet, E. Pilon, M. Rodgers and M. S. Zidi, JHEP **1311** (2013) 154 [arXiv:1310.4397 [hep-ph]].

[27] E. Gildener, "Gauge Symmetry Hierarchies," Phys. Rev. D **14** (1976) 1667;
E. Gildener and S. Weinberg, "Symmetry Breaking And Scalar Bosons," Phys. Rev. D **13** (1976) 3333;
S. Weinberg, "Gauge Hierarchies," Phys. Lett. B **82** (1979) 387.

[28] F. Caravaglios and M. Moretti, *Phys. Lett.* **B358** (1995) 332; hep-ph/9507237.
F. Caravaglios and M. Moretti, *Z. Physik* **C74** (1997) 291; hep-ph/9604316.

[29] A. Kanaki, C.G. Papadopoulos, *Comput. Phys. Commun.* **132** (2000) 306; hep-ph/0002082.

[30] M. Moretti, T. Ohl and J. Reuter, `hep-ph/0102195`.

[31] F. Boudjema and L. D. Ninh, Phys. Rev. D **78** (2008) 093005 [arXiv:0806.1498 [hep-ph]].

[32] http://minami-home.kek.jp.

[33] http://legacy.kek.jp/intra-e/index.html.

[34] J. Fujimoto, T. Ishikawa, M. Jimbo, T. Kon and M. Kuroda, Nucl. Instrum. Meth. A **534**, 246 (2004) [hep-ph/0402145].

[35] J. Fujimoto, T. Ishikawa, M. Jimbo, T. Kaneko, K. Kato, S. Kawabata, K. Kon and M. Kuroda *et al.*, Comput. Phys. Commun. **153** (2003) 106 [hep-ph/0208036].

[36] J. Fujimoto, T. Ishikawa, M. Jimbo, T. Kon, Y. Kurihara and M. Kuroda, hep-ph/0701200.

[37] K. Aoki, Z. Hioki, R. Kawabe, M. Konuma and T. Muta, Suppl. Prog. Theor. Phys. **73** (1982) 1.

[38] F. Boudjema and E. Chopin, *Z. Phys.* **C73** (1996) 85; hep-ph/9507396.

[39] G. J. van Oldenborgh, *Comput. Phys. Commun.* **58** (1991) 1.

[40] T. Hahn, `LoopTools`, `http://www.feynarts.de/looptools/`.

[41] http://www.nikhef.nl/ form.
J. A. M. Vermaseren:*New Features of FORM*; math-ph/0010025.

[42] J. A. M. Vermaseren, Nucl. Phys. Proc. Suppl. **183** (2008) 19 [arXiv:0806.4080 [hep-ph]].

[43] M. Tentyukov, J. A. M. Vermaseren and J. Vollinga, PoS ACAT **2010** (2010) 072 [arXiv:1006.2099 [hep-ph]].

[44] J. A. M. Vermaseren, Nucl. Phys. Proc. Suppl. **205-206** (2010) 104 [arXiv:1006.4512 [hep-ph]].

[45] J. A. M. Vermaseren, PoS CPP **2010** (2010) 012 [arXiv:1101.0511 [hep-ph]].
J. Kuipers, T. Ueda, J.A.M. Vermaseren, J. Vollinga, FORM version 4.0, **j.cpc.** (2012) .12.028.

[46] S. Kawabata, *Comp. Phys. Commun.* **41** (1986) 127; *ibid.,* **88** (1995) 309.

[47] G. Belanger, F. Boudjema, J. Fujimoto, T. Ishikawa, T. Kaneko, Y. Kurihara, K. Kato and Y. Shimizu, Phys. Lett. B **576** (2003) 152 [hep-ph/0309010].

[48] G. Belanger, F. Boudjema, J. Fujimoto, T. Ishikawa, T. Kaneko, K. Kato, Y. Shimizu and Y. Yasui, Phys. Lett. B **571**, 163 (2003) [hep-ph/0307029].

[49] G. Belanger, F. Boudjema, J. Fujimoto, T. Ishikawa, T. Kaneko, K. Kato and Y. Shimizu, Nucl. Phys. Proc. Suppl. **116**, 353 (2003) [hep-ph/0211268].

[50] R. -Y. Zhang, W. -G. Ma, H. Chen, Y. -B. Sun and H. -S. Hou, Phys. Lett. B **578** (2004) 349 [hep-ph/0308203].

[51] Y. You, W. -G. Ma, H. Chen, R. -Y. Zhang, S. Yan-Bin and H. -S. Hou, Phys. Lett. B **571** (2003) 85 [hep-ph/0306036].

[52] A. Denner, S. Dittmaier, M. Roth and M. M. Weber, Phys. Lett. B **575** (2003) 290 [hep-ph/0307193].

[53] A. Denner, S. Dittmaier, M. Roth and M. M. Weber, Nucl. Phys. B **680** (2004) 85 [hep-ph/0309274].

[54] A. Denner, S. Dittmaier, M. Roth and M. M. Weber, Phys. Lett. B **560** (2003) 196 [hep-ph/0301189].

[55] A. Denner, S. Dittmaier, M. Roth and M. M. Weber, Nucl. Phys. B **660** (2003) 289 [hep-ph/0302198].

[56] K. Kato, F. Boudjema, J. Fujimoto, T. Ishikawa, T. Kaneko, Y. Kurihara, Y. Shimizu and Y. Yasui, PoS HEP **2005** (2006) 312.

[57] P. H. Khiem, J. Fujimoto, T. Ishikawa, T. Kaneko, K. Kato, Y. Kurihara, Y. Shimizu and T. Ueda *et al.*, Eur. Phys. J. C **73** (2013) 2400 [arXiv:1211.1112 [hep-ph]].

[58] P. H. Khiem, Y. Kurihara, J. Fujimoto, T. Ishikawa, T. Kaneko, K. Kato, N. Nakazawa and Y. Shimizu *et al.*, arXiv:1403.6557 [hep-ph].

[59] J. Beringer et al. (Particle Data Group), Phys. Rev. D86, 010001 (2012).

[60] A. Freitas, W. Hollik, W. Walter and G. Weiglein, Nucl. Phys. B **632** (2002) 189 [Erratum-ibid. B **666** (2003) 305] [hep-ph/0202131].

[61] A. Sirlin, Phys. Rev. D **22** (1980) 971.

[62] F. Yuasa, T. Ishikawa, J. Fujimoto, N. Hamaguchi, E. de Doncker and Y. Shimizu, PoS ACAT **08** (2008) 122 [arXiv:0904.2823 [hep-ph]].

[63] F. Yuasa, T. Ishikawa, Y. Kurihara, J. Fujimoto, Y. Shimizu, N. Hamaguchi, E. de Doncker and K. Kato, PoS CPP **2010** (2010) 017 [arXiv:1109.4213 [hep-ph]].

[64] E. de Doncker, J. Fujimoto, N. Hamaguchi, T. Ishikawa, Y. Kurihara, M. Ljucovic, Y. Shimizu and F. Yuasa, arXiv:1110.3587 [hep-ph].

[65] F. Yuasa, E. de Doncker, N. Hamaguchi, T. Ishikawa, K. Kato, Y. Kurihara, J. Fujimoto and Y. Shimizu, Comput. Phys. Commun. **183** (2012) 2136 [arXiv:1112.0637 [hep-ph]].

[66] K. Kato, E. de Doncker, N. Hamaguchi, T. Ishikawa, T. Koike, Y. Kurihara, Y. Shimizu and F. Yuasa, PoS QFTHEP **2011** (2013) 029 [arXiv:1201.6127 [hep-ph]].

[67] G. 't Hooft and M. Veltman, **B153** (1979) 365.

[68] J. Fujimoto, M. Igarashi, N. Nakazawa, Y. Shimizu and K. Tobimatsu, *Suppl. Prog. Theor. Phys.* **100** (1990) 1.

[69] (Ed.) Bruning, O. et al. LHC design report. Vol. I: The LHC main ring. CERN-2004-003-V-1;
http://ab-div.web.cern.ch/ab-div/Publications/LHC-DesignReport.html.

[70] CERN, CERN-LHCC-99-14.

[71] J. Ohnemus, Phys. Rev. D **44** (1991) 1403.

[72] J. M. Campbell, R. K. Ellis and C. Williams, JHEP **1107** (2011) 018 [arXiv:1105.0020 [hep-ph]].

[73] S. Dittmaier, S. Kallweit and P. Uwer, Phys. Rev. Lett. **100** (2008) 062003 [arXiv:0710.1577 [hep-ph]].

[74] E. Accomando, A. Denner and S. Pozzorini, Phys. Rev. D **65** (2002) 073003 [hep-ph/0110114].

[75] E. Accomando, A. Denner and A. Kaiser, Nucl. Phys. B **706** (2005) 325 [hep-ph/0409247].

[76] E. Accomando, A. Denner and C. Meier, Eur. Phys. J. C **47** (2006) 125 [hep-ph/0509234].

[77] A. Bierweiler, T. Kasprzik, J. H. Kühn and S. Uccirati, JHEP **1211** (2012) 093 [arXiv:1208.3147 [hep-ph]].

[78] A. Bierweiler, T. Kasprzik and J. H. Kühn, JHEP **1312** (2013) 071 [arXiv:1305.5402 [hep-ph]].

[79] J. Baglio, L. D. Ninh and M. M. Weber, Phys. Rev. D **88** (2013) 113005 [arXiv:1307.4331].

[80] R. K. Ellis , W. J. Stirling, B. R. Webber, QCD and Collider Physics, Camb. Monogr. Part. Phys. Nucl. Phys. Cosmol. 8 (1996) 1-453.

[81] J. Butterworth, G. Dissertori, S. Dittmaier, D. de Florian, N. Glover, K. Hamilton, J. Huston and M. Kado *et al.*, arXiv:1405.1067 [hep-ph].

[82] A. D. Martin, W. J. Stirling, R. S. Thorne and G. Watt, Eur. Phys. J. C **63** (2009) 189 [arXiv:0901.0002 [hep-ph]].

[83] A. D. Martin, W. J. Stirling, R. S. Thorne and G. Watt, Eur. Phys. J. C **64** (2009) 653 [arXiv:0905.3531 [hep-ph]].

[84] A. D. Martin, W. J. Stirling, R. S. Thorne and G. Watt, Eur. Phys. J. C **70** (2010) 51 [arXiv:1007.2624 [hep-ph]].

[85] T. Behnke, J. E. Brau, B. Foster, J. Fuster, M. Harrison, J. M. Paterson, M. Peskin and M. Stanitzki *et al.*, arXiv:1306.6327 [physics.acc-ph].

[86] I. Božović Jelisavčić, S. Lukić, G. Milutinović Dumbelović, M. Pandurović and I. Smiljanić, JINST **8** (2013) P08012 [arXiv:1304.4082 [physics.acc-ph]].

[87] K.Tobimatsu and Y.Shimizu, Prog. Theor. Phys. **74** (1985), 567-575.

[88] K.Tobimatsu and Y.Shimizu, Prog. Theor. Phys. **75** (1986), 905-913.

[89] M. Bohm, A. Denner, W. Hollik and R. Sommer, Phys. Lett. B **144** (1984) 414.

[90] M. Bohm, A. Denner and W. Hollik, Nucl. Phys. B **304** (1988) 687.

[91] F. A. Berends, R. Kleiss and W. Hollik, Nucl. Phys. B **304** (1988) 712.

[92] J. Fleischer, J. Gluza, A. Lorca and T. Riemann, Eur. J. Phys. **48** (2006) 35 [hep-ph/0606210].

[93] A. A. Penin, Phys. Rev. Lett. **95** (2005) 010408 [hep-ph/0501120].

[94] A. A. Penin, Nucl. Phys. B **734** (2006) 185 [hep-ph/0508127].

[95] R. Bonciani, A. Ferroglia, P. Mastrolia, E. Remiddi and J. J. van der Bij, Nucl. Phys. B **701** (2004) 121 [hep-ph/0405275].

[96] R. Bonciani, A. Ferroglia, P. Mastrolia, E. Remiddi and J. J. van der Bij, Nucl. Phys. B **716** (2005) 280 [hep-ph/0411321].

[97] R. Bonciani, A. Ferroglia and A. A. Penin, Phys. Rev. Lett. **100** (2008) 131601 [arXiv:0710.4775 [hep-ph]].

[98] R. Bonciani, A. Ferroglia and A. A. Penin, JHEP **0802** (2008) 080 [arXiv:0802.2215 [hep-ph]].

[99] A. A. Penin and G. Ryan, JHEP **1111** (2011) 081 [arXiv:1112.2171 [hep-ph]].

[100] K. Tobimatsu and M. Igarashi, Comput. Phys. Commun. **136** (2001) 105.

[101] S. Actis, P. Mastrolia and G. Ossola, Phys. Lett. B **682** (2010) 419 [arXiv:0909.1750 [hep-ph]].

[102] M. Igarashi et al, *in preparation.*

[103] F. Abe *et al.* [CDF Collaboration], Phys. Rev. Lett. **74** (1995) 2626 [hep-ex/9503002].

[104] S. Abachi *et al.* [D0 Collaboration], Phys. Rev. Lett. **74** (1995) 2632 [hep-ex/9503003].

[105] ATLAS Collaboration, ATLAS-CONF-2012-024.

[106] CMS Collaboration, CMS-PAS-TOP-11-024.

[107] D. Asner, A. Hoang, Y. Kiyo, R. Pöschl, Y. Sumino and M. Vos, arXiv:1307.8265 [hep-ex].

[108] T. Horiguchi, A. Ishikawa, T. Suehara, K. Fujii, Y. Sumino, Y. Kiyo and H. Yamamoto, arXiv:1310.0563 [hep-ex].

[109] P. Doublet, F. Richard, R. Poschl, T. Frisson and J. Rouene, arXiv:1202.6659 [hep-ex].

[110] M. S. Amjad, M. Boronat, T. Frisson, I. Garcia, R. Poschl, E. Ros, F. Richard and J. Rouene *et al.*, arXiv:1307.8102.

[111] A. H. Hoang, M. Beneke, K. Melnikov, T. Nagano, A. Ota, A. A. Penin, A. A. Pivovarov and A. Signer *et al.*, Eur. Phys. J. direct C **2** (2000) 1 [hep-ph/0001286].

[112] M. Beneke and Y. Kiyo, Phys. Lett. B **668** (2008) 143 [arXiv:0804.4004 [hep-ph]].

[113] A. H. Hoang and M. Stahlhofen, JHEP **1106** (2011) 088 [arXiv:1102.0269 [hep-ph]].

[114] M. Stahlhofen, Talk at the Top Physics Workshop. Paris, May 2012..

[115] A. Lazopoulos, K. Melnikov and F. J. Petriello, Phys. Rev. D **77** (2008) 034021 [arXiv:0709.4044 [hep-ph]].

[116] K. Melnikov, M. Schulze and A. Scharf, Phys. Rev. D **83** (2011) 074013 [arXiv:1102.1967 [hep-ph]].

[117] A. Juste, Y. Kiyo, F. Petriello, T. Teubner, K. Agashe, P. Batra, U. Baur and C. F. Berger *et al.*, hep-ph/0601112.

[118] M. S. Amjad, M. Boronat, T. Frisson, I. Garcia, R. Poschl, E. Ros, F. Richard and J. Rouene *et al.*, arXiv:1307.8102.

[119] T. Aaltonen *et al.* [CDF Collaboration], Phys. Rev. D **83**, 112003 (2011) [arXiv:1101.0034 [hep-ex]].

[120] V. M. Abazov *et al.* [D0 Collaboration], Phys. Rev. Lett. **100**, 142002 (2008) [arXiv:0712.0851 [hep-ex]].

[121] A. Denner, S. Dittmaier, S. Kallweit and S. Pozzorini, Phys. Rev. Lett. **106** (2011) 052001 [arXiv:1012.3975 [hep-ph]].

[122] A. Denner, S. Dittmaier, S. Kallweit and S. Pozzorini, JHEP **1210** (2012) 110 [arXiv:1207.5018 [hep-ph]].

[123] G. Bevilacqua, M. Czakon, A. van Hameren, C. G. Papadopoulos and M. Worek, JHEP **1102** (2011) 083 [arXiv:1012.4230 [hep-ph]].

[124] K. Melnikov, M. Schulze and A. Scharf, Phys. Rev. D **83** (2011) 074013 [arXiv:1102.1967 [hep-ph]].

[125] K. Melnikov, A. Scharf and M. Schulze, Phys. Rev. D **85** (2012) 054002 [arXiv:1111.4991 [hep-ph]].

[126] CMS collaboration, Physics Analysis Summary CMS-PAS-TOP-11-30(2011).

[127] J. Fujimoto and Y. Shimizu, Mod. Phys. Lett. **3A**, 581 (1988).

[128] J. Fleischer, T. Hahn, W. Hollik, T. Riemann, C. Schappacher and A. Werthenbach, hep-ph/0202109.

[129] J. Fleischer, A. Leike, T. Riemann and A. Werthenbach, Eur. Phys. J. C **31**, 37 (2003) [hep-ph/0302259].